

Development of a semi transparent perovskite module

Optimization of the laser scribes for the interconnection

H.F. Castillo González

Technische Universiteit Delft

DEVELOPMENT OF A SEMI TRANSPARENT PEROVSKITE MODULE

OPTIMIZATION OF THE LASER SCRIBES FOR THE INTERCONNECTION

by

H.F. Castillo González

in partial fulfillment of the requirements for the degree of

Master of Science
in Sustainable Energy Technology

at the Delft University of Technology,
to be defended publicly on Tuesday August 22nd, 2017 at 14:00.

Supervisor:	Prof. dr. A. W. Weeber	
Daily supervisor:	Dr. S. Veenstra,	ECN-Solliance
Thesis committee:	Prof. dr. M. Zeman,	TU Delft
	Dr. T. J. Savenije,	TU Delft
	Ing. H. Fledderus,	Holst / TNO-Solliance

This thesis is confidential and cannot be made public until August 22nd, 2017.

An electronic version of this thesis is available at <http://repository.tudelft.nl/>.



PREFACE

This is the end of another professional phase of my life, I am completely happy to achieve another goal of my life. When I moved to The Netherlands I did not imagine the life I was going to live.

I want to thank the *FONDO SECTORIAL CONACYT-SECRETARÍA DE ENERGÍA-SUSTENTABILIDAD ENERGÉTICA* for the sponsorship of this master, I would not be able to accomplish this goal without the aid of my country.

Regarding professional field, I am completely grateful with Dr. Arthur Weeber, who found the place for me at ECN and was my mentor during all these months and gave me advice and complete attention.

Thanks to my committee who is up to evaluate my performance: Dr. Miro Zeeman, Dr. Tom Savenije and especially to Ing. Henri Fledderus who always gave me insight and critical analysis during my stay at Solliance.

My thesis was developed at ECN, Solliance, where I met professional friends and colleagues who always helped me: My daily supervisor Sjoaerd Veenstra, Dong, Olivera DM, Kunal, and specially thanks to Maarten Dörenkämper who were my main support and always had a smile even in tough situations.

I would like to thank to my friends from the Master who were always there: Paulo César, Lisset, Miguel, Gaby, Kenji, Jorge, Patricia and Carlos. Thanks for all the time together, doing work together, quality time, mexican food, laughs and company. *¡Sí se pudo, amigos!*

Thanks to my family friends back in Mexico who always were a big emotional and mental support: My beloved mother, Clarisa, Rudy, Nayeli, and Gustavo.

*H.F. Castillo González
Delft, August 2017*

ABSTRACT

Despite the fact of the outstanding efficiency of the perovskite-based devices, their current size is around a few square millimeters. The application of this thin-film technology in module scale requires an interconnection with optimal laser processing to create a channel for the photo current. In this project, the relation between each film material and the laser beam is analyzed. Furthermore, this scribing process is applied to a working module manufacturing.

A semi transparent triple cation-based perovskite module scribing processing has been studied. An n-i-p structure was used for the device. 200 nm indium tin oxide films were used as the front and back electrode, to guarantee the transparency. Spin deposited layers of tin oxide and spiro-OMeTAD were used as the n-type and p-type layers, respectively. A buffer layer between the hole transmitting film and the anode was applied to enhance the performance; for this purpose, a 20 nm molybdenum oxide layer is vapor-deposited. This architecture had a performance of 10.95 % for a single cell, and 4.06 % for a six cells module in front illumination. The laser system is set to work in the UV range with 1 ps pulse length, 10 kHz frequency and apparent power from 1300 to 1800 for scribing speed between 30 to 60 *mm/s*. To further improve the performance of the module, it was illuminated from the rear side, achieving a 5.9 % efficiency. The results shows a promising outlook for this technology for novel applications, such was in tandem cell applications.

CONTENTS

List of Figures	ix
List of Tables	xi
1 Introduction	1
1.1 Motivation	1
1.2 Objective of the thesis	3
1.3 Outline of the thesis	3
2 Perovskite solar cells	5
2.1 Composition and structure of perovskite materials	5
2.1.1 Triple cation perovskite	6
2.2 Perovskite cell architecture	7
2.2.1 Electrode layer	8
2.2.2 Electron transporting layer	8
2.2.3 Hole transporting material.	9
2.2.4 Anode buffer layer	9
2.3 Working principle of perovskite solar cells	9
3 Perovskite solar module processing	13
3.1 Overview of the module processing.	13
3.2 Thin-film deposition methods	16
3.2.1 Magnetron sputtering	16
3.2.2 Spin coating.	17
3.2.3 Thermal annealing	18
4 Laser technology	21
4.1 Working principle	21
4.1.1 Material - laser beam interaction	22
4.1.2 Pulse length influence on the ablation mechanism	22
4.1.3 Optoelectronic properties of the materials	22
4.2 Laser in organic photovoltaics.	25
5 Methodology	27
5.1 Deposition methods	27
5.1.1 Electrode deposition	27
5.1.2 Electron transmission layer deposition	28
5.1.3 Perovskite layer deposition	28
5.1.4 Hole transmission layer deposition	28
5.1.5 Anode buffer layer deposition	28
5.2 Laser scribing.	28
5.2.1 Laser system setup	29
5.2.2 P1 scribe line	30
5.2.3 P2 scribe line	31
5.2.4 Transmission line method	31

5.2.5	P3 scribe line	33
5.2.6	Module laser scribing	34
5.3	Overview of the module processing.	34
5.4	Characterization of the solar module	34
6	Results and discussion	37
6.1	Set up of the ADEM Laser System	37
6.2	P1 scribe line	39
6.3	P2 scribe line	42
6.3.1	TLM measurements	45
6.4	P3 scribe line	46
6.5	Overview of the laser system parameters.	48
6.6	Module processing	48
6.6.1	Reference cell characterization	51
6.6.2	Module characterization	52
6.7	Additional P2 scribe	56
7	Conclusions and recommendations	57
7.1	Conclusions.	57
7.2	Recommendations	58
	Bibliography	59
A	Ablation threshold	65
B	Power scan for the P1 scribe	69
C	Power scan for the P2 scribe	73
D	Transmission Line Measurement	77
E	P3 power scan	79
F	Transmission Line Measurement for the processed modules	81

LIST OF FIGURES

1.1	Energy share and electricity production through the time	1
1.2	Fuel share of CO_2 emissions and CO_2 emissions per fuel through the time	2
1.3	Global energy potential	2
2.1	Perovskite cubic crystal structure	5
2.2	Diagram of the phase transition observed for lead and tin iodide perovskites	6
2.3	Statistics of control and Cs-based cells	7
2.4	Achitecture of a semi transparent perovskite solar cell	8
2.5	Working principle of a perovskite solar cell	10
2.6	Relevant energy levels of the TiO_2 , perovskite and spiro-OMeTAD junction	10
2.7	Semitransparent perovskite-based device developed at Solliance	11
3.1	Overview of perovskite module processing	13
3.2	Effect of the temperature of deposition on the ITO film structure	14
3.3	SnO_2 thin-film deposited via spin coating	15
3.4	Cross-sectional view of a processed cell with vapor and solution-based perovskite film	16
3.5	Main components of the sputtering magnetron technology	17
3.6	Main steps of the spin coating process	18
3.7	Effect of the anneal temperature during the post-treatment on a perovskite layer	19
4.1	Absorption emission of energy at the atomic level	21
4.2	Beam-matter interaction: short vs. ultrashort pulse length interaction	23
4.3	Absorbance spectrum of ITO-coated on glass	23
4.4	Absorption spectrum of SnO_2 nanoparticles	24
4.5	Absorbance spectrum of triple cation perovskite	24
4.6	Absorption spectrum of spiro-OMeTAD	24
4.7	Cross section of a processed perovskite module	25
5.1	Schematics of the ADEM laser system	29
5.2	Gaussian beam profile	31
5.3	Schematics of the four-probe TLM	32
5.4	Setup of the TLM to characterize contact and sheet resistance	32
5.5	Current transfer from semiconductor to the electrode material	32
5.6	Fitted line of the Total resistance R_T vs. length L for the TLM measurements	33
5.7	Layout of the laser scribes of the module	34
5.8	Overview of the perovskite module processing	35
6.1	D^2 of ablated spot vs pulse energy/ D^2 of ablated spot vs fluence for home sputtered ITO	38
6.2	D^2 of ablated spot vs pulse energy/ D^2 of ablated spot vs fluence for commercial ITO	38
6.3	Schematic view of the spots overlap	39
6.4	Crystallization effect on amorphous ITO	40
6.5	Crystallization effect on amorphous ITO	40
6.6	Power effect on ITO scribes	41

6.7	Scribe speed effect on ITO scribes	41
6.8	Apparent power effect for the P2 scribed lines	42
6.9	Cross sectional profiles of the P2 scribe	42
6.10	Comparison of diverse samples for the first P2 power scan	43
6.11	Microscopy analysis for the most suitable settings for the P2 scribe	44
6.12	Total resistance R_T versus distance d of a selected scribed interconnection	45
6.13	Contact resistivity ρ_c for selected P2 scribe settings	46
6.14	P3 scribes power scan	46
6.15	P3 scribed line topography analysis	47
6.16	P3 scribed line elemental analysis	47
6.17	P1 scribing line characteristics	48
6.18	Effect of substrate clean after P0 and P1 scribing	49
6.19	Morphology of SnO_2 , perovskite, and spiro-OMeTAD layers	49
6.20	P2 scribing line characteristics	50
6.21	P3 scribing line characteristics	50
6.22	Outline of the scribe processing	51
6.23	IV curves of reference cell under illumination and dark	51
6.24	IV curves for the working modules	53
6.25	IV curves for the modules illuminated from the rear side	54
6.26	Photoluminescence test for perovskite modules	55
6.27	Lock-in thermography test for perovskite modules	55
6.28	Dark lock-in thermography test for perovskite modules	56
6.29	Additional P2 scribe test	56
A.1	Apparent power vs measured power of laser beam, in mW	65
A.2	D^2 of ablated spot vs pulse energy/ D^2 of ablated spot vs fluence	67
D.1	Contact resistivity ρ_c for selected P2 scribe settings	78
E.1	Total resistance R_T versus distance d of a selected scribed interconnection	81

LIST OF TABLES

6.1	Maximum pulse energy in $\mu J/pulse$ for each pulse length and frequency	37
6.2	Threshold parameters for ITO samples ablated with UV laser	39
6.3	Conduction test of the power scan for the commercial ITO	40
6.4	Conduction test of the power scan for the home sputtered ITO	40
6.5	Selected settings for each scribe line	48
6.6	Reference cell characteristics under illumination in backward and forward scan	52
6.7	Complete characterization of the semi transparent perovskite modules.	53
6.8	Complete characterization of the semi transparent perovskite modules with rear illumination. Forward scan	54
A.1	Real power and pulse energy for each frequency	66
A.2	Real power and pulse energy for each frequency pulse length at 10 kHz frequency	66
A.3	Real power and pulse energy for each frequency pulse length at 50 kHz frequency	66
A.4	Ablation of ITO samples for commercial and home sputtered ITO	67
B.1	First power scan for the commercial ITO	69
B.2	First power scan for the home-sputtered ITO	70
B.3	Second power scan for the commercial ITO	70
B.4	Second power scan for the home-sputtered ITO	71
B.5	SEM images for isolating lines in commercial ITO samples	71
B.6	SEM images for the isolating lines in home-sputtered ITO samples	72
C.1	Confocal microscope images for the first power scan for the P2 scribed line	73
C.2	Cross-sectional images for the first power scan for the P2 scribed line	73
C.3	Confocal microscope images for the second power scan for the P2 scribed line	74
C.4	Cross-sectional images for the second power scan for the P2 scribed line	74
C.5	SEM images for selected cases of the second power scan for the P2 scribed line	75
D.1	Resistivity and resistance of Au-ITO and ITO-ITO contacts scribed with 1200 mW	77
D.2	Resistivity and resistance of Au-ITO and ITO-ITO contacts scribed with 1250 mW	77
D.3	Resistivity and resistance of Au-ITO and ITO-ITO contacts scribed with 1300 mW	77
E.1	Confocal microscope images for the first power scan for the P3 scribed line	79
E.1	Resistivity and resistance of ITO-ITO contacts scribed with 1300 mW	81

ABBREVIATIONS

- ABL** anode buffer layer. 9, 15, 28
- CPE** Conversion Power Efficiency. 3, 6, 7, 9, 10, 53, 57, 58
- DC** direct current. 27
- EDS** Energy Dispersive Spectroscopy. 31, 33, 35, 43, 44, 47
- ETL** electron transporting layer. 7–10, 14, 58
- FF** fill factor. 7, 8, 51, 52, 54
- GFF** geometrical fill factor. 25, 34, 41, 50, 54
- HOMO** Highest Occupied Molecular Orbital. 10
- HTL** hole transporting layer. 7, 9, 10, 15, 28, 43, 44, 58
- IEA** International Energy Agency. 1, 2
- IR** Infrared. 23, 28
- ITO** indium tin oxide. 8–10, 13, 15, 16, 23, 25, 27, 30, 32–34, 37–48, 51, 53, 57, 66, 67, 69–71
- KRICT** Korea Research Institute of Chemical Technology. 3
- LUMO** Lowest Unoccupied Molecular Orbital. 9
- NIR** Near infrared. 15
- NREL** National Renewable Energy Laboratory. 3, 10
- OPV** organic photovoltaics. 3, 8–10, 14, 15, 17
- RF** radio frequency. 27
- SEM** Scanning Electron Microscope. 30, 31, 35, 41, 43, 44, 47, 71, 72, 75
- SKKU** Sungkyunkwan University. 6
- spiro-OMeTAD** 2,2',7,7'-tetrakis(N,N-di-p-methoxyphenyl-amine)9,9'-spirobifluorene. 9, 10, 15–18, 23, 24, 27, 28, 34, 42–44, 47, 49, 52, 54–57
- ST** semi-transparent. 10, 15
- TCO** transparent conductive oxide. 7, 8, 10, 15–17, 27, 45
- TLM** transmission line method. 31–33, 45, 50, 57
- UV** Ultra-violet. 9, 23, 29, 37–39, 49, 57, 58

NOMENCLATURE

- A_C contact area. 32
- E_C Conduction band. 8
- E_F Fermi level. 8
- E_{pulse} pulse energy. 29
- F_{th} threshold fluence. 30
- J_{SC} short-circuit current. 7, 8, 51, 52
- L contact length. 33
- L_T limited transfer length. 33
- P_{real} real power (measured power). 29
- R_C contact resistance. 32
- R_S series resistance. 25
- R_T total resistance. 31, 45, 81
- R_{ITO} ITO electrode resistance. 33
- R_{SH} sheet resistance. 14, 15, 27, 31, 33
- R_{TC} total contact resistance. 31, 33, 43, 81
- V_{OC} open-circuit voltage. 7, 8, 51–54
- W_a active area width. 25
- W_d dead area width. 25
- Å Angstrom. 6
- μL microliters. 28
- μ_h hole mobility. 9
- μm micrometers. 29, 30, 38, 39, 41, 42, 44, 47–50, 56, 66, 67
- ρ_c specific contact resistivity. 31–33, 45, 46, 50, 57, 78
- °C degree Celsius. 14, 15, 18, 19, 28
- d distance. 31, 45, 81
- e^- electron. 9, 10
- f_0 peak fluence. 30

- f_{laser} laser frequency. 29, 30
- h^+ hole. 9, 10
- w width. 31
- Ar** Argon. 16
- Ar⁺** Argon ion. 16
- Br** Bromine. 5, 6
- C** Carbon. 43, 44, 47, 55
- Cl** Chlorine. 5
- CO₂** Carbon dioxide. 2
- Cs** Caesium. 5–7
- CsI** Caesium iodide. 28
- DMF** Dimethylformamide $(CH_3)_2NC(O)H$. 15, 28
- DMSO** Dimethyl sulfoxide $(CH_3)_2SO$. 15, 28
- eV** electronvolt. 3, 8–10
- FA** Formamidinium. 5–7
- FAI** Formamidinium iodide $CH(NH_2)_2I$. 28
- fs** femtoseconds. 22, 29, 37, 65–67
- GW_p** gigawatt peak. 3
- Hz** hertz. 29
- I** Iodine. 5, 6
- In** Indium. 43, 44, 47
- K** Kelvin. 6
- kHz** kilohertz. 29, 30, 37–39, 57, 65–67
- MA** Methylammonium. 5–7, 9, 10
- mA** milliampere. 7, 28, 52, 53
- MABr** Methylammonium bromide CH_3NH_3Br . 28
- mbar** millibar. 15, 16, 28
- mm** millimeter. 27, 28, 34, 50

MoO₃ Molybdenum trioxide. 9, 15, 16, 28, 34, 42, 43, 54, 57

mV millivolt. 7, 51, 52

mW milliwatt. 37–48, 56, 57, 65, 69–71, 73, 74, 77–79, 81

nm nanometers. 15, 23, 27–29, 37, 42–44, 47, 48, 53, 54, 56, 57

Pb Lead. 5, 15, 43, 44, 47, 55

PbBr₂ Lead(II) bromide. 28

PbI₂ Lead(II) iodide. 28

ps picoseconds. 22, 29, 37–39, 57, 65

rpm revolutions per minute. 28

Sn Tin. 5

SnO₂ Tin dioxide. 8, 9, 14–16, 18, 23, 24, 27, 28, 34, 43, 48–50, 52, 53, 56–58

TiO₂ Titanium dioxide. 9, 10

V volt. 16, 52

W watt. 29

1

INTRODUCTION

1.1. MOTIVATION

The relevance of fossil fuels such as coal, crude oil and other non-renewable sources of primary energy is a deep-rooted trend. The hindering factor is the increase of the energy demand from the world powers such as Europe and North America and the dynamic emerging nations such as China and India. The increase in the living standards in the developing economies is also an influential factor in the already growing energy demand. The depletion of fossil fuels to produce electricity, gas and refined fuels is a process that runs since the industrial revolution; this energy source is nothing but the solar energy stored as chemical energy for millions of years. Furthermore, the use of fossil fuels as an energy source is directly related to the emission of greenhouse gases that enhance the global warming, harvesting the future of the humankind. Given all this, the use of renewable energy carriers such as solar energy is almost mandatory to cover the current energy demand and the upcoming needs for the future [1].

In its 2016 report, the International Energy Agency (IEA) states the high energy share of 81.1 % of the energy production covered by fossil fuels such as natural gas, petroleum, and coal (Figure 1.1). The percentage covered by renewable sources such as solar, wind and geothermal energy is 1.4 %. This figure is not comparable to other alternative sources, such as the current 10.3 % hold by biomass sources [2].

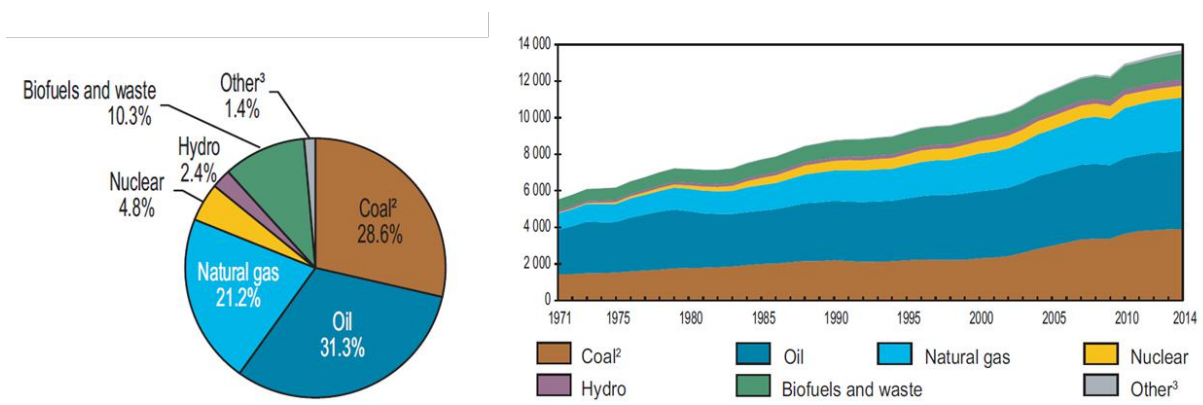


Figure 1.1: Energy sources share of the worldwide total primary energy supply according to the IEA (left side); Electricity generation by each fuel from 1971 to 2014 in mega tonne of oil equivalent (right side) [2].

Nonetheless, the combination of solar, wind and geothermal sources in the electricity production share reaches 6.3 %, while the fossil source production is depleted to 66.7 % by 2014. This

situation is also critical for the energy production trend, which has steadily increased in the last 40 years [2].

In terms of CO₂ emissions, the IEA reports a 0.5 % contribution of the total generation by renewable energy including biomass-based production (Figure 1.2. This value is almost neglected from the 32,400 megatons of CO₂ estimated in 2014. The right side of the Figure 1.2 shows a steady trend for fuel combustion, however the CO₂ emissions by coal combustion have duplicated compared to 1971 [2].

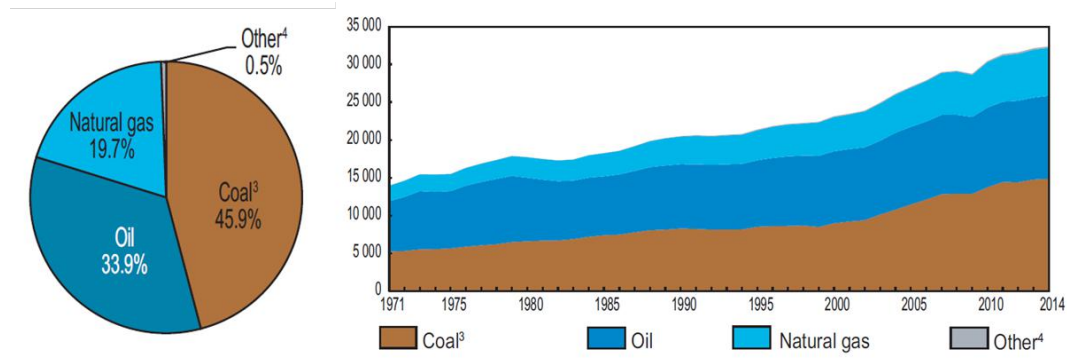


Figure 1.2: Fuel share of CO₂ emissions according to the IEA (left side); CO₂ emissions by each fuel combustion from 1971 to 2014 in mega tonne of oil equivalent (right side) [2].

The Figure 1.3 shows the energy demand estimated in 2015, calculated as 18.5 *TW*y/y. This figure is expected to reach 27 *TW*y/y by 2050. Regarding renewable sources, the global potential is estimated up to 23,150 *TW*y/y, of which 99 % is solar energy based. The use of solar energy as an energy supplier is remarkable than any other energy source, with a higher energy availability than the sum of all the finite energy reserves available on earth [3].

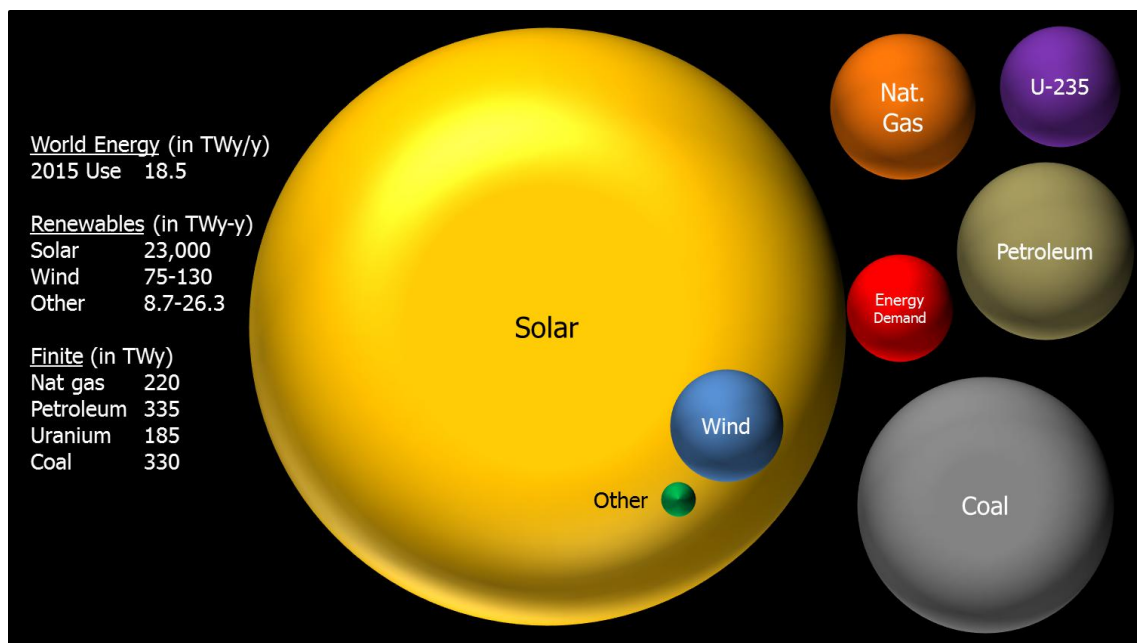


Figure 1.3: Global energy potential. Adapted from [3].

The photovoltaic cells are capable of the production of electricity from the Sun. These devices are mainly silicon-based materials. The total global installed capacity for grid-connected systems is

estimated in 306.5 GW_p in 2016 [4]. Thanks to the experience, better understanding and lowering cost of the technology, the industrial produced solar cells made of crystalline silicon are reaching the Conversion Power Efficiency (CPE) of 25.2 % [5], while the 26.6 % CPE value on research ambit has been static for several years [6].

The current concern of research is to improve the CPE for the devices up to 30 % and even transcend. This can be reached by the manufacture of multi-junction solar cells with diverse band gap materials, for the top cell. A low-cost thin-film solar cell technology is proposed for this purpose [7].

The metal-halide perovskite solar cells are a novel technology in organic photovoltaics (OPV) whose advances in performance, especially power conversion efficiency and stability, triggered the interest during the former years [8] [9]. In April 2017 the research team from the Korea Research Institute of Chemical Technology (KRICT) reported a stable device with 22.1 % CPE, the highest achieved for this technology according to the National Renewable Energy Laboratory (NREL) [10] [6]. This outstanding development has been reached only during the last 15 years [11]. Moreover, the perovskite solar cells prove to be a versatile material because of its tailoring properties such as the band gap, a property that is crucial for a possible tandem with a commercial wafer. A band gap of approximately 1.75 eV cell is needed to pair it with a 1.12 eV crystalline silicon [9].

The current perovskite-based technologies are in the laboratory scale, which creates the need of upscaling the devices. This thin-film technology has module prototypes with scribed interconnections, this technique can be done with mechanical and laser processed methods.

This project presents the development of a semi-transparent perovskite solar module by the optimization of the scribe processing to set the specifications of the laser system per each scribe line.

1.2. OBJECTIVE OF THE THESIS

This thesis aligns with the development of a semi-transparent perovskite module interconnection technology. This goal can be achieved by the correct set up of the laser beam for the scribing process and thus reduce the geometric and performance losses. The questions for this purpose are:

- What are the most suitable laser settings for each scribe?

The settings to define are wavelength, frequency, pulse length, power, and scribing speed. The influence of these factors on the scribes will be studied.

- How to determine the laser setup?

It is known that the ablation characteristics characteristics are dependent on the optoelectronic properties of the layers. Thus a literature review will help to approximate certain characteristics, such as wavelength of the laser. Besides, the scribed lines will be assessed with qualitative and quantitative methods, the critical factor in these evaluations is the possible side effects that the laser can inflict to the materials.

1.3. OUTLINE OF THE THESIS

Seven main chapters structure this material. The first three chapters handle the theoretical framework. The Chapter 2 shows the perovskite solar cell technology, the architecture of the stack, and working principle; the Chapter 3 handles the manufacturing of the perovskite solar cells and thin-film deposition techniques; Chapter 4 explains the working principle of the laser technology and its application to the solar module processing. The Chapter 5 shows the methodology for the experimental work and data processing. Chapter 6 summarizes the results, analysis and discussion. Lastly, Chapter ?? shows the conclusions of this study and propose an outlook for further work

2

PEROVSKITE SOLAR CELLS

The aim of this chapter is to explain the structure and importance of the perovskite materials in organic-inorganic photovoltaics. The architecture of a semi-transparent perovskite solar cell is described afterward, describing the materials and function of each layer. Eventually, the working principle of the devices is explained. Finally, this chapter shows the characteristics of the perovskite used for this project.

2.1. COMPOSITION AND STRUCTURE OF PEROVSKITE MATERIALS

The metal halide perovskites semiconductors are materials formed by two different cations and one anion described by the general formula of ABX_3 where A and B are the cations and X the anion (Figure 2.1). A is frequently cesium (Cs), methylammonium (MA) or formamidinium (FA), B is lead (Pb) or tin (Sn), and X the anion of iodine (I), chlorine (Cl) or bromine (Br) [12]. The use of lead as the B cation is proved to be a component for production of efficient solar cells. The Pb offers protection against oxidation with the induction of a deeper valence band. This effect also induces the increase of the material band gap [13].

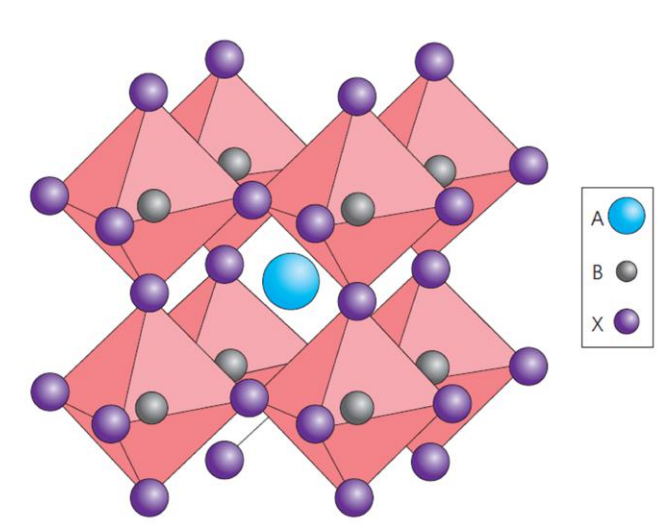


Figure 2.1: Perovskite cubic crystal structure, where A and B are cations of different size and X the anion [13].

Regarding structure, the perovskite can present two distinctive phases, known as the yellow and black phase. The yellow phase also called hexagonal δ -phase has photoinactive properties that

make it not suitable for photovoltaic applications. On the other side, if the crystallization reaches the black phase, also known as α -phase, the photocurrent can take place due to the photoactive properties of this state [14] [15]. Given this, it is necessary to use materials and methods to avoid the formation of the inactive material, which can also appear if the material reaches certain temperatures [15].

The Figure 2.2 shows an example of the phase transitions for lead and tin iodide based perovskite, with the α -phase fixed as the basal structure. This structure can convert into other structures via two pathways: if the black phase has a liquid interface, it can turn in the δ -phase if the temperature is below 260 K. On the other hand, when the α -phase is dried and cooled it converts in to the β -phase (below 200 K) or the γ -phase (below 130 K) [15].

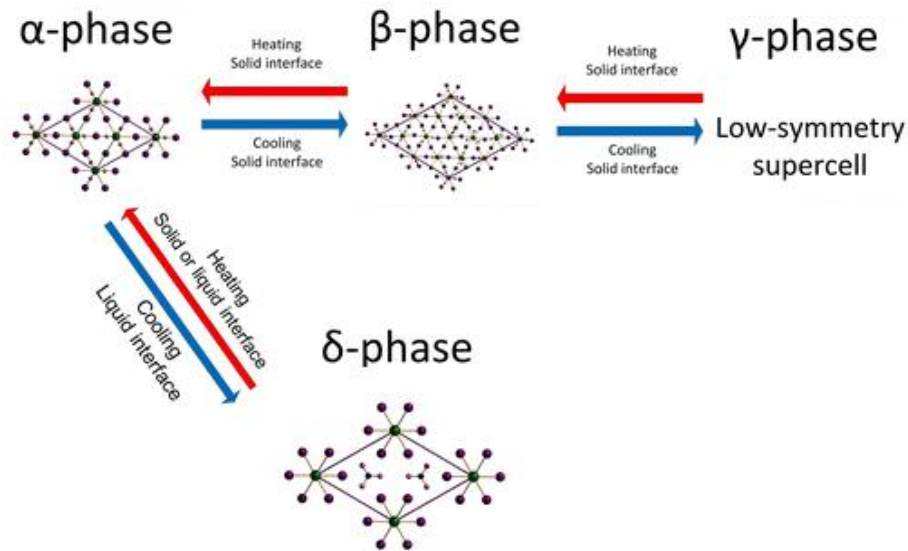


Figure 2.2: Diagram of the phase transition observed for the lead and tin iodide perovskites [15].

2.1.1.1. TRIPLE CATION PEROVSKITE

In recent works, a mixture of Methylammonium MA and Formamidinium FA has been tested. The double cation perovskite has an improved material quality regarding the structure and thermal stress tolerance. The MA acts as a stabilizer inducing the crystallization of the FA to the so-called black phase structure [14].

Nonetheless, Cesium Cs has attracted attention as a component for the mixed cation perovskite. Two alternative double-cation materials based on cesium Cs have been recently tested. A perovskite based on Cs and MA ($MA_{1-x}Cs_xPbI_3$) has been tested, reporting a final CPE of 8 % with an α -phase stabilized perovskite structure [16]. The team from the Sungkyunkwan University (SKKU), Korea reported a Cs-FA perovskite ($FA_{1-x}Cs_xPbI_3$) with an outstanding thermal and moisture stability through the lifetime and reaching a CPE of 16.5 % [17]. Yi *et al* states that mixing cations such as Cs and FA is energetic favorable in the α -phase, while on the other hand the δ -phase is hindered because the entropy cannot compensate the mixing process. The reported cells reached a CPE of 18 % with a halide mixture of I and Br [18]. McMeekin *et al* states that the perovskite-based materials have a tunable band gap by changing their compositions, this characteristic makes it suitable for tandem cell applications with silicon-based devices [9].

A new finding states that the ionic radius has a strong influence on the stability of the perovskite materials. The Cs has an ionic radius of 1.81 Å, while the MA and FA have ionic radii of 2.70 Å and 2.79 Å, respectively [14]. For the Cs-FA mixture, it can be tuned to improve the Goldschmidt toler-

ance factor, which indicates the stability and distortion of crystalline structures. This combination enhances the black phase crystallization since the difference in size of the ions is remarkable. It was also discussed in this section that MA could also improve the black phase in combination with FA [14]. However, the rate is lower if it is compared to the cesium blend material since the yellow photo inactive phase can be present in this blend. The almost same ionic radius of the molecules explains this situation [19].

Saliba *et al* shows an exceptional working device based on a triple cation of Cs-MA-FA with a stabilized CPE of 21.1 % and an efficiency of 18 % after 250 hours of operation (Figure 2.3) [14].

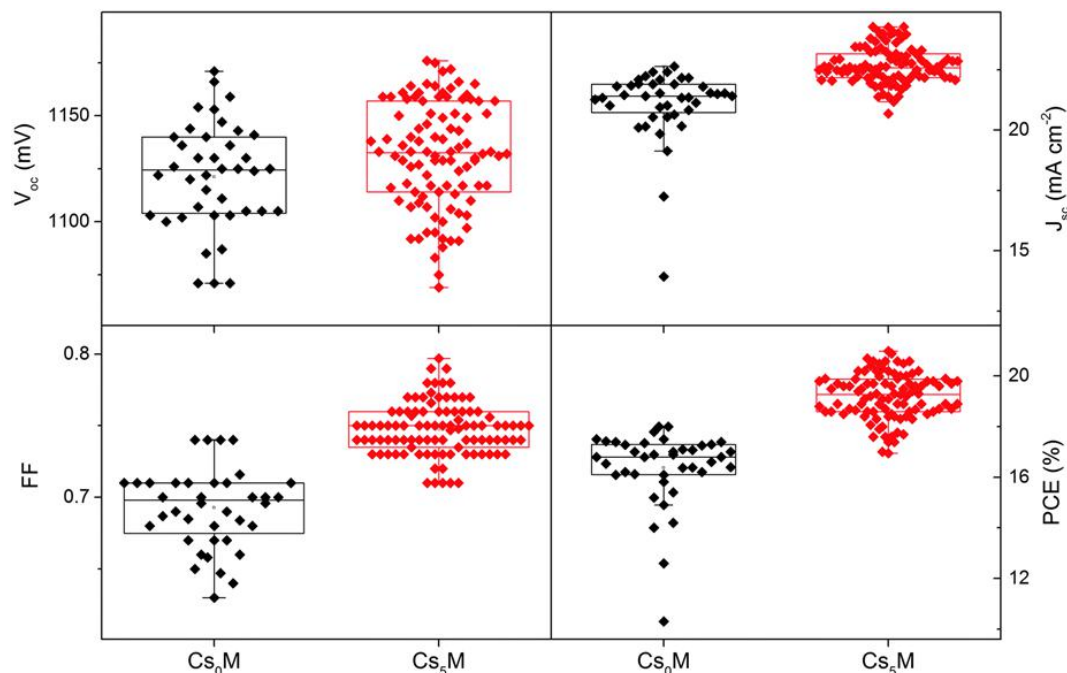


Figure 2.3: Statistics of control and Cs-based cells. This test has 40 control devices (Cs_0M) and 98 Cs-based cells (Cs_5M). The reproducibility can be appreciated in this scheme. The standard deviation is added to all the values. The V_{OC} had no significant variation from 1121 ± 25 mV to 1132 ± 25 mV. The J_{SC} improved from 21.06 ± 1.53 mA/cm² to 22.68 ± 0.75 mA/cm². The fill factor (FF) improved from 0.693 ± 0.028 to 0.748 ± 0.018 . The CPE improved from 16.37 ± 1.49 % to 19.20 ± 0.91 % [14].

This material avoids the yellow phase crystallization and presents a uniform film with grains that connect the electron transporting layer (ETL) with the hole transporting layer (HTL). Given the processing method of this layer, the triple cation perovskite is subject of high reproducibility [14].

2.2. PEROVSKITE CELL ARCHITECTURE

The components of this solar cell are the following layers from bottom to the top (Figure 2.4): glass, transparent conductive oxide (TCO) as the anode, ETL, perovskite layer, HTL and a rear TCO layer as cathode. This architecture is the so-called substrate device configuration, in which the light enters directly to the absorber layer [1]. Furthermore, the record efficiency cells have an architecture in such a way that the light enters into the ETL side [20].

Given the construction of the stack, the device is in the so-called n-i-p configuration, this is because the n-type layer (ETL) is deposited before the intrinsic layer (perovskite) and the final p-type layer (HTL). This configuration has the back contact deposited on the substrate (TCO). [1].

The most efficient perovskite solar cells utilize ETL also as the hole blocking layer (Section 2.3, and HTL as the electron blocking layer to dissociate the photogenerated charge carriers produced in the absorber layer. Plus, they help to avoid carrier recombination at the interface. Given that,

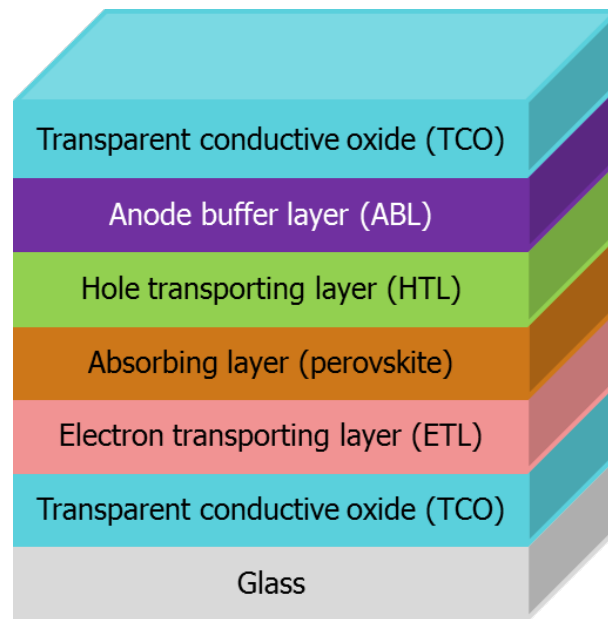


Figure 2.4: Architecture of a semi transparent perovskite solar cell (the layer thicknesses are not in scale).

these n-type and p-type layers are essential to achieve high efficiency devices in terms of V_{OC} and FF [20]

2.2.1. ELECTRODE LAYER

Since the primary interest of this perovskite solar technology is to achieve a good grade of transparency to couple it in a tandem stack, the usage of semitransparent electrodes is required [21].

The translucent front and rear electrode require a material with a good trade-off between transparency and transmission, often referred to as TCO [1]. For standard industrial applications, the indium tin oxide (ITO) is the preferred material, its lowest resistivity compared to similar materials and high transparency makes this compound suitable for OPV.

The ITO thin-film is a low-electrical resistive n-type material with a high carrier concentration, reflected in a resistivity value of $2 - 4 \times 10^{-4} \Omega cm$. In this material, the Fermi level (E_F) is situated above the conduction band (E_C), this degenerate state is possible due to the high doping of the layer. The doping is occurring during the layer deposition where oxygen vacancies and substitutional tin dopants are generated [22].

Moreover, the ITO in its oxidized state is capable to absorb light in the visible and infrared spectrum. Given the broad band gap of 3.5 – 4.3 eV the parasitic absorption effect is reduced [22].

The use of ITO, among other oxide layers, as an electrode has the potential capacity to decrease or even stop the fast degradation process in perovskite devices by creating a moisture barrier [21].

2.2.2. ELECTRON TRANSPORTING LAYER

For the ETL a metal oxide such as tin oxide SnO_2 is employed. This layer needs to be electron selective to facilitate the transport of negative charges from the perovskite to the electrode [23].

Ke et al. attributes the remarkable performance of SnO_2 due to the excellent optoelectronic properties of the SnO_2 films, such as fitting band gap positions, and especially a high electron mobility. These characteristics are reflected on the improved short-circuit current J_{SC} during the tests of the devices [20].

The requirements for high V_{oc} differs from high J_{sc} or high FF. Band bending is needed for V_{oc} , and difference in mobility for selectivity.

Typically, titanium dioxide TiO_2 is a commonly used n-type material. However, the poor electron mobility [20], high sensitivity to Ultra-violet (UV) light [24], and the suppressing of the flexibility of the cell [23] were remarkable drawbacks that commenced the research of alternative materials with more suitable properties.

The SnO_2 shows a proper alignment of the conduction band with the perovskite and SnO_2 by-products in the planar configuration. This property is essential to fabricate perovskite solar cells with high and stable CPE [8]. Additionally, SnO_2 has a wider gap compared to the TiO_2 , which compensates the parasitic losses of the ETL. However, this does not contribute with the final photocurrent of the cell [25].

2.2.3. HOLE TRANSPORTING MATERIAL

In OPV, the use of 2,2',7,7'-tetrakis(N,N-di-p-methoxyphenyl-amine)9,9'-spirobifluorene (spiro-OMeTAD) as the HTL is well-established. This compound is partially oxidized through an uncontrolled oxidative process to obtain discernible conductivity. This is because the layer increases the transport of positive charges [26] [27].

A drawback of this film is the reduction of the transparency of the final stack. The spiro-OMeTAD is a very opaque layer compared to the rest [26] [28]. Furthermore, the low intrinsic hole-mobility (μ_h), and thus a lower conductivity and the need of uncontrolled doping makes this process less reproducible [27].

2.2.4. ANODE BUFFER LAYER

The anode buffer layer (ABL) is indicated to avoid current leakage. This occurs when the transfer of electrons from the acceptor material to the HTL happens due to the direct contact of both the HTL ETL with the electrode layer [29].

The use of Molybdenum Oxide MoO_3 as the ABL in OPV started 20 years ago. In the first reported experiment, this layer was used between the HTL and the anode, and the final device presented a reduced voltage and increased efficiency. This is associated with the reduction of the hole-injection barrier in the interface created with the HTL. It is believed that the decrease of this barrier is caused by a dipole layer formed at the interface, which increases the vacuum level and consequently aligning the energy levels to a more favorable condition [30].

In addition to the improvement of performance, the MoO_3 layer provides further characteristics such as fewer pollutants on the electrode surface through the operation time, giving more stability to the material in the junction [30].

2.3. WORKING PRINCIPLE OF PEROVSKITE SOLAR CELLS

The band gap of the perovskite is approximately 1.5 eV [31]. This value is higher than the silicon band gap of 1.1 eV [1], due to this property the perovskite can absorb more photons with higher energy with less parasitic losses and utilize more energy of the total spectrum and reduce losses due to thermalization. The incident photons with a higher energy level than the energy gap of the semiconductor are absorbed, these energy packets excite the electrons to the conduction band and leave the holes in the valence band, bending the energy bands at the edges and causing separation of charges that are subsequently retrieved in the ETL (SnO_2 or TiO_2) and the HTL (spiro-OMeTAD) in the case of electrons e^- and holes h^+ , respectively (Figure 2.5). Therefore the charges move to be retrieved at the electrodes (ITO).

In order to enhance the mobility of the negative energy carriers e^- to the electrode the ETL needs to have a lower Lowest Unoccupied Molecular Orbital (LUMO) than the perovskite absorber layer [32]. The conduction band of the SnO_2 is approximately located -4.5 eV respect to the vacuum level, while for the TiO_2 this level is located -4.0 eV. Since the MA-based perovskite has a conduction band located at -3.93 eV (Figure 2.6) [33], this condition is satisfied and the mobility of the carriers

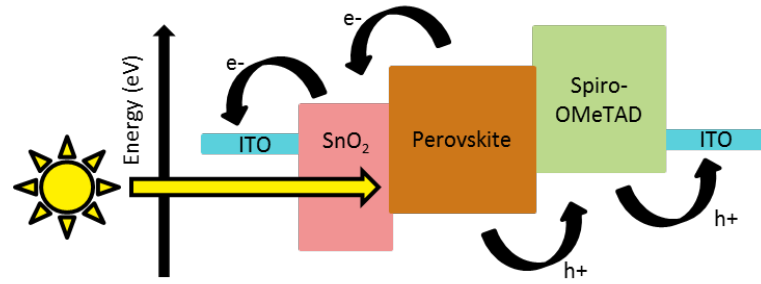


Figure 2.5: Working principle of the perovskite solar cell with the given architecture. Band gaps of the materials are not in scale

is possible at this side of the junction.

Respect to the positive charges h^+ , the HTL requires a higher Highest Occupied Molecular Orbital (HOMO) than the absorber layer [32]. In this case, the spiro-OMeTAD has a HOMO level of -5.22 eV respect to the vacuum level, while the MA-based perovskite layer has a value of -5.43 eV (Figure 2.6) [33]. Given that, this condition is also accomplished and form an efficient drive function for this junction.

After the transport of the holes h^+ and electron e^- energy carriers at the HTL and ETL, respectively, they continue to the front and rear contact of TCO to be collected and transmitted. This material also requires the satisfying of the level condition to assure the charge transport.

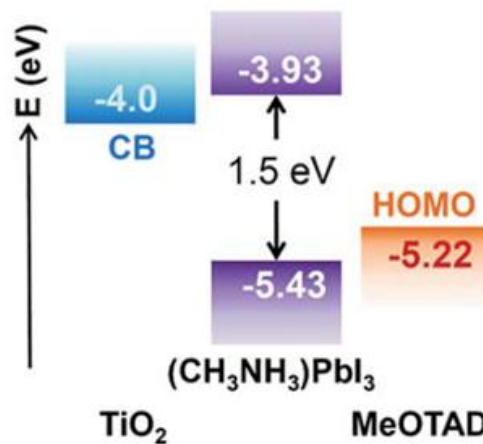


Figure 2.6: Relevant energy levels of the TiO_2 , perovskite and spiro-OMeTAD junction [32].

The CPE of this technology has surprisingly increased if the efficiency is compared between the first reported devices in 2006, when a 2.2 % CPE was reached [13]. Currently, a 22.1 % CPE has been achieved according to the NREL [10] [6]. The stability and resistance to thermal stress and moisture are some of the hindering factors for the introduction of this technology. Nonetheless, these characteristics have been improved among the CPE [13]. This technology still has the potential to develop in such a way that a good balance of performance and stability can be achieved.

The development of efficient semi-transparent (ST) devices is possible owing to the use of these materials. This transparency can be harnessed for architectural applications or tandem technologies [26]. In this case, the use of ITO as front and rear electrode helps to satisfy the semi transparency requirement (Figure 2.7).

It is clear that the use of perovskite materials as the light absorber layer in OPV is a novel and attractive option for the photovoltaic technologies.

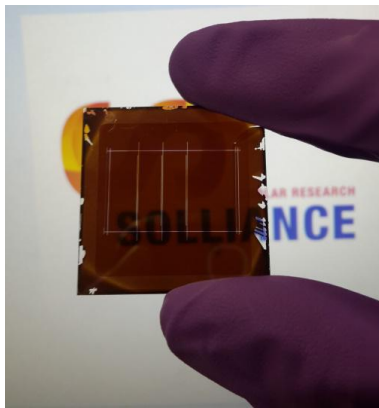


Figure 2.7: Semitransparent perovskite-based module developed at Solliance

3

PEROVSKITE SOLAR MODULE PROCESSING

The information of Chapter 2 creates a real insight of the components of a perovskite solar device. Given that, this chapter briefly explains the steps required for the stack manufacturing and the principle of its deposition methods

3.1. OVERVIEW OF THE MODULE PROCESSING

Each layer of the stack has distinctive chemical and physical properties that require different deposition methods to deposit a thin-film with the necessary characteristics and without compromising the adjacent layers, or the whole stack. These processes are critical for the performance of the cell, and this is mainly because of the thermal stress that is applied to the stack during the deposition. The Figure 3.1 gives a flow diagram of how the processing is handled in an n-i-p structure (substrate configuration).

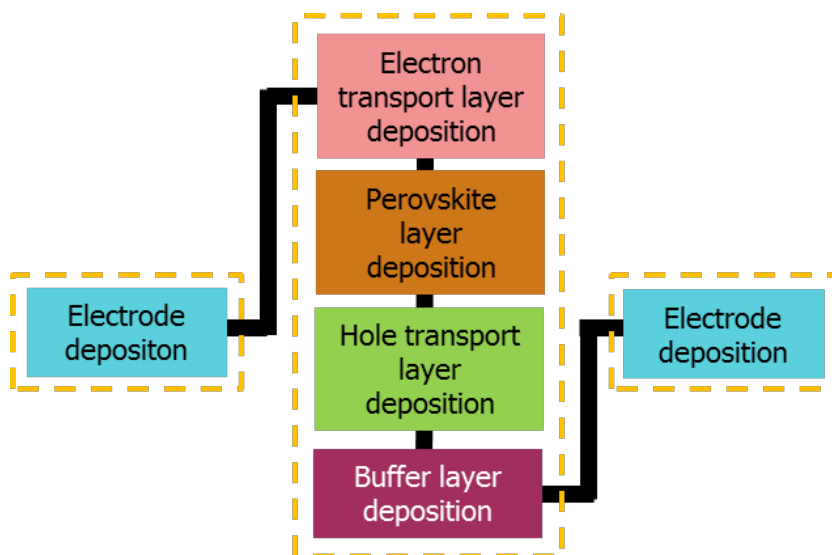


Figure 3.1: Overview of the perovskite module manufacturing. The yellow dashed line indicates a laser scribing step after the deposition.

The first layer deposited is the ITO electrode on a pre-cleaned glass substrate. The previous cleaning process is employed to annihilate undesired pollutants that can form recombination spots or compromise the uniformity of the layer. The deposition techniques for this film deposition are available, chemical vapor deposition, magnetron sputtering, evaporation and spray pyrolysis are

some alternatives. The main drawback of these methods is the temperature stress that they can inflict to the deposited films given the thermal properties and the high temperature of operation in the magnitude of 300 to 500 °C, mainly caused by the uniformity of the film that reduces the recombination places [22].

Regarding morphology, the low-temperature deposition forms a film with smaller and more uniform grains (Figure 3.2), This is because the reduced crystallization effect compared to the high temperature methods. In this case, the light transmittance is enhanced due to the relatively thin layers. Such characteristics are reflected in the optical properties, layers deposited at a lower temperature than 300 °C present more transmittance of the light spectrum with values around 80 %. This situation is because of the scattering of light caused by the roughness of the surface obtained at higher temperatures. In terms of electrical properties, the sheet resistance R_{SH} and resistivity ρ are strongly decreased with deposition temperature over 300 °C [34].

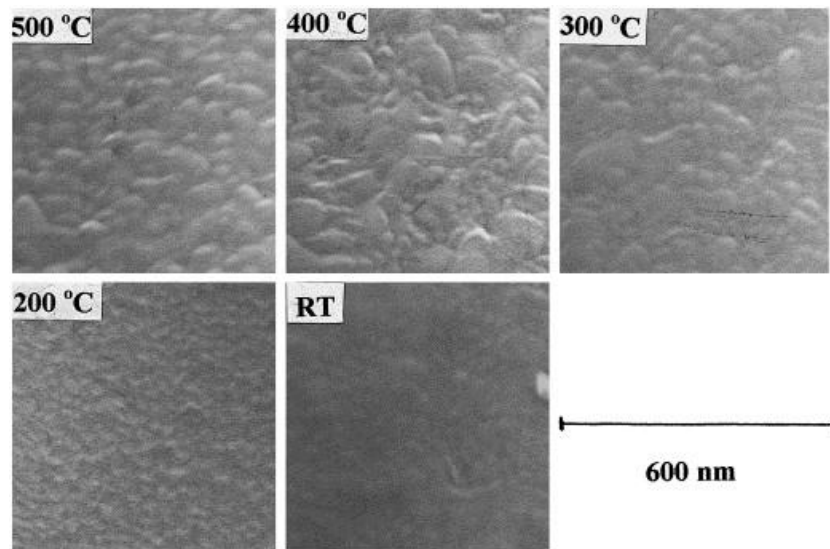


Figure 3.2: Effect of the temperature of deposition on the ITO film structure [34].

Given all this, the most common technology for the electrode deposition is magnetron sputtering (Section 3.2.1). It is important to mention that this process is performed at room temperature, and because of this the produced layer has an amorphous morphology without crystalline structures.

The second phase starts with the ETL deposition, since SnO_2 is the material to be deposited a solution-based process such as spin coating is the preferred method (Section 3.2.2) [20] because of the uniformity of the resulting layer and the relative ease to . After SnO_2 deposition a thermal treatment at 120 °C (Section 3.2.3) is applied [35]. The Figure 3.3 shows the layer morphology created under the depicted method. The structure is conformed by grains with a right alignment and continuous contact with the neighbor particles, the geometry achieved is the responsible for the path for electron transport through this layer [36].

This deposition can be carried out in a flow box without additional protective measures, since the SnO_2 and its water-based solvent are not health harmful.

In OPV there are several techniques to process a perovskite solar cell, they are mostly based on low temperature and solution-based methods because of their potential low cost production. These methods encompass spin coating, dip coating, thermal evaporation, among others. [8] [37]. The performance of the cell is directly related to the method of deposition and its operating conditions [37].

The perovskite layer deposition is performed by spin coating (Subsection 3.2.2) under inert con-

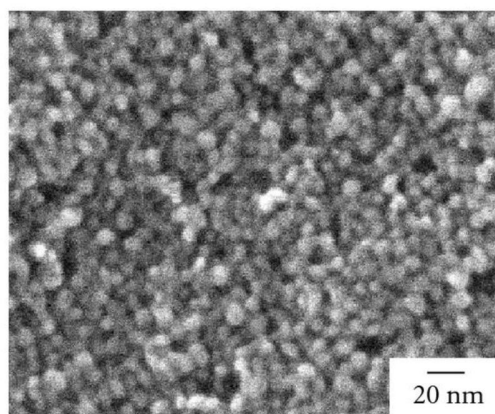


Figure 3.3: SnO₂ thin-film deposited via spin coating[36].

ditions, and this is because of the high reactivity of the perovskite material under moisture and oxygen exposure. Furthermore, the material is sensitive to thermal stress and, thus, the thermal post-treatment has to be performed under optimal temperature conditions [37]. In case of the triple cation perovskite, the annealing temperature is approximated in 150 °C

The process is carried out in a closed glove box that can assure inert atmosphere and isolation. This safety measure is because the presence of hazardous substances, such as lead Pb, and organic solvents DMSO and DMF during the deposition. Subsequently, an anti-solvent is applied to cure the film. This can be implemented in liquid or gas phase. Finally, the process is accomplished with a heat annealing step, which will be depicted at the end of this section (Subsection 3.2.3).

The HTL is deposited after the post-treatment of the perovskite deposition. This layer consists of a doped spiro-OMeTAD layer filed by the spin coating method (Subsection 3.2.2). This step is completed by the oxidation of this layer in a dry-air atmosphere.

The use of spiro-OMeTAD in its partial oxidized state is preferred in OPV. It has to be considered that the device loses transparency when this layer is applied. Furthermore, it is believed that this layer is related with the parasitic absorption of the device [26].

The ABL, in this case MoO₃, is usually deposited by vapor-assisted and solution-based methods. The first method deposits under vacuum conditions, where the pressure is around of 1×10^{-6} mbar. The process starts with the evaporation of the material contained in a crucible with an electrical heat system. Given the low absolute pressure of the chamber, the material evaporates at low-temperature conditions, and it passes through a shutter that sends the material to the substrates content on a rotating dome.

This method delivers a film with tunable thickness, from units to dozens of nm [38]. The second method uses spin coating (Subsection 3.2.2), which forms layers of 10 to 15 nm [39]. However, this step requires thermal annealing (Subsection 3.2.3), and this can compromise the stability of the adjacent layers. Nonetheless, *Liu et al.* proposes an alternative short-time annealing for a functional ABL, 10 minutes anneal process at 100 °C is proved as an alternative to the more thermal stressing methods [38].

In regard to the electrode layer, it should be considered diverse requirements. The ideal ST perovskite cell should have formidable transparency in the visible and Near infrared (NIR) regions, low sheet resistance R_{SH} , good adhesion to the stack, chemical stability and affinity with adjacent layers [23] [28].

The use of sputtered ITO as the front electrode meets the requirement of a low-temperature and solvent-free electrode deposition, since the perovskite and spiro-OMeTAD layers are temperature and solvent sensible [23]. Given all that, the rear TCO layer is deposited via magnetron sputtering

(Subsection 3.2.1) [32].

The Figure 3.4 shows the influence of the deposition method on the morphology of the layers: vapor-deposited layer has more continuity and uniformity than the solution-based depositions. Additionally, the probability of forming voids is reduced since the layer is continuous in thickness. This is because the continuous deposition in a well defined area that generates an homogeneous film. However, the vapor-based deposition technologies are not suitable for large scale applications due to the requirements to perform this [40].

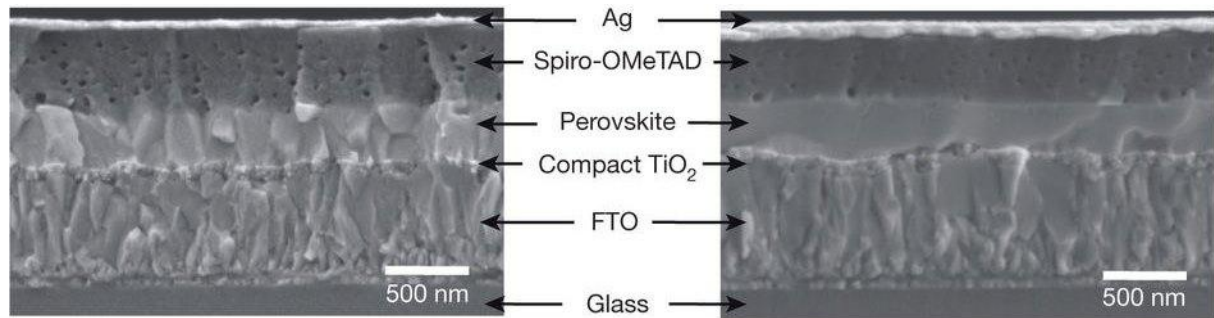


Figure 3.4: Cross-sectional view of a processed non transparent cell with vapor processed perovskite film (left) and solution-based perovskite film (right) [40].

3.2. THIN-FILM DEPOSITION METHODS

The perovskite solar cell is a thin film technology that requires different methods to deposit each layer of the stack. The selected technique is directly dependent on the chemical and physical properties of the material to be applied. The magnetron sputtering, spin coating and material evaporation at low pressure (Sections 3.2.1, and 3.2.2) are the techniques employed in the stack manufacturing for deposition of ITO (TCO), SnO_2 , perovskite and spiro-OMeTAD, and MoO_3 respectively. The next subsections will explain what is the working principle of each mechanism and its operating conditions to further justify their use for each layer of the module.

3.2.1. MAGNETRON SPUTTERING

The deposition of some layers such as the TCO (ITO) is performed by a sputtering technique described in this section.

The classical sputtering method begins with Argon atoms that are ionized (Ar^+) in a low-pressure chamber. This forms a phase of electrons and ions called plasma. This material state is well-known because of the emission of light (incandescence). This glow-discharge material bombards a surface with energetic ions (Ar^+) to remove selected atoms during collisions, which are finally deposited in a substrate layer on the substrate. The electrons ejected in this process collide with another Ar atoms leading to additional ionization [41] [42]. The Figure 3.5 shows the general components of the magnetron sputtering.

Magnetron sputtering is a technology that works under the principle of a parallel magnetic field that enhances electron motion of the target (Figure 3.5). The arrangement of the magnets in this system ensures the ionization efficiency, forming a highly condensed plasma in the desired region. The formed state increases the ion bombardment, enhancing the sputtering and consequently the deposition at the substrate. The operation conditions are approximately 10^{-3} mbar and 500 V [41].

The drawbacks of this conventional technique are the low deposition rates, low ionization efficiency, and high substrate heating effects [41].

An alternative to the conventional method is the direct radio frequency sputtering technology [41]. In the reactive mode, this method uses O_2 and N_2 as sputter gases [43]. A controlled oxygen

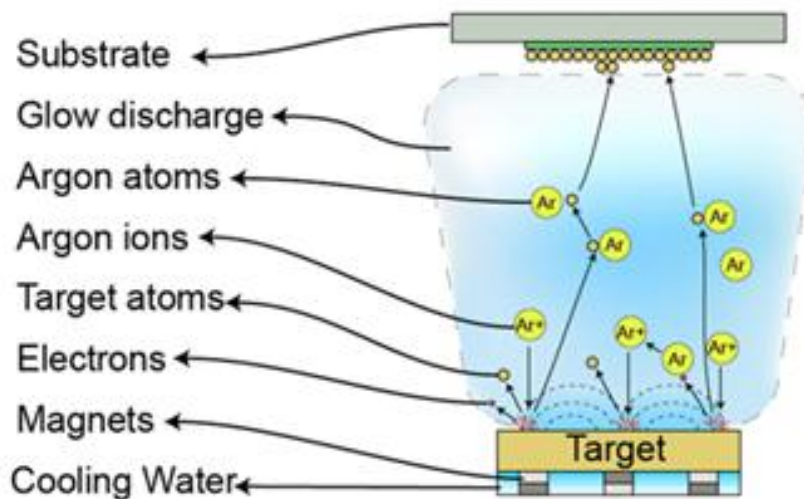


Figure 3.5: Main components of the sputtering magnetron technology [42].

atmosphere is required to make the reaction with metal to form the oxide [41].

This technology can deliver coating with unique optical and electrical characteristics [41]. Since the TCO needs to be transparent and highly conductive, this technology can deliver the desired parameters for the required layer. Another advantage of this method is the room temperature of processing since the perovskite layer, and spiro-OMeTAD layer are thermally sensitive, the top electrode should be deposited in a rather low-temperature process.

3.2.2. SPIN COATING

The spin coating is the leading procedure employed to produce thin-film layers from solutions in OPV at laboratory scale. The method is based on the use of centrifugal forces that spread the liquid towards the exterior of the surface in a radial direction. During the layer formation, the evaporation of the solvent is a major step of the process. The viscous force and surface tension play a significant part to produce a flat substrate [44].

About the effectiveness of the layer, some reports correlate the performance of the device with the thickness of the coat, and thus with the rotational speed and viscosity of the solution. The molecular organization in the interface, molecular orientation due to the shear field, formation of aggregates and diffusion of molecules on the film are some parameters that are directly related to the operation parameters [45].

The relationship between the film thickness, the rotational speed of the process and viscosity of the material can be expressed as in the equation 3.1.

$$d = k(\omega)^\alpha \quad (3.1)$$

Where ω is the angular velocity, and k and α are empirical constants related to the physical properties of the solvent, solute, and substrate. The viscosity of the solution is taken into account inside the factor k

This process is divided into four main steps (Figure 3.6). The fluid discharge from the center of the surface to obtain a uniform layer. The spin rotation spreads the solution and reaches such a speed that the liquid forms a thin film enough to rotate with the surface; stable fluid outflow where the substrate has a constant rotational speed, and the viscous forces govern the thinning phenomenon. This process delivers uniform layers when a volatile solvent is employed. Droplets are formed at the edge of the substrate droplets that are eventually dumped. Finally, the spin rotation ends, and the drying step begins when evaporation is the leading process that reduces the layer

thickness, the rate of evaporation is determined by the difference of partial pressure of the solvents, during the evaporation a liquid surface or solid layer is obtained [44].

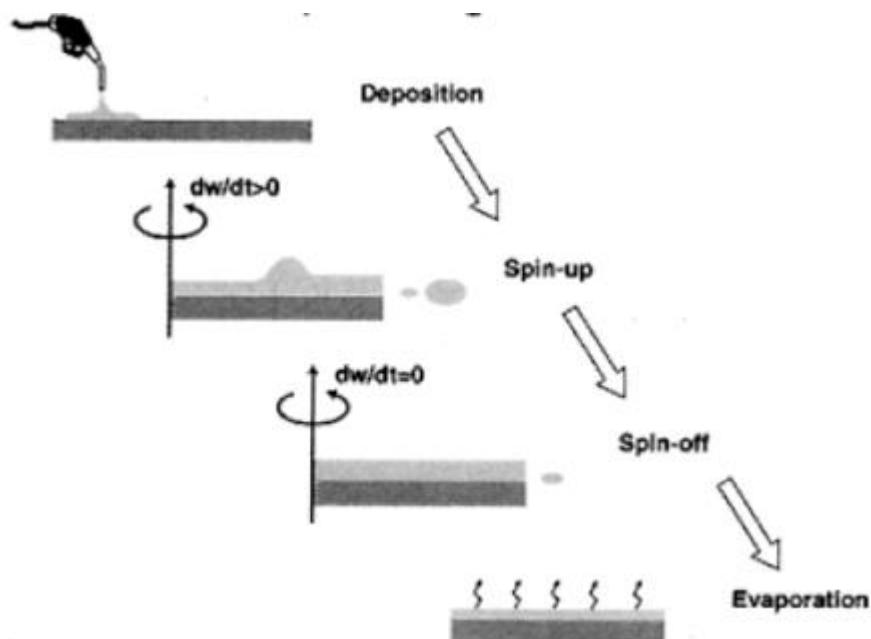


Figure 3.6: Main steps of the spin coating process [44].

The advantages of this robust technology are the modifiable film thickness through the change of rotational speed. Another edge is the progressive form of the uniform layer simultaneously to the thinning process. This process is well settled because of the fast and inexpensive operation conditions. The main drawback of this technology is the material utilization since only 2 to 5 % remains on the substrate and the rest is dumped and not recoverable. Despite this solution-loss on the process, the amount of required solution to form the layer is sufficient [44] [45].

Respect to the material characteristics, the SnO_2 , perovskite, and spiro-OMeTAD can be deposited with this method since it is a low-temperature pressure and does not compromise the chemical composition of the layers. Furthermore, with an adequate volume of liquid and rotational speed, a uniform layer can be produced. Nevertheless, the first two thin-films require a crystallization process to form the layer correctly. In light of that, a thermal post-treatment is applied (Section 3.2.3)

3.2.3. THERMAL ANNEALING

After the spin coating process, the thermal annealing is performed, this heat treatment completes the layer deposition by accelerating the reaction between molecules to enhance the thin film formation. However, the primary challenge of this treatment is to set the temperature and time of annealing. This processing is highly sensitive due to the characteristics of the deposited materials. Both organic and inorganic compounds tend to have fast reaction mechanisms, plus the temperature-dependent morphology of the layers which are closely related to the treatment conditions (Figure 3.7 [37]).

The temperature of operation is a critical parameter for the annealing. For instance, the perovskite layer can be annealed between $90\text{ }^\circ\text{C}$ and $170\text{ }^\circ\text{C}$. On the other side, the SnO_2 can be annealed at $150\text{ }^\circ\text{C}$ without compromising the film quality. However higher temperatures lead to lower surface coverage and thus poorer performance of the manufactured cell. This is because the irregularity of the layer can even lead to voids that propitiate the contact between the p-type and n-type

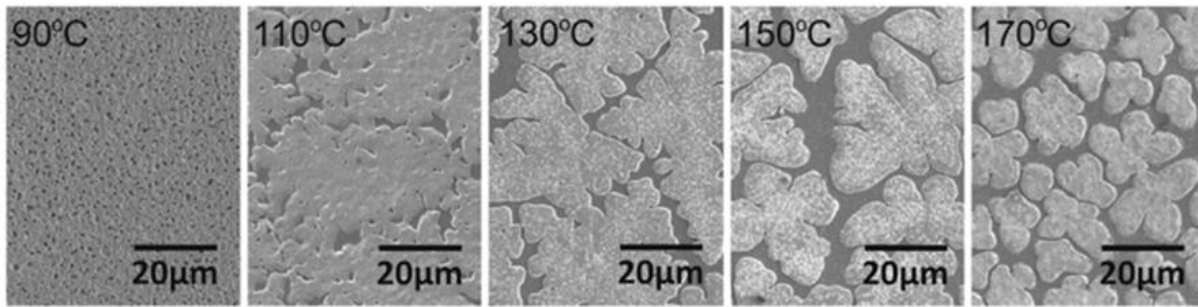


Figure 3.7: Effect of the anneal temperature during the post-treatment on a $MAPbI_{3-x}Cl_x$ -based perovskite layer [37].

layers forming shunting resistance [22].

The Figure 3.7 shows the effect of the temperature of annealing on a $MAPbI_{3-x}Cl_x$ -based perovskite, after 110 °C the film shows bigger grains that lead to less coverage until a temperature of 170 °C, where the void presence is evident through the layer. This effect is due to the perovskite degradation at high temperatures [37].

4

LASER TECHNOLOGY

The aim of this chapter is to present an overview the working principle of the laser and its application for ablation. Consequently, the use of this technology in photovoltaics will be explained. The last subsection mentions the characteristics and uses of each scribing line made with the laser for the device.

4.1. WORKING PRINCIPLE

The laser is an amplified beam of electromagnetic radiation. It emits photons with the same wavelength (monochromatic), phase (coherent) and with the same alignment (collimated). This results in a highly directional and high power density beam, different from the regular light [46] [47].

The three most important components of the laser are [47]: (i) The lasing medium can be used in different phases such as crystal, glass, dye, solvents, helium, CO_2 or semiconductors. The laser is commonly named after the material employed for this component. It also determines the wavelength of the produced beam. (ii) An energy source, also called pump, can be an electrical discharge, chemical reaction, diode, laser or flash lamp. The type of pump is defined by the material of the lasing medium. (iii) Optical resonator or cavity consists in 2 mirrors parallel aligned, one is highly reflective, and the other is partially reflective. The light escapes from the cavity to produce the output beam.

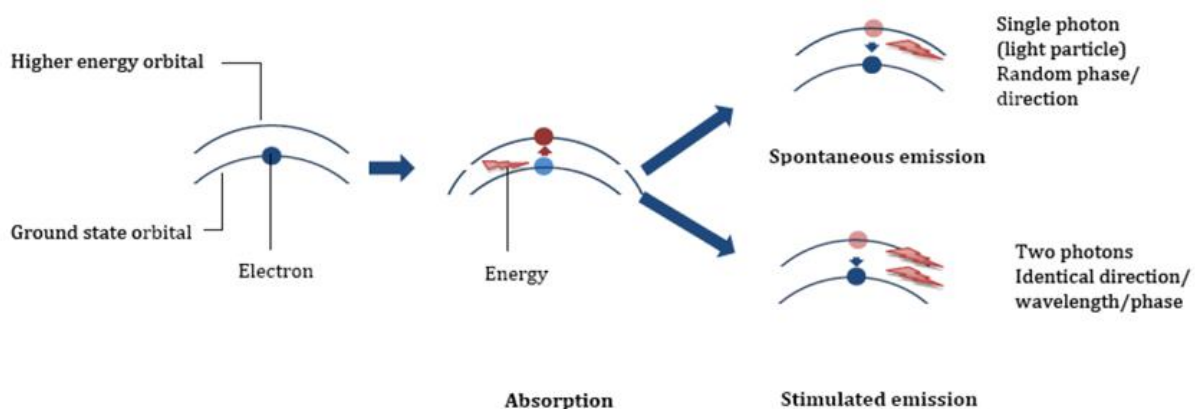


Figure 4.1: Absorption emission of energy at the atomic level [47].

At the atomic level (Figure 4.1), the process starts with the absorption of the energy in the atoms, whose electrons excite from low energy to a high energy state. In the next step, some negative-

charged particles with high energy levels lose energy in the form of photons with a wavelength determined by the difference between the excited and basal energy states, yet the phase and direction are rather random, this process is called spontaneous emission of photons [47].

During the last phase, the photons are reflected with the reflective mirrors at the resonant cavity and move back to the lasing medium. The reflection of photons and excited atoms leads to the decay of the atom to its basal state generating two identical photons regarding direction, phase, and wavelength, known as the stimulated emission of light [47].

4.1.1. MATERIAL - LASER BEAM INTERACTION

The incident beam excites the electrons of the material to high energy levels. This energy is dissipated in heat in a very short time lapse. Given this, the laser is a pure heat source [48]. Irradiation is the energy transfer phenomenon between the laser and the material. The use of mechanical scribing has been established for thin film technology, however the quality of the scribes can be improved by a laser-based process [46].

The effectiveness of the process is based on the optical and thermal properties of the material. Thus if the material has propitious thermal conductivity and diffusivity is suitable to be treated with this technology [46]. Another remarkable property of the materials is the ablation threshold, which is the lowest energy required of the laser to start the material displacement

This technology can be coupled to an automated system to build a complex machine with the ability to perform precise procedures. Given that, the laser is useful for the so-called laser beam machining. A technique used for material processing such as scribing, marking, cutting, drilling and so on [46].

4.1.2. PULSE LENGTH INFLUENCE ON THE ABLATION MECHANISM

In laser processing, two types of pulse length are present: the short pulse comprises micro- and nanoseconds pulse length, while the ultra short pulse includes the pico- and femtoseconds pulse length. The use of ultra short pulse length avoids the melting and thermal effects present in the classical short pulse. As the pulse duration increases the quality and reproducibility of the ablation decreases, this is because melting side-effects are present at short pulse scribing. On the other side, the ultrashort pulses involve almost neglect melting when the process is carried out near the ablation threshold [49].

In laser-assisted ablation, various beam-matter interactions are englobed. Heat conduction, melting, evaporation and plasma formation are present phenomena in laser scribing (Figure 4.2). The process starts with the energy applied to a surface, which absorbs it and form a temperature field through heat conduction. The melting step begins when the material reaches the required temperature. If the temperature surpasses this value, it can also form a vapor or plasma phase of the material. The next step is ejection of material via melt expulsion and evaporation, the pulse length and pulse energy are directly related to the dominance of melt or evaporation processes [46] [49].

Nonetheless, the classical model starts to lose validity in short microsecond pulse length, and thus cannot be applied for ultrashort pulse length such as pico- and femtosecond time scales (ps, fs). At ultrashort pulse length, the energy absorption has a different nonlinear trend. In this case, the material cannot pass to a vapor phase continuously due to the short interaction with the pulse. The mechanism is rather explained as a phase explosion, where the material experiments extreme temperature and pressure in a short period make material expansion rapidly (Figure 4.2) [49].

4.1.3. OPTOELECTRONIC PROPERTIES OF THE MATERIALS

The ablation by laser processing is not only dependent on the beam characteristics, but the material optoelectronic also plays a role on how the beam does interact with the matter. Each material can

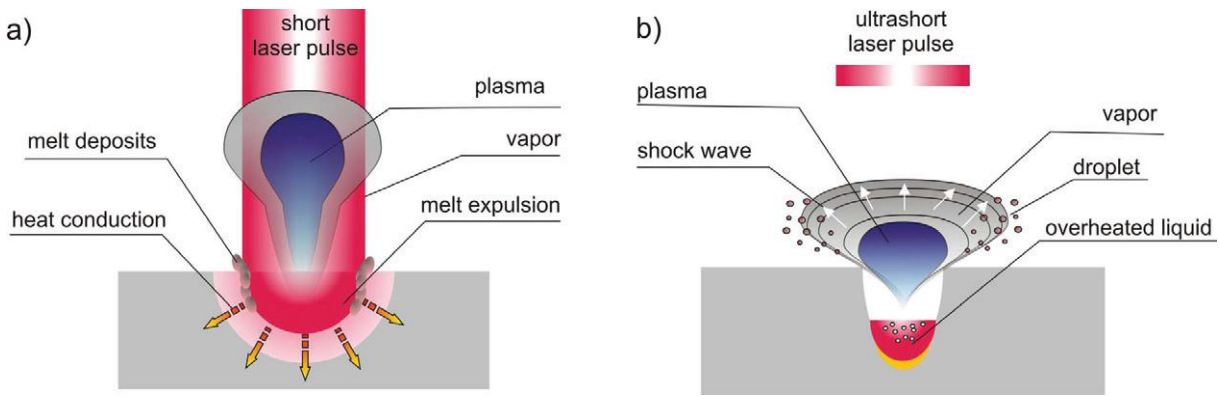


Figure 4.2: Beam-matter interaction: short pulse length interaction (a); ultrashort pulse length interaction (b) [49].

be transparent or opaque to certain wavelengths of the light spectrum. Given that, the settings of the laser and the quality of ablation are also determined by the match of optical properties and the wavelength of the laser.

In case of the front and rear-electrode ITO, the absorbance is considerable under 330 nm [50]. The Figure 4.3 shows the absorbance spectrum of a similar material to the ITO that will be tested in this project. The material is transparent to the green and Infrared (IR) wavelengths, and this can be translated into more energy intensive process when the UV laser is not employed.

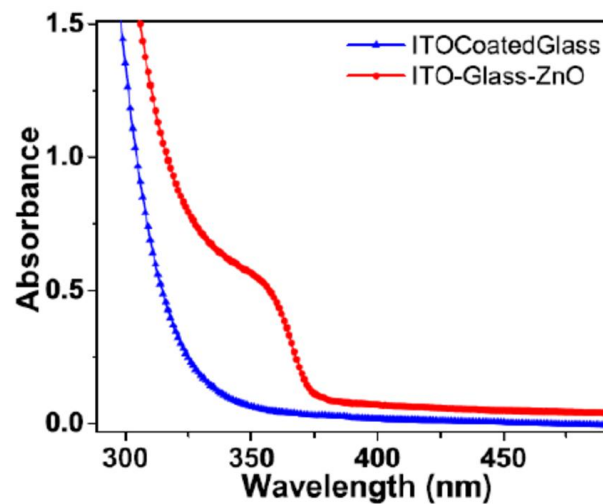


Figure 4.3: Absorbance spectrum of ITO-coated on glass [50].

With regard of the SnO_2 , the Figure 4.4 shows the absorption spectra of this material in its nanoparticle form. This chart shows a high absorbance for the UV wavelength. And high transmittance above 350 nm [51]/ This means that UV laser processing is also suitable for this layer

Concerning the triple cation perovskite, the Figure 4.5 shows the broad variety of wavelengths that this material can absorb. From UV to near IR, this material shows an average absorbance factor of 80 %. This also proves its compatibility with the absorbing material of the stack. In this case, wavelengths between 300 and 800 nm are sufficient to ablate the layer.

The spiro-OMeTAD has a slightly wider absorbance spectrum compared to the prior layers, and this is depicted in the Figure 4.6. In this case, the material has high affinity to wavelengths under 425 nm [52]. For this material, the green and IR lasers would require a higher amount of power and exposition time to correctly ablate the material.

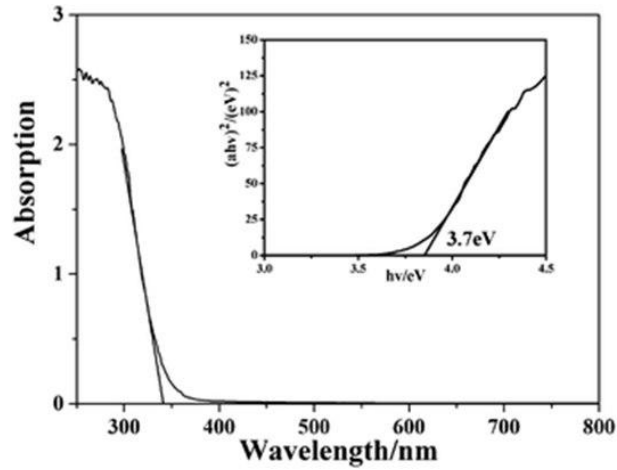


Figure 4.4: Absorption spectrum of SnO₂ nanoparticles in a.u. [51].

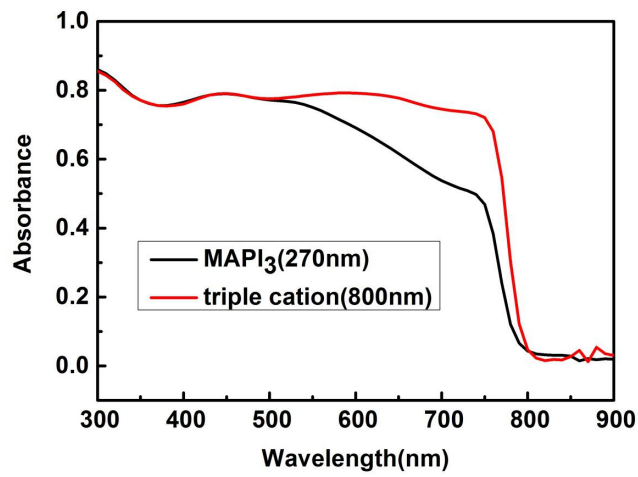


Figure 4.5: Absorption spectrum of triple cation perovskite, in percentage. *Measured at Solliance, Eindhoven*

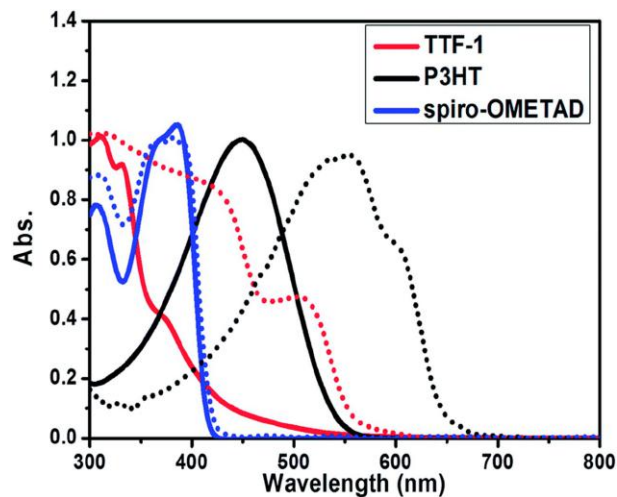


Figure 4.6: Absorption spectrum of spiro-OMeTAD. The solid lines indicate the substances in dichloromethane. The dashed lines indicate the spectra in thin film structure, in a.u. [52].

4.2. LASER IN ORGANIC PHOTOVOLTAICS

The thin-film technologies require the sectioning of the film to form series-interconnected cells to increase the voltage and maintain a constant current through the device [53]. The implementation of a standardized laser process on the production of organic-inorganic solar cells increases the potential of a high quality and reproducible production [54]. This is possible due to the uniformity of the laser scribes and the current deposition methods that produce samples with the same characteristics.

Laser processing is a technology that enables the scribing of the layers to obtain the desired architecture of the solar cell. For this solar cell, three scribing lines are required. These lines are defined as P1, P2, and P3. The P1 scribe ablates the substrate electrodes (ITO) to form cells. The semiconductor is removed of the ITO with the P2 scribe and an ohmic contact is formed after the deposition of the top electrode layer. Finally, the top electrode is scribed by the P3 forming single cells connected in series [54]. The P1 and P3 ablation have a high risk of shunting because of the emitted particles of this scribe, and therefore, shunt-losses [54].

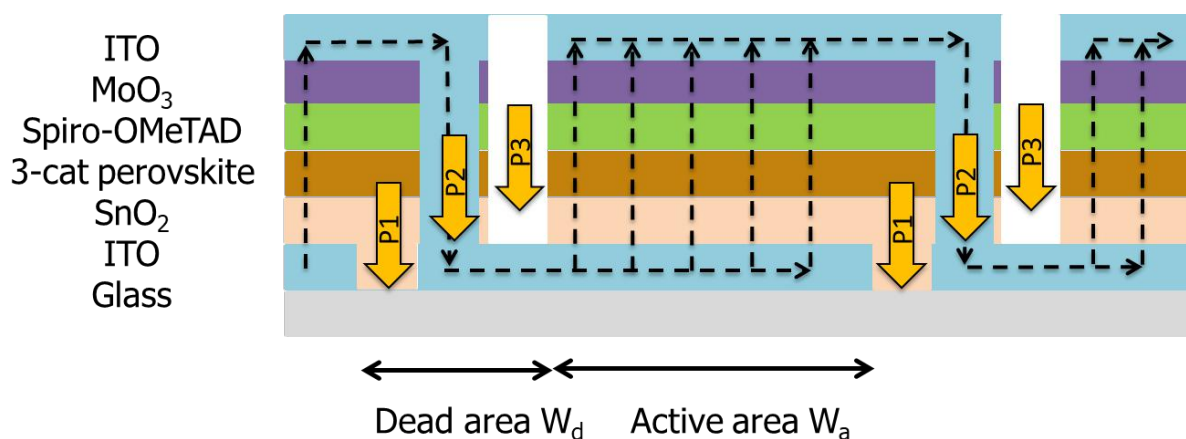


Figure 4.7: Cross section of prepared perovskite module. W_a is indicated as the photo active area, while W_d is the non-active "dead" area. The dashed lines represent the current flow within the device.

There are four possible scenarios to delve into the analysis of P2 scribe: (1) too low laser power does not remove the active layer efficiently, and series resistance (R_s) is increased. (2) Too high power compromises the ITO layer, leading to resistance losses or even the loss of interconnection. (3) A narrow P2 scribe line generates extra series resistance (R_s) if the interconnection between electrodes (ITO layers) is insufficient. (4) A wide P2 scribe line causes higher geometric losses [54].

The area between the scribing lines has no photo activity and this is considered as dead area (Figure 4.7). This region has a width W_d and considers the area of all the scribed lines. The area where the photovoltaic activity takes place has a width W_a . The geometrical fill factor (GFF) is known as the ratio of photo active area and the total area of the device, which can give the losses of the device due to line scribing.

The development of ideal laser settings is a challenge since complete removal of the individual layers is required without influencing the performance of the device. Possible damage by micro-cracks during the scribing process can produce short-circuits, hindering the efficiency of the device [55].

5

METHODOLOGY

The aim of this chapter is to describe in detail the experimental design of the project. This method has a base on all the information discussed in the previous sections. First, the selected deposition techniques and their operation conditions are considered for each layer regarding the material properties. Secondly, laser processing is described; starting from the setup of the laser and threshold determination, continuing with power scanning and characterization of the scribed lines. Finally, the optimal settings are used for the manufacturing of a module and the characterization methods are also depicted.

5.1. DEPOSITION METHODS

Given the architecture of the cell in the Section 2.2 the construction of the cell will be described in order of deposition. These devices have an n-i-p configuration, of which the architecture is also outlined in the Section 2.2. The selected processes for each layer deposition were optimized by Solliance engineers.

For the ITO samples two types of materials are tested: commercial full area ITO substrates of 30 x 30 x 7 mm with 10Ω /square R_{SH} , and home sputtered ITO by magnetron sputtering with 20Ω /square with less transparency compared to the commercial sampe. Subsequently, a SnO_2 layer is deposited by spin coating with post-treatment. Then, the absorbing layer (triple cation perovskite in this case) is deposited by two-step spin coating with thermal annealing. Furthermore, the spiro-OMeTAD is placed by two step processing. Finally, the TCO top electrode is deposited by magnetron sputtering.

5.1.1. ELECTRODE DEPOSITION

The substrates employed for this work are *Eagle glass* 30 x 30 x 0.7 mm. Since the glass needs to be free of pollutants, the samples are cleaned through rinsing and sonication in Extran® solution, demi-water, and isopropanol for 5 minutes, respectively. The use of Extran® solutions is to avoid the transference of residues to the samples after cleaning. The sonication and warming help to reduce the processing time. The demi-water sonication is recommended to rinse the Extran® to avoid the presence of ions on the substrate. The isopropanol solution helps to dry the humidity due to its high volatility. This drying process is enhanced by blowing a N_2 flow on the surface of the substrate.

Once the glass substrates are clean, the samples are handed to the *AJA sputtertool*. This machine is capable of performing radio frequency (RF) and direct current (DC) sputtering. In the case of an ITO layer, the RF magnetron sputtering mode is settled. This process is executed at room temperature and has a rate of 40 nm/hour. The obtained film has a 200 nm thickness with a R_{SH} of 20Ω /square.

5.1.2. ELECTRON TRANSMISSION LAYER DEPOSITION

The SnO₂ is deposited by spin coating. The *Spincoater LF bench* is employed for this step. It is important to mention that this method is made in a regular down flow system. The required substance is a 2.5 % SnO₂ solution diluted from a 15 % Alfa Aesar batch, processed at Solliance. 100 μ L are deposited under a one-step solution-based process at 3000 rpm during 50 seconds.

The annealing post-treatment is required for this case. The samples are treated at 120 °C for one hour. This treatment enhances the solvent evaporation and crystallization of the deposited material as described in the section 3.2.3.

5.1.3. PEROVSKITE LAYER DEPOSITION

This solution-based process uses triple cation perovskite solution to generate the film. The preparation of the solution and the deposition steps are performed inside a glovebox; this is because the perovskite solution has toxic components such as lead that can compromise the facility safety. The prepared solution contains FAI, PbI₂, PbBr₂, and MABr, dissolved in DMF and DMSO, and finally stirred with a CsI solution. For this deposition a *Spincoater GB* is used. The two-step deposition spins 50 μ L of solution at 3000 and 5000 rpm for 20 seconds, a post-curation with N₂ is done 12 seconds after the rotation starts. This deposition is done at room temperature.

Thermal annealing is also required for this layer (section 3.2.3). A stove with 150 °C is employed to anneal the samples for half an hour. During this step, the substrates reduce the transparency considerably, so it becomes brownish.

5.1.4. HOLE TRANSMISSION LAYER DEPOSITION

The spiro-OMeTAD is deposited via spin coating as the HTL. This solution is also hazardous since its solvent is chlorobenzene. Therefore the handling of this material must be inside the glovebox. For this deposition, the *Spincoater GB* is employed. The process is set as a two-step deposition with 2000 and 5000 rpm in 50 seconds. For this layer 65 μ L are required. This layer does not require annealing post-treatment. Nevertheless, an overnight dry atmosphere is required for curing the cell.

5.1.5. ANODE BUFFER LAYER DEPOSITION

The MoO₃ (ABL) is deposited via physical vapor deposition at low pressure mode. A 20 nm layer is deposited at 1×10^{-6} mbar. This process is performed with a starting rate deposition of 0.1 Å/s to finally achieve a rate of 0.5 Å/s at a source current of 700 mA.

5.2. LASER SCRIBING

The function and characteristics of each line are explained in section 4.2. Furthermore, the optical properties of the materials are shown in Section 2.2. With the information from both sections, the laser wavelength can be approximated. An ablation threshold is determined with a power scan on each substrate, this is followed by laser scribing experiments, where the pulse overlap is tuned by changing the laser energy, scribing speed and frequency.

The experiments are carried out in the *ADEM system* facility at ECN, Eindhoven. The laser system is a *Pharos femtosecond laser model 10-200-PP* manufactured by *Light conversion*. This system possesses an IR laser source that is possible to be modified to green and ultraviolet outputs through a system of crystals that are capable of duplicating the frequency and filter its harmonics. The lens is a *Telecentric f-theta series S4LFT4010/75* manufactured by *Sill optics*. This lens has a short focal length translated in 35 x 35 mm optical field.

The Figure 5.1 shows the laser beam path. From the laser source, the beams pass through beam expanders, and are deflected towards the scanner head using stirring mirrors. After this step, the three beams are fused in one to make it move in a series of mirrors. Eventually, the three beams are separated with the mirrors arrangement in the head of the system. This head has a scanner per

wavelength, each scanner head contains two deflecting mirrors that control the laser spot on the irradiated surface, thus X and Y directions. The part of the system is also capable of moving in the Z direction to set the focus of the laser.

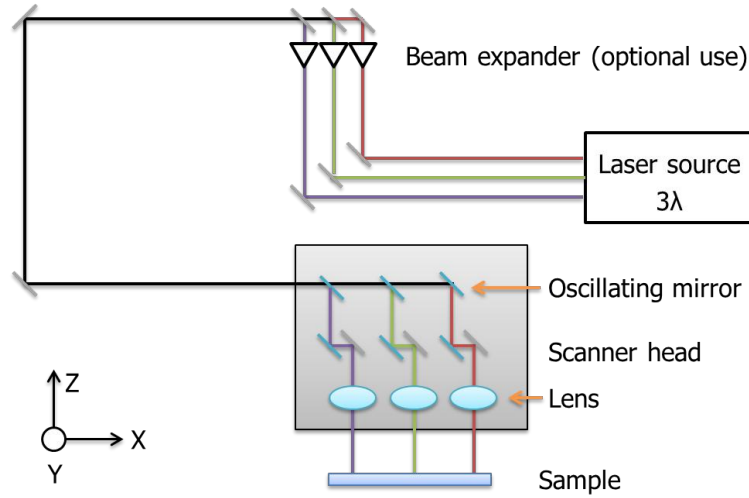


Figure 5.1: Schematics of the ADEM laser system.

The ADEM system can deliver three laser types as the output: infrared (1030 nm), green (515 nm), and ultraviolet (335 nm). This equipment has pulse length range from 200 fs to 10 ps. In terms of scribing speed, the laser system has a maximum speed of 2500 mm/s. The beam quality M^2 is 1.2, which is a good figure. This value represents the degree of variation of the beam from an ideal Gaussian beam [56]. The approximated spotsize obtained with the Telecentric f -theta lens is around 20 μm .

5.2.1. LASER SYSTEM SETUP

The energy delivered by the laser beam depends on a set of parameters such as frequency and power. The first parameter to define is the wavelength, with the analysis of the optical properties of similar materials in Chapter 4 it can be stated that the most suitable value is 355 nm, which is the UV wavelength.

The pulse length is the next parameter to determine. The section 4.1 discusses the advantages of setting the pulse length in ultrashort pulse duration such as picosecond and nanosecond magnitudes. Formerly in the ADEM system, the tested pulse lengths were in magnitudes of femtoseconds fs up to picoseconds ps. The Pharos femtosecond laser has a pulse duration range from 300 fs to 10 ps. The tested pulse length are 0.25, 1, 5 and 10 ps.

After this step, the frequency is defined. For this case, 10, 20 and 50 kHz are tested. This parameter limited the power range of the laser, as long as the frequency decreases, the operation power range is situated in lower values. For high power values the integrity of the system is compromised. The system emits a warning alert if the setting compromises the crystals and mirrors of the system.

The real power of the laser beam is measured by a power meter, the measurements and calculations are listed in Appendix A. The employed power meter measures the power in watts. Nevertheless, comparable data is given in $\mu\text{J}/\text{pulse}$. Thus a conversion of the data is required. The equation A.1 provides the necessary calculation for the pulse energy.

$$E_{\text{pulse}} = \frac{P_{\text{real}}}{f_{\text{laser}}} \quad (5.1)$$

Where the pulse energy E_{pulse} is given in J/pulse , the real power (measured power) P_{real} in W, and the frequency of the laser f_{laser} in Hz.

After the calculation of the pulse energy, the setup with the most similar values to the previous values obtained at Solliance ($6 \mu J/pulse$) is selected to start the ablation of the rear electrode.

5.2.2. P1 SCRIBE LINE

In the case of the bottom electrode substrate, there are two available substrates with different layer structures: commercial samples of ITO with a crystalline structure, and home-sputtered ITO layer with an amorphous structure due to the operation conditions of the deposition method. These substrates will be tested to compare the ablation of the laser in such different materials.

A single pulse ablation experiment is carried out to determine the ablation threshold of the ITO. For this test, it is required to calculate the scribing speed regarding frequency and distance between spots (Equation 5.2).

$$v_{scribe} = d_{spots} f_{laser} \quad (5.2)$$

Where d_{spots} is the distance between the center of two ablated spots in μm , and f_{laser} is the frequency of the laser beam in kHz, the scribe speed is calculated in mm/s . In the case of this test, it is preferred to have a high scribing speed to produce isolated spots. With the frequency and scribe speed fixed, a power scan is performed.

For the next step, it is necessary to measure the ablation depth d reached the beginning of the ablation and a certain threshold fluence F_{th} . This value can be determined with a semilogarithmic plot of d vs. peak fluence f_0 . The Lambert-Beer law is employed to understand the photochemical and photothermal ablation (Equation 5.3).

$$d = \frac{1}{\alpha_{eff}} \ln \frac{F_0}{F_{th}} \quad (5.3)$$

Where α_{eff} is the effective absorption coefficient of the material. which is used in the Bee-Lambert's law in the ablation regime, this is obtained with the ablation rate and fluence [57].

However, the ablation depth was difficult to measure with an optical microscope in thin-film materials. Given the situation, an alternative is to measure the ablated diameter D_{ab} with a microscope and plotting the square diameter D^2 versus laser fluence f_0 (equation 5.4). For this equation, $2\omega_0^2$ is the beam diameter in the focal plane.

$$D^2 = 2\omega_0^2 \ln \frac{F_0}{F_{th}} \quad (5.4)$$

The Figure 5.2 shows the correlation of the laser fluence and the ablated diameter, this charts shows the inverse proportion of both parameters. The image below also shows the possibility of relating the diameter of ablation and fluence of the laser beam.

The optimization of the P1 laser settings is achieved with a power scan where the wavelength, pulse length, and frequency were set to fixed values; and the apparent power and scribe speed as variable parameters. The scribing speed is a critical step to ablate continuous lines and avoid interaction between two ablated areas.

Two qualitative tests were used to evaluate the electrical isolation and quality of the scribed line. The first one consists in measuring the isolation of the material produced by the scribed lines with a multimeter. Once the ablated lines are identified as isolating, they are evaluated in the confocal microscope to observe the profile of the line and approximates its depth. Consequently, the samples are tested in the Scanning Electron Microscope (SEM) to find undesired effects such as cracking or delamination of the material.

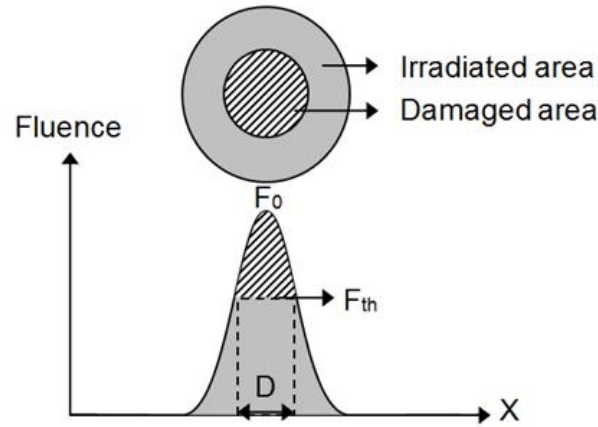


Figure 5.2: Gaussian beam profile

5.2.3. P2 SCRIBE LINE

The interconnection of the module is the critical step of the laser processing, as discussed in section 4.2.

The power scan is performed with the same wavelength, pulse length, and frequency from the P1 scribe; the apparent power and scribe speed are variable parameters. Concerning the apparent power, this value needs to be lower compared to the P1 setting scan to avoid the damage of the bottom electrode.

This scribed line is characterized by quantitative and qualitative tests, the subsection 5.2.4 explains the method to measure the resistivity of the contact formed by the top and bottom electrode, this value is intended to be as small as possible to guarantee a good conductance of the interconnection. The qualitative tests are both confocal and electronic microscopy. In this case, the SEM device is also used in Energy Dispersive Spectroscopy (EDS) mode, this allows to make an elemental analysis and see the presence of chemical elements and determine whether the laser removed the desired layers entirely, this is due to the variety of compounds to be removed by the laser for the P2 scribes.

5.2.4. TRANSMISSION LINE METHOD

The transmission line method (TLM) is used to determine the contact resistance between the front and rear electrodes of a cell through the use of a four-probe setup Figure 5.3. This is based on measuring the sheet resistance R_{SH} of a conductive film with a width w and distance d that connects two electrical contacts. The equation 5.5 shows the calculation of the total resistance R_T as the addition of the sheet resistance $R_{SH} \frac{d}{w}$ and the total contact resistance R_{TC} between the films and the electrodes [58].

$$R_T = R_{SH} \frac{d}{W} + 2R_{TC} \quad (5.5)$$

The experimental method consists in the variation of the electrode distances, where R_{SH} and R_{TC} are measured. Depending on the configuration of the measurements of the Figure 5.4, the sheet resistance R_{SH} of the front or rear electrode can be determined. With the determination of these parameters, a complete electrical characterization is performed [58].

The current of the device flows from the semiconductor to the electrode material and if this faces the resistances specific contact resistivity ρ_c and sheet resistance R_{SH} . The semiconductor-electrode contact can be expressed with the equivalent circuit of the Figure 5.5, where the current selects the least resistance path [60].

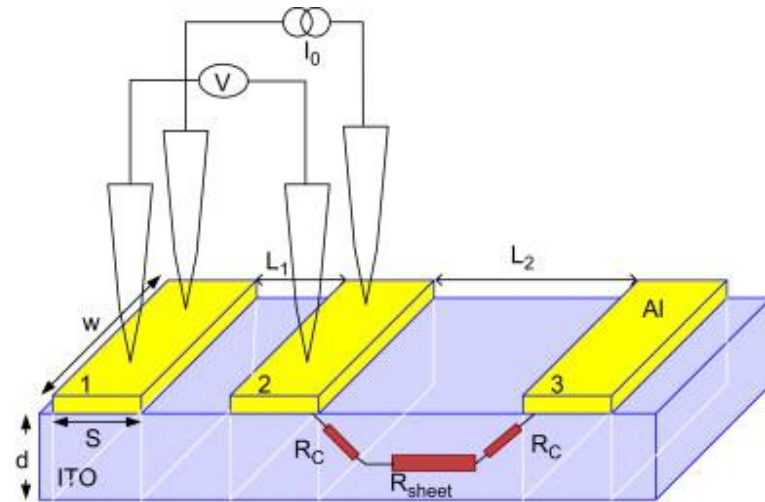


Figure 5.3: Schematics of the four-probe TLM [59].

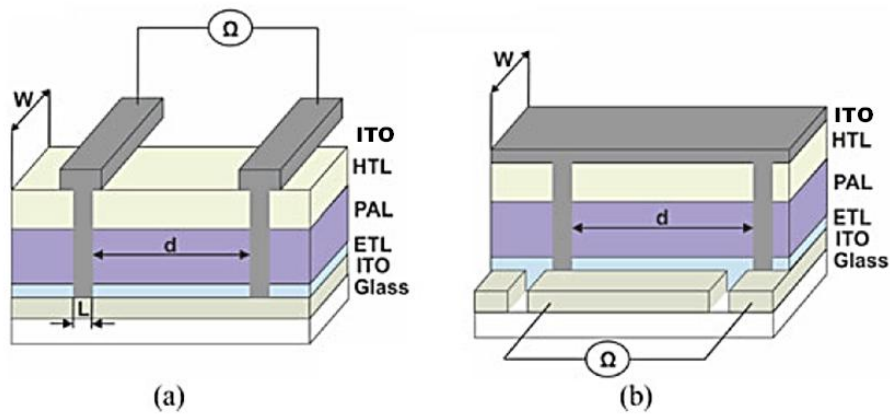


Figure 5.4: (Adapted) Setup of the TLM to a) Characterize the P2 contact resistance and the rear ITO sheet resistance. b) Determine the top ITO sheet resistance [58].

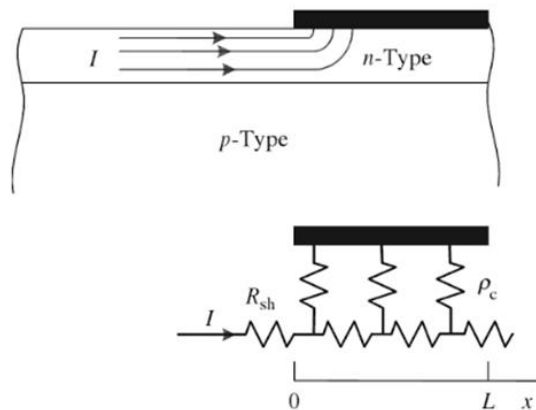


Figure 5.5: Current transfer from semiconductor to the electrode material [60].

The specific contact resistivity of the system ρ_c is determined for further loss analysis, this value is calculated as in Equation 5.6, where R_C is the contact resistance and A_C is the contact area, these properties are also depicted in Figure 5.3 [59]. A good value of this parameter is $\rho_c < 1 \times 10^{-6} \Omega m^2$

[60].

$$\rho_c = R_c A_c \quad (5.6)$$

The total contact resistance R_{TC} is obtained with the sum of contact resistance of both top and bottom electrodes, and the resistance in the front ITO electrode R_{ITO} between the P2 contact and the measurement probes (Equation 5.7). There is an additional consideration of the non-homogeneous current flow over the P2 contact as a result of the limited transfer length L_T , shown in equation 5.8 [58]. This length is known as the distance which most of the current is transferred from the semiconductor to the electrode or vice versa [60].

$$R_{TC} = \frac{\sqrt{\rho_c R_{SH}}}{W} \coth L \sqrt{\frac{R_{SH}}{\rho_c}} + R_{ITO} \quad (5.7)$$

$$L_T = \sqrt{\frac{\rho_c}{R_{SH}}} \quad (5.8)$$

Given the determination of the R_{SH} and R_{TC} and the variation of the contact length L it is possible to determine the specific contact resistivity ρ_c [58].

This method can be simplified by a graphic method with a plot of the measured total resistance R_T versus the contact length L . This graph can provide some parameters such as the contact resistance R_{TC} ; this is because the supposition of the zero-length resistor reaches its limit at $L = 0$. Therefore, the R_{TC} can be obtained with the extrapolation of the fit line, where this line crosses the R_T axis the found value is twice the total contact resistance (Figure 5.6).

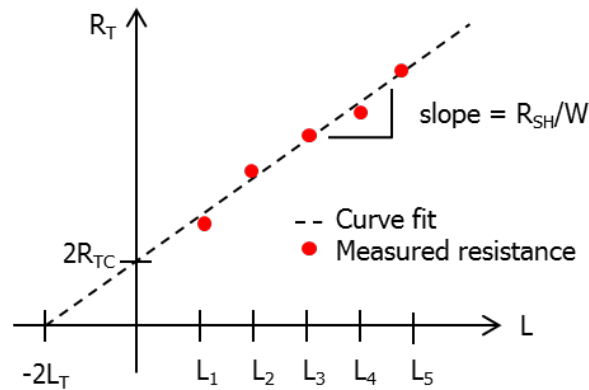


Figure 5.6: Fitted line of the Total resistance R_T vs. length L for the TLM measurements

The sheet resistance R_{SH} can also be determined by the slope of the line, calculated as R_{SH} / W . Besides, the transfer length can also be estimated by this regression. When the fit line is extrapolated until it touches the horizontal axis, the interception will have the value of $-2L_T$. In the calculation of the specific contact resistivity ρ_c , is important to mention that if L_T has a minimum magnitude, it would be substituted by the contact length L .

5.2.5. P3 SCRIBE LINE

The power scan is performed close to the values determined for P1 and P2 scribe. The wavelength, pulse length, and frequency are fixed again. Since an additional layer is going to be ablated (ITO), either higher apparent power or slower scribe speed is expected to give the best results.

Electronic and optical microscopy characterizes the ablated lines. The EDS mode is also employed for this test. This scribing process presents a photo mechanical ablation which causes the fracture and delamination of the ITO layer. This effect is caused by the low ablation threshold of

perovskite, spiro-OMeTAD and MoO_3 which causes the fast evaporation of material, this causes a mechanical stress which is liberated by the rupture of the ITO film. The GFF is compromised because of the width of delamination.

5.2.6. MODULE LASER SCRIBING

Once the optimal laser settings (wavelength, pulse length, frequency, apparent power, and scribe speed) are defined, they are programmed in the laser software. The *ADEM* system uses *Mathematica* to define the scribing lines position.

The Figure 5.7 shows the layout of the scribes required for the module: the device contains six cells and two contact area (left and right areas). Each size is 20×3.23 mm, making a total active area of 388.4 mm^2 . The markers on the top left, and down right sides are made to help the software to align the scribes on the next steps correctly. In this case, the P0 (wide scribe in gray) has the same settings as the P1 scribe.

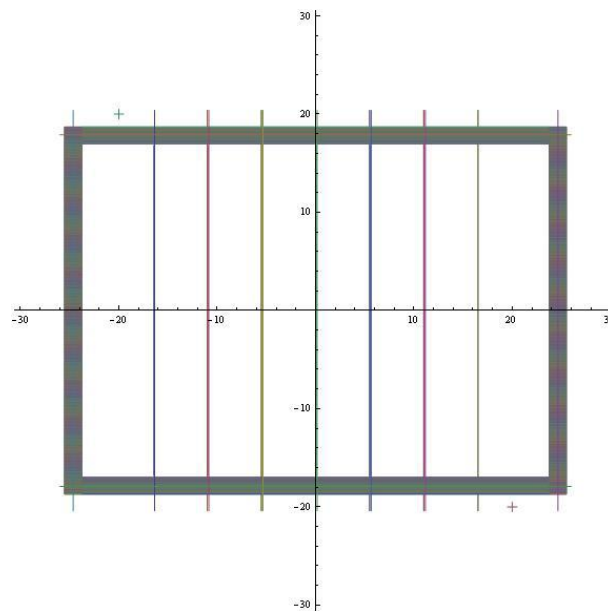


Figure 5.7: Layout of the laser scribes of the module (Schematics from *Mathematica* software), 1.7x upscaled

5.3. OVERVIEW OF THE MODULE PROCESSING

The Figure 5.8 shows a process diagram of the necessary steps to create a module (See also Sections 5.1 and 5.2). The module manufacturing can be divided into three phases according to the laser processing. First, the glass is cleaned to make suitable the ITO deposition by magnetron sputtering.

The first phase finishes with the P1 line scribing. The second phase begins with the cleaning of the glass substrate to remove the particles from the laser scribe. Then the SnO_2 and perovskite are deposited by spin coating with a posterior thermal post-treatment. Therefore, the spiro-OMeTAD is also processed by the solution-based method and exposed to dry air to form the layer. This phase finalizes with the MoO_3 deposition via a vapor-based method and the P2 line scribing.

The third and final phase starts with the ITO deposition via magnetron sputtering and the P3 line scribing, which finalizes the module processing.

5.4. CHARACTERIZATION OF THE SOLAR MODULE

For this project, the characterization consists in performance, quality material and interconnection of the cells evaluations. These methods are carried out by the IV-curve measurement; electronic

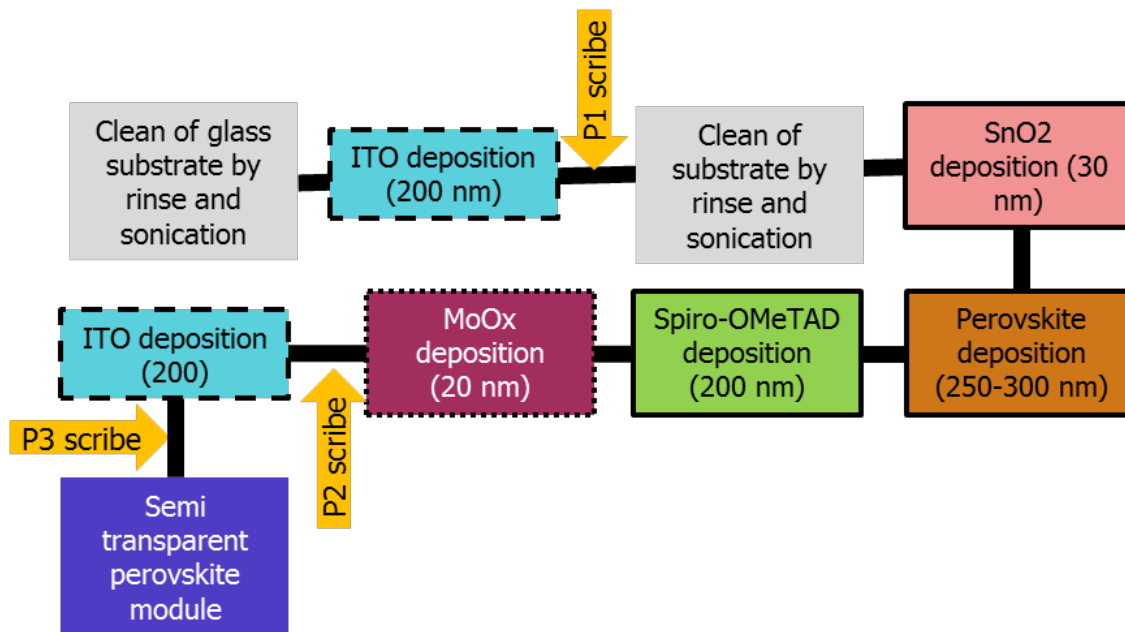


Figure 5.8: Overview of the perovskite module processing. The dashed outline are processed under RF magnetron sputtering, the dotted outline stands for vapor deposition, and the continuous line is deposition by spin coating.

and optical-microscopy; and photoluminescence and lock-in thermography, respectively.

The IV-curves are retrieved with a *Wacom Solar Simulator* which used to be AAA solar simulator at 10 x 10 cm. However, over the time the uniformity is no longer class A in this area. A silver paste is added to the contacts to enhance the conductivity with the probes of the system to improve the measuring. The silver paste is a *RS Pro Silver Paint Conductive Adhesive* manufactured by RS. The measurement is made in forward and reverse scan, which gives information of hysteresis of the module. A post-light soaking is also performed to analyze the behavior of the device after illuminated conditions.

The microscopy is employed in additional samples to evaluate the layer deposition and quality of the laser scribes, these factors are determinant to evaluate the layer deposition and the laser scribe quality. The confocal microscopy can provide a cross-sectional profile of the ablation and give an approximate depth of the line. With the approximate thickness of each layer, it can be approximated if the desired layers were removed. Furthermore, the electronic microscopy (SEM) also provides the elemental analysis through its EDS mode, this is critical for the laser scribe evaluation, since this mapping shows the presence of remaining elements in the ablation profile.

The interconnection is evaluated via photoluminescence and lock-in thermography. In photoluminescence, the sample is exposed to a green LED that excites the active area and takes a photo with a special filter that shows the stimulated areas. With this technique, the interconnection area would appear as a dark region of the device since it is not photovoltaic active. Additionally, this method can approximate the quality of the cells, and if the cells are producing current uniformly. That is because the activated areas should shine with the same intensity and the inactive spots should show some shunt effect. For this test the *Greateyes System LumiSolarCell* was employed.

For the thermography, the sample is tested in two modes: light activated and in the dark. During the first mode, the sample is excited with a green LED light lamp. In this case, the shunting areas should show a high temperature due to the resistance of the material to conduct. Regarding the interconnection, this area appears heated if the interconnection is not optimal. In the dark mode, the interconnection can be better evaluated, since the cell experiments an external current which also elevates the temperature of the sample. For this test, the *Thermography Camera ImageIR®* was

employed.

6

RESULTS AND DISCUSSION

This chapter reports the findings of the experimental work of this project. The sections are divided to show the establishment of the laser system, the setting up of each scribing line, and the eventual manufacturing of the module.

6.1. SET UP OF THE ADEM LASER SYSTEM

The first step is to analyze the process parameters of the *ADEM System* and their effect on the characteristics of the laser beam

As it was discussed in section 4.1.3, the most suitable wavelength for the stack is the UV due to the optoelectronic characteristics of the stack materials. Given that, the system was set on 335 nm wavelength. The influence of the frequency and pulse length on the pulse energy is analyzed with a power scan. The complete results are listed on Appendix A.

The Table 6.1 shows that the pulse energy reaches a maximum at 20 kHz for most of the cases. However, it required more source energy, 256.5 mW to perform the ablation process compared to 10 kHz with 58.9 mW. The maximum pulse energy was $20.15 \mu J/pulse$ with 144.4 mW at 20 kHz.

Respect to the pulse length it showed an inverse proportion to the pulse energy, where the weakest pulses were measured at 10 ps and the highest at 250 fs. Nonetheless, the femtosecond range delivers too high results for the ITO ablation.

Table 6.1: Maximum pulse energy in $\mu J/pulse$ for each pulse length and frequency

Frequency [kHz]	250 fs	1 ps	5 ps	10 ps
10	15.4	6.3	1.3	0.5
20	20.15	5.23	0.79	0.34
50	16.32	4.98	0.54	0.18

From the retrieved information it can be concluded that the pulse energy decreases with the increase of the pulse length, obtaining the highest value for 250 fs and the lowest at 10 ps.

Regarding the frequency, it is inversely proportional to the generated pulse energy of the system.

The Table 6.1 shows the highest pulse energy values for each pulse length and frequency. According to previous experiments at Solliance with a different system with similar wavelength, a pulse energy of $6 \mu J/pulse$ is required to ablate the ITO and form the scribing lines (Subsection 5.2.1). In light of this, the pulse length is set up to 1 ps at a 10 kHz frequency.

The diameter of the focal plane and ablation threshold were determined by a graphic method depicted in Subsection 5.2.2. In this method the power of the laser is varied to obtain different ablated diameters.

The Figure 6.1 shows the (a) D^2 of the average ablated spot at different apparent power, in μm^2 versus the pulse energy, in J . In this case, a trend line with logarithmic regression is employed to make the calculation. According to the method, the slope is used to determine the diameter of a beam in the focal plane $2\omega_0$, which is related to the fluence when assuming Gaussian beam profile. (b) Presents a dispersion of the D^2 of the average ablated spot for different apparent power, in μm^2 versus the fluence, in J/cm^2 with a logarithmic scale. In this case, the ablation threshold can be determined by the slope and intercept of the trend equation (Subsection 5.2.2).

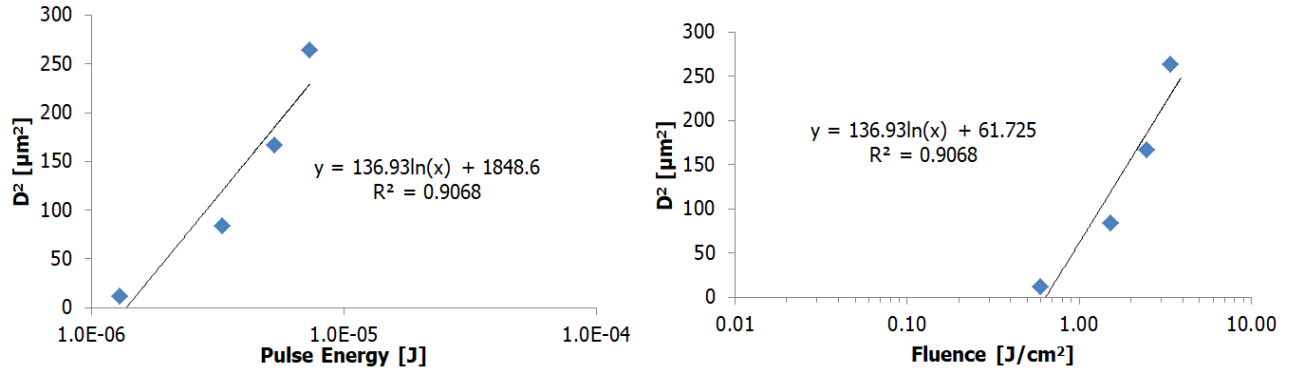


Figure 6.1: (left) D^2 of ablated spot (in μm^2) vs pulse energy (in J) for the determination of the diameter of beam in focal plane $2\omega_0$; (right) D^2 of ablated spot (in μm^2) vs fluence in logarithmic scale (in J/cm^2) for the calculation of the ablation threshold F_{th} home sputtered ITO.

The Figure 6.2 shows the plot for the calculation of $2\omega_0$ and the fluence. The results present that the commercial ITO film has a higher ablation threshold. This is directly reflected with the improved transparency of this material, which propitiates a more energy consuming ablation process compared to the home sputtered film.

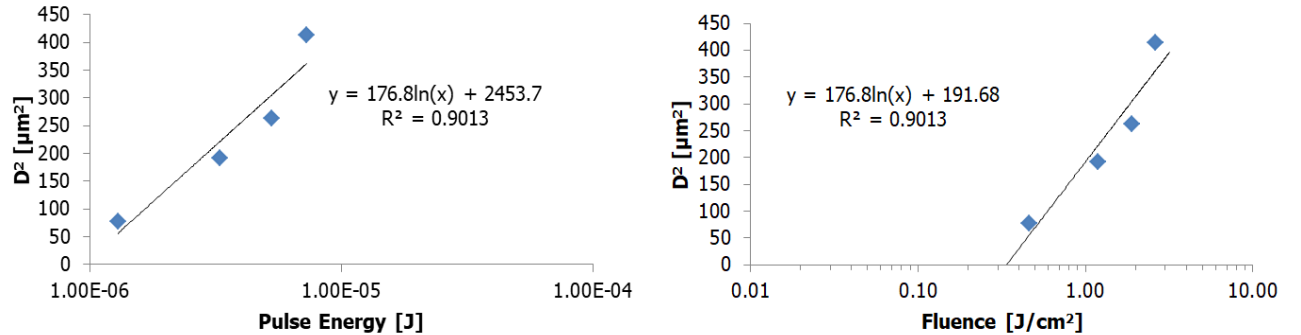


Figure 6.2: (left) D^2 of ablated spot (in μm^2) vs pulse energy in logarithmic scale (in J) for the determination of the diameter of beam in focal plane $2\omega_0$; (right) D^2 of ablated spot (in μm^2) vs fluence in logarithmic scale (in J/cm^2) for the calculation of the ablation threshold F_{th} commercial ITO.

The radius and diameter of the laser beam in the focal plane ω_0 and D_f , area of the spot in the focal plane A , and fluence threshold F_{th} are listed in Table 6.2. Additionally, the complete set of graphs and calculations are in Appendix A.

With this essay, the closest setting to the $6\ \mu\text{J}/\text{pulse}$ from previous works is a UV laser with 58.9 mW power with 1 ps pulse length at 10 kHz. The next values to determine per each scribe are the power and scribing speed.

Table 6.2: Threshold parameters for ITO samples ablated with UV laser at 10 kHz frequency 1 ps pulse length, and 7.6 to 58.9 mW power

Parameter	Commercial ITO	Home sputtered ITO
ω_0 [μm]	8.27	9.40
D_f [μm]	16.54	18.80
A [cm^2]	2.15×10^{-6}	2.77×10^{-6}
F_{th} [J/cm^2]	0.6371	0.3381

6.2. P1 SCRIBE LINE

A preliminary power scan is performed to find the most suitable scribe speed and power for the P1 line. This test is based on the estimation of the $16.5 \mu\text{m}$ spot size for the commercial ITO and $19 \mu\text{m}$ spot size for the home-sputtered ITO.

The distance between the ablated center of two dots is calculated with the Equation 5.2, this distance is also used to calculate the overlap between ablated spots.

The example below shows a simple calculation of the percentage of overlap for the home sputtered ITO. In this case, the distance between spot sizes is $16 \mu\text{m}$, which represents the 84 % of the spot size, and thus, a 16 % overlap (Figure 6.3).

$$16 \times 10^{-6} \text{m} \times 10 \times 10^3 \text{Hz} \frac{1000 \text{mm}}{1 \text{m}} = 160 \text{mm/s}$$

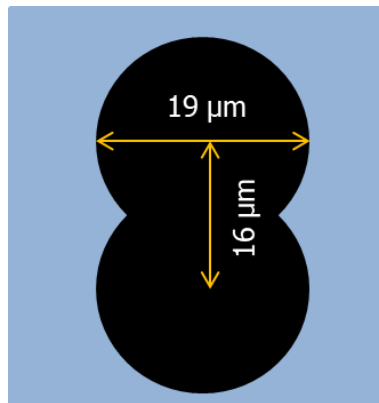


Figure 6.3: Schematic view of the spots overlap, where the $19 \mu\text{m}$ refer to the spot size, and the $16 \mu\text{m}$ show the spot distance. This example shows a 16 % overlap.

The first power scan was performed between 20 % and 95 % overlap and power from 7.6 to 58.9mW in steps of 17.1 mW (Appendix B). A simple check-up with a multimeter was performed to determine whether the line was conducting or not and check the presence of conducting material on the scribe.

The microscopy gave information for a qualitative evaluation of the scribed lines, such as front view and cross-sectional profile images. Some of the images of the P1 scribe show modification of the ITO next to the laser track helped to identify undesired phenomena such as annealing effect (Figure 6.4), especially in the amorphous sputtered-ITO.

Because of the focus issue of the laser beam a non-uniform pulse can be appreciated in this image, where the right side of the scribe shows ablation and the left side only modification of the material. This can be explained with an irregular distribution of the fluence (Figure 6.5) which shows more power at one side of the beam.

The Tables 6.3 and 6.4 show the results of the multimeter test for the scribed lines. The conductive lines are marked in gray, which mean not correct ablation of the material, while the white blanks refer to the isolating lines. This approach helped to narrow the power and scribing speed

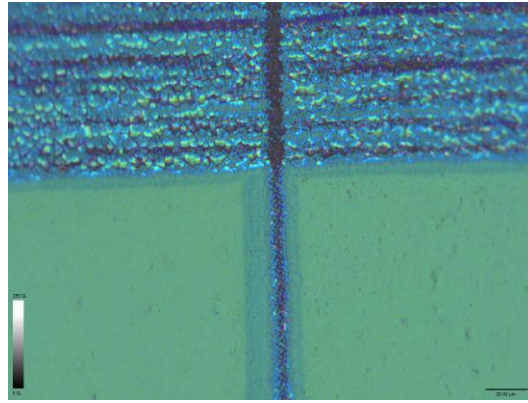


Figure 6.4: Crystallization effect on amorphous ITO, 50x magnification using confocal microscopy in white light mode.

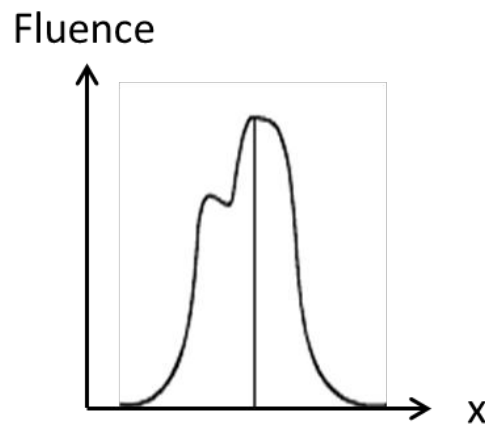


Figure 6.5: Crystallization effect on amorphous ITO, 50x magnification using confocal microscopy in white light mode.

range for a consequent power scan with more accuracy.

Table 6.3: Conduction test of the power scan for the commercial ITO

Power/speed	160 mm/s	120 mm/s	80 mm/s	40 mm/s	10 mm/s
7.6 mW	Conductive	Conductive	Conductive	Conductive	Conductive
24.7 mW	Conductive	Conductive	Conductive	Conductive	Conductive
41.8 mW	Conductive	Conductive	Conductive	Isolation	Isolation
58.9 mW	Conductive	Conductive	Isolation	Isolation	Isolation

Table 6.4: Conduction test of the power scan for the home sputtered ITO

Power/speed	160 mm/s	120 mm/s	80 mm/s	40 mm/s	10 mm/s
7.6 mW	Conductive	Conductive	Conductive	Conductive	Conductive
24.7 mW	Conductive	Conductive	Conductive	Isolation	Isolation
41.8 mW	Conductive	Conductive	Conductive	Isolation	Isolation
58.9 mW	Conductive	Conductive	Isolation	Isolation	Isolation

Given the big power and overlap steps of the prior power scan, a second power scan was performed with narrower ranges for scribe speed and power. In one hand, the commercial samples of ITO, the range was defined between 60 and 90 % overlap, and 35 to 45.2 mW. On the other hand, the home sputtered ITO required less energy to make a proper ablation, with a range between 17.9 and

28.1 mW. That is because the higher ablation threshold ITO of the commercial sample that requires more energy to melt and evaporate than the home-sputtered layer with a lower threshold.

The prior described isolation and qualitative tests were also carried out for this experiment. The complete images of confocal microscopy of the power scan can be found on the Appendix B. The Figure 6.6 shows the influence of the power inflicted to the amorphous ITO layer. For a lower power (a) the scribe presents melted material on the edges of the scribe which can cause shunts. While for higher power (c) the adjacent material experiences high thermal stress and forms cracks next to the edges of the scribe, these malformations can be responsible for delamination of the layer that leads to the reduction of the photoactive area. Therefore, the selected settings for the P1 scribe are 24.7 mW power at 30 mm/s for the home-sputtered ITO. Under these conditions, the average width of the scribe is 12.2 μm according to the SEM.

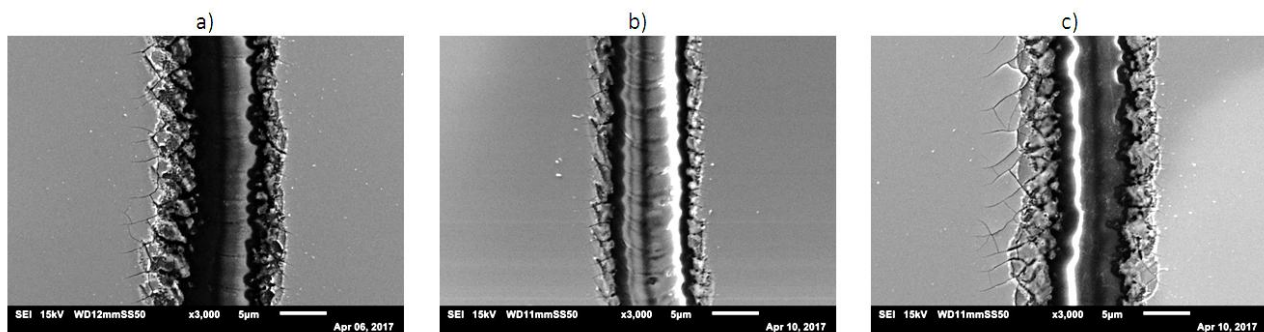


Figure 6.6: Power effect for the scribes on home-sputtered ITO for fixed 30 mm/s scribe speed and power of: (a) 1400 mW (21.3 mW real power), (b) 1500 mW (24.7 mW real power), and (c) 1600 mW (28.1 mW real power), 3000x magnification using SEM under scanner mode.

For the commercial ITO samples, the same power scan was performed. The complete set of experiments can be found in the Appendix B. The Figure 6.7 shows an example of the effect of the scribing speed at a fixed power. The slower scribe speeds deliver continuous lines (a), the faster speeds give isolated spots (c). Nonetheless, there is a trade off between the thickness scribe and scribing speed, if the scribing speed is slow, the thickness of the scribe tends to be thicker, and thus, reduce the GFF. After the analysis, the selected settings for the commercial ITO substrate were 35 mW and 80 % overlap (40 mm/s scribe speed). The white line of the figures (a) and (b) is charged glass due to the electron collision of the SEM microscope.

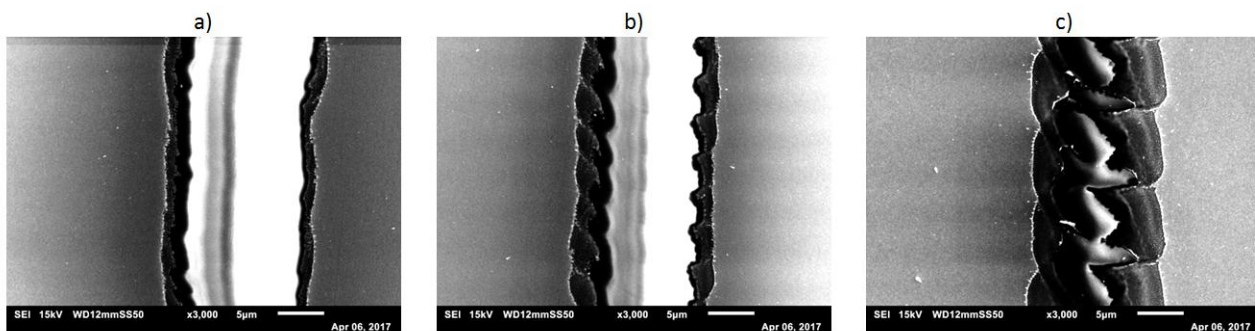


Figure 6.7: Scribe speed effect for the scribes on home-sputtered ITO for fixed 1800 mW apparent power (35 mW real power) and scribe speed of: (a) 20 mm/s , (b) 40 mm/s , and (c) 80 mm/s , 3000x magnification using SEM under scanner mode.

6.3. P2 SCRIBE LINE

The critical scribe line of this project is the P2 scribe since it determines the quality of the interconnection of the cells. The power scan starts with large power steps beginning with values of 11, 24.7, and 35 mW for the power, and overlap from 60 to 90 %. The Appendix B displays the complete set of results for the power scan. The Figure 6.8 shows the influence of the power of the beam on the laser scribe with different power. The confocal microscope gives an image with the actual colors of the sample, in this case, the dark purple of the center line is the bottom ITO, which should be completely free from other materials to form the contact with the subsequently deposited electrode layer. For a power of 11 mW (a) a non-continuous profile is present, this reduces the quality of the interconnection because of bridging material that increases the contact resistance. As long as the power increases, the damage to the bottom electrode layer increases, as it can be seen in (b). On the highest tested power, 35 mW (c), the laser surpasses the electrode to leave the glass substrate exposed, and this situation can lead to extra isolation of the cells.

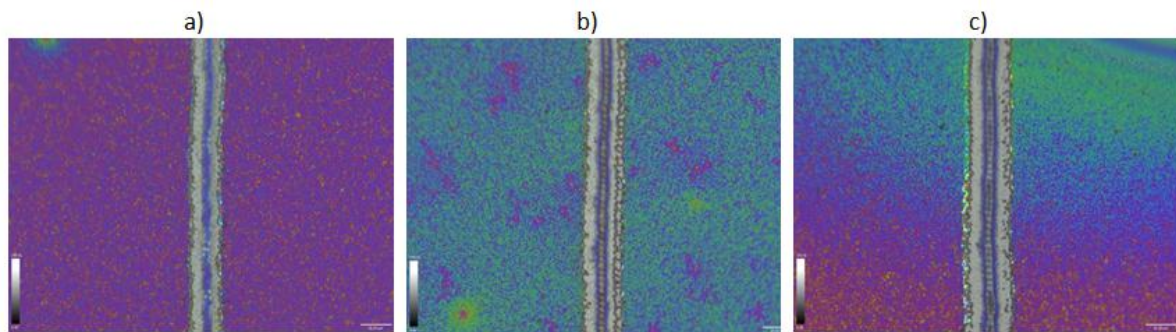


Figure 6.8: Apparent power effect for the P2 scribed lines on a stack with commercial ITO as bottom electrode for fixed 34 mm/s scribe speed and apparent power of: (a) 1100 mW (11 mW real power), (b) 1500 mW (24.7 mW real power), and (c) 1800 mW (35 mW real power), 50x magnification using confocal microscopy in white light mode.

The confocal microscopy can also provide a profile in a cross-sectional view. Since the approximate thicknesses of the layers are known, it can also determine whether the scribe reached the required depth. The Figure 6.9 gives the profile of two ablated lines at different scribing speed. At 80 mm/s (a) (60 % overlap) the estimated width of the scribe is 20 μm and a depth of 250 nm, which represents the removal of MoO₃ and spiro-OMeTAD. Additionally, the profile shows a rather squared shape, which is preferred for the P2 scribe since it will form the channel for the current flow.

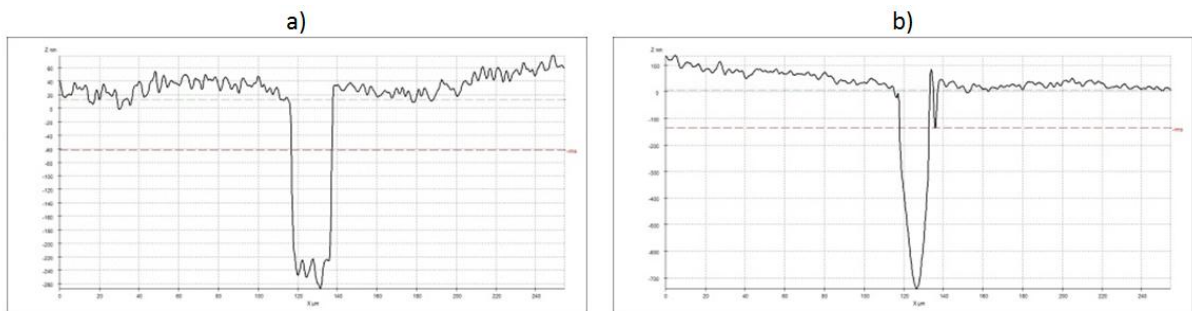


Figure 6.9: Cross sectional profiles of the P2 scribes at a fixed apparent power of 1100 mW (11 mW real power) and overlap of 60 % (a), and 90 % (b), 80 and 20 mm/s, respectively. Obtained with confocal microscopy in topography mode.

On the other side, the 20 mm/s scribing speed (b) (90 % overlap) has a narrower width of 15 μm . This setting reaches a depth of 750 nm. Regarding the profile outline, this scribe shows a triangular shape, with a minimum width of 5 μm on the bottom of the valley, this would mean a dramatically

decreased contact area, which can reduce the current flow.

Considering the thicknesses of the layers as 30 nm for SnO_2 , 480 nm for the perovskite layer, 200 nm for spiro-OMeTAD, and 20 nm for MoO_3 . Resulting scribing depths close to the 730 nm will be selected for further analysis in the SEM.

The SEM method can determine the removal of desired material thanks to its elementary analysis available on the EDS mode. The Figure 6.10 shows the front view in 3000x magnification, and In and Pb element mapping for three different cases: (a) was scribed with 11 mW at 40 mm/s. This case presents a narrow scribe and a relatively extensive affected area (lighter gray color at the sides of the line) the elemental analysis shows an absence of carbon C in the affected region. This would infer a damage to the C-content perovskite and spiro-OMeTAD layers. However, the Pb contour shows the presence of this element in the damaged area. Therefore, only the HTL is additionally affected during the P2 scribe. In the case of the bottom electrode layer (left side), it shows no damage on its surface and then can form a good contact.

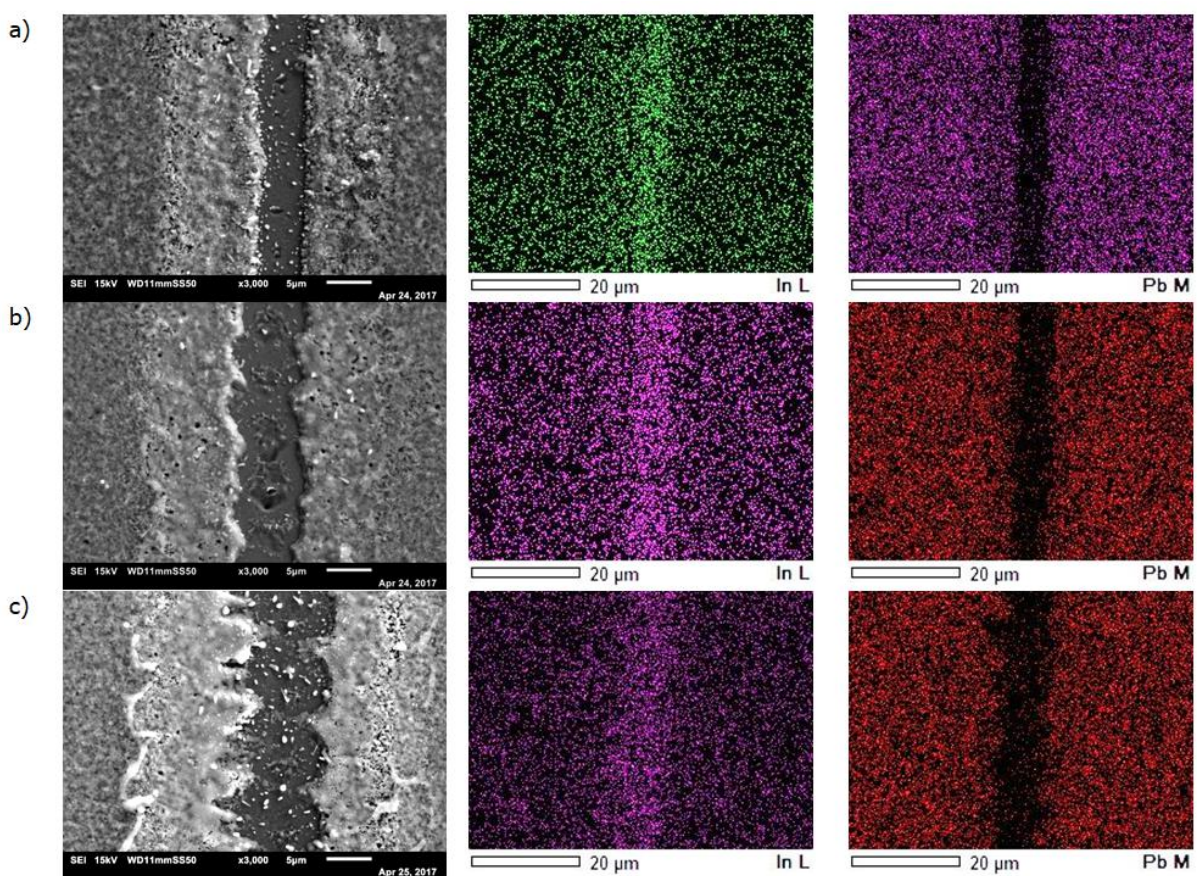


Figure 6.10: Comparison of diverse samples for the first P2 power scan with different power and scribe speed: (a) 1100 mW apparent power (11 mW real power) at 40 mm/s; 1500 mW apparent power (24.7 mW real power) at 60 mm/s; and (c) 1800 mW apparent power (35 mW real power) at 80 mm/s, 3000x magnification using SEM under scanner mode (left), and EDS mode (center, right).

The image (b) shows a scribe performed with 24.7 mW at 40 mm/s; this case showed a similar profile in comparison with the first picture, except for the broader valley in this case. Furthermore, the ITO layer shows some damage at the center of the scribe, which could reduce the quality of the electrode contact by the increase of R_{TC} , this effect requires further research. Lastly, for 1800 mW at 80 mm/s (c) the line shows an irregular continuity with a broader damage to the spiro-OMeTAD, this is because high scribing speed gives rather patterned than a uniform line, also seen in Figure 6.7

(c). However, the scribe presents a wider valley because of the higher power employed.

To conclude, this experiment shows the influence of the power and scribing speed: the higher power forms larger scribed lines with potential damage to bottom layers, such as the electrode, it also damages the edges of some materials such as the HTL. Regarding the speed, slower scribing leads to continuous and wider lines, but it can also have the same damaging effect as the high power. The complete power scan can be found on the Appendix C. Given this, the power for the next test will be no higher than 24.7 mW

A fine tuning power scan was performed between 14.4 and 21.3 mW and overlap from 65 to 85 %. This test shows satisfying results between 17.9 and 21.3 mW with an overlap between 75 and 80 %. The Figure 6.11 shows the microscopy analysis of one of the best-scribed lines, the settings of this sample were a power of 17.9 mW and scribing speed of 40 *mm/s*, which corresponds to an 80 % overlap. (a) shows the image obtained with optical microscopy, the ablated line shows a continuous profile with no damage to the bottom electrode (the dark blue area at the center), nonetheless, it shows gray areas on the sites of the scribe which will be analyzed by electronic microscopy. (b) shows the cross sectional profile of the scribed line, this has a depth of 700 nm and approximate width of 25 μm near the surface and 5 μm on the deepest region, which gives an estimation of the correct ablation of material. (c) Shows the image captured with electronic microscopy (SEM) under 2000x magnification, there is narrower damage to the edges of the scribe compared to other settings (Appendix C) and the bottom ITO layer also has minor damage.

The evaluation continues with the elementary analysis under the EDS mode of the microscope. Regarding the bright gray area, the image (d) shows an absence of C in this area, which may suggest a damage caused to the spiro-OMeTAD layer, this is confirmed by the presence of Pb in the same region (f). The intense presence of In in the center of the image (e) and the absence of Pb in the same region of (f) show a proper ablation of the layers.

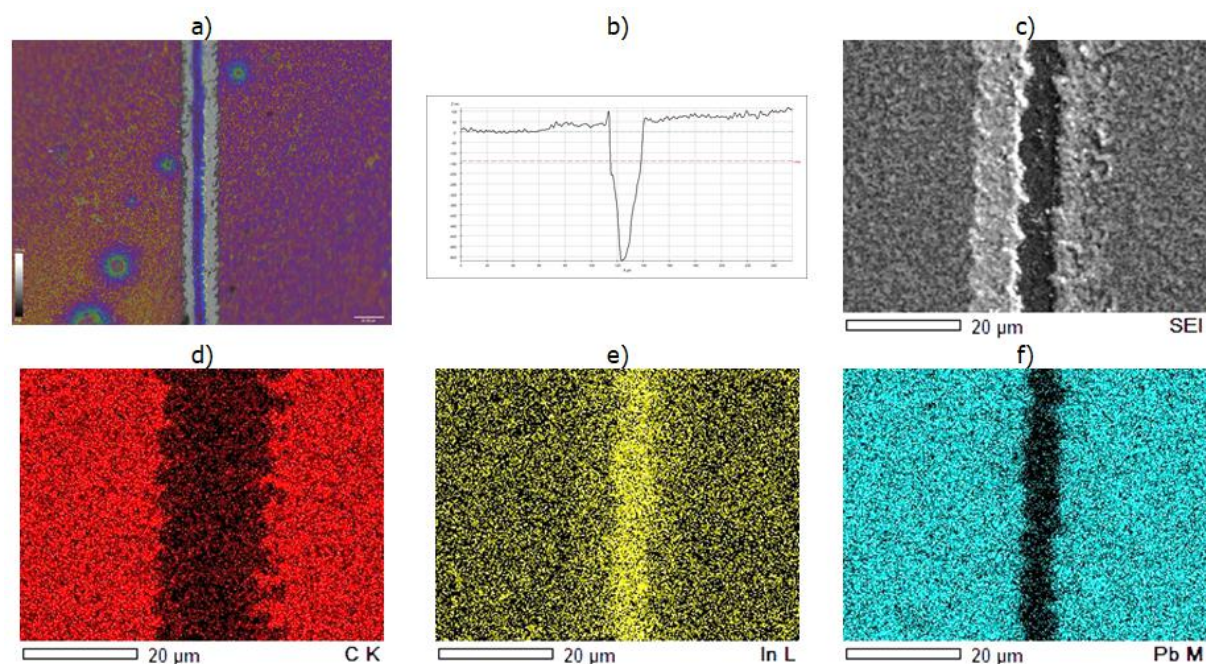


Figure 6.11: Microscopy analysis for the most suitable settings for the P2 Scribe. The scribe was done with an apparent power of 1300 mW (17.9 mW real power) at 40 *mm/s* (80 % overlap). (a) 50x magnification using confocal microscopy in white light mode; (b) cross sectional profile using confocal microscope under topography mode; (c) 2000x magnification using SEM under scanner mode; 2000x magnification using SEM under EDS mode to detect C (d), In (e), and Pb (f).

The microscopy analysis suggests a laser configuration of 17.9 mW power at a scribing speed between 50 and 60 *mm/s* (70 and 60 % overlap, respectively). This scribe quality has relatively low

reproducibility during this project because of the batch-processed laser scribes and the narrow optic field. The next subsection presents the results from the TLM measurements to select the most suitable settings for the P2 scribe.

6.3.1. TLM MEASUREMENTS

The contact resistivity ρ_c was determined for two type of contacts: TCO-TCO, and metal-TCO, the scribes were made with three different power and two different scribing speed. In this test the gold top electrode was compared with ITO to make a reference with the material that has also been tested recently at another partner of Solliance [58].

The Figure 6.12 shows the measured total resistance R_T in terms of the measured distances for a scribed interconnection in a ITO-ITO contact. This line was scribed with 17.9 mW (1300 mW apparent power) at 60 mm/s. The average contact resistivity ρ_c was $1.20 \times 10^{-3} \Omega \text{cm}^2$ for ITO-ITO contact, and $2.81 \times 10^{-4} \Omega \text{cm}^2$ for the Au-ITO contact presented. More research needs to be done to find the causes. The complete results are available in Appendix D.

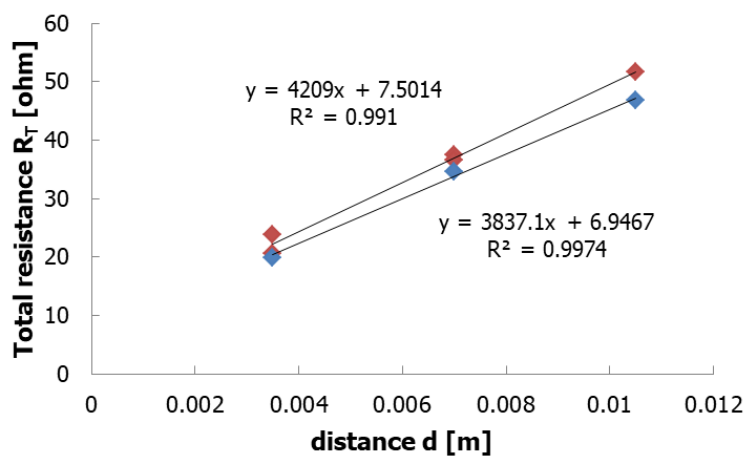


Figure 6.12: Total resistance R_T (in Ω) versus distance d (in m) for an interconnection scribed with an apparent power of 1300 mW at 60 mm/s scribe speed.

The Figure 6.13 shows a chart with the results of the TLM for the ITO-ITO and Au-ITO connection.

For the ITO-ITO connection the contact resistivity is directly proportional to the power used in the scribe. This is coherent with the qualitative analysis, where the high power inflicts damage to the electrode layer, and therefore, hinders the contact of the front and rear electrodes. Respect to the scribing speed, it does not show a clear relation with the ρ_c , this can also infer that this parameter is close to the optimal value. However, the scribing speed of 60 mm/s presented better results in the microscopy analysis.

For the Au-ITO connection the trend shows a slight decrease at 1250 mW apparent power (16.15 mW real power). This uncommon trend can be related with the small optical field of the laser system, which cannot deliver the same quality of line for the whole scribed batch. This was also explained with the non-uniform fluence distribution on Figure 6.5. Nevertheless, the most suitable setting seems to be with 16.15 mW power with no clear preferred scribing speed.

The comparison between the previous determination of ρ_c of this samples and the processed modules is required because of the laser scribe and film deposition variations. A TLM study is performed to some samples from the batch of the module processing.

From the qualitative and quantitative tests the selection of the P2 setup is set with 17.9 mW power at a scribing speed of 60 mm/s.

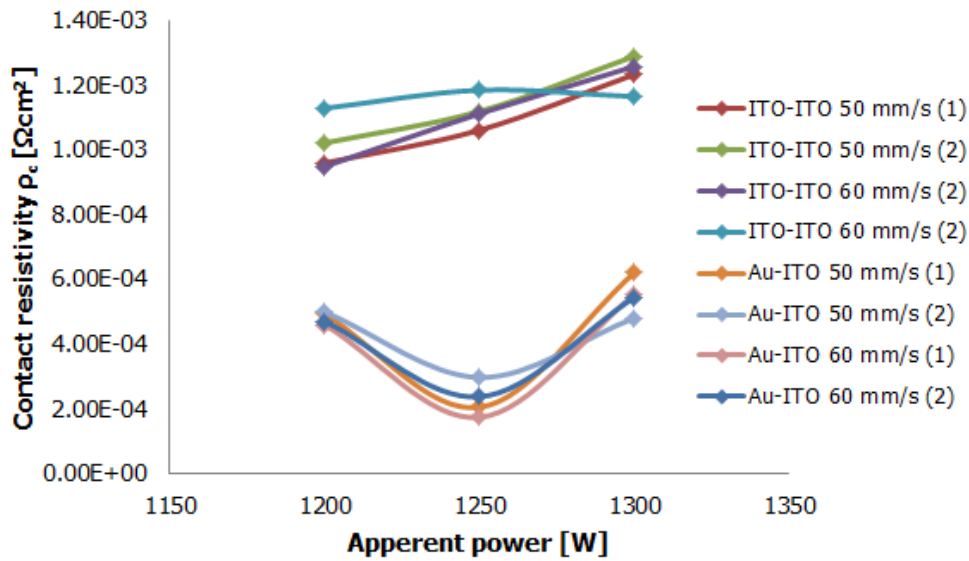


Figure 6.13: Contact resistivity ρ_c (in Ωcm^2 vs apparent power (in mW) for selected P2 scribe settings

6.4. P3 SCRIBE LINE

The power scan of the P3 scribed started with values close to the P2 selected settings. The power was considerably narrow compared to the previous tests, the tested powers were 14.4, 16.15, and 17.9 mW. Most of the selected power delivered good results at scribing speed of 40 mm/s .

The Figure 6.14 shows a comparison of scribing speed for a sample processed at 17.9 mW. An important delamination phenomenon occurs in all cases, and this is because the lower threshold of perovskite which causes a photo mechanical ablation effect with the front ITO electrode. This material has an amorphous structure, which is highly sensitive to thermal stress. In addition, the crystallization effect (Figure 6.4) also contributes to this issue. The damage of this layer is inversely proportional to the scribing speed, reflected in less chips. In this case, the 40 mm/s was the optimal rate for this scribe line. The complete set of results is displayed in Appendix E.

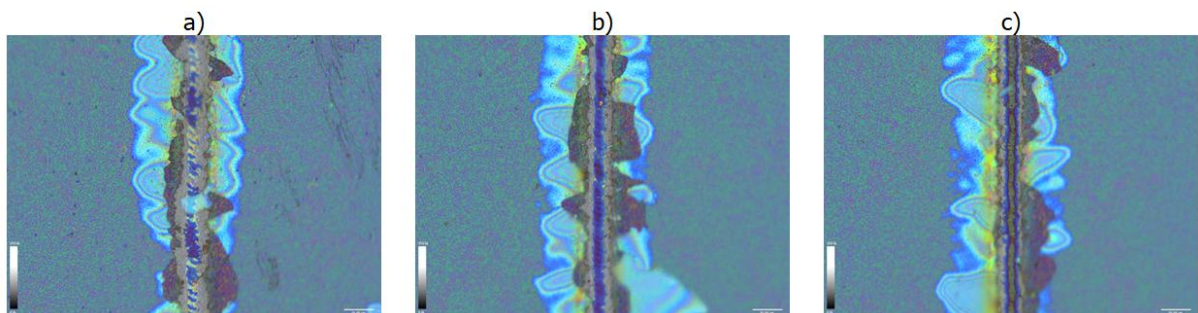


Figure 6.14: P3 scribes power scan with fixed apparent power of 1300 mW (17.9 mW real power) at scribing speed of (a) 50 mm/s , (b) 40 mm/s , (c) 30 mm/s , 50x magnification with confocal microscopy in white light mode.

Given the detachment of material on the sample, a topography study was performed. The confocal microscopy can capture 3D images to analyze the nature of the scribe.

The Figure 6.15 shows the results of this analysis. (a) Presents a 3D picture of the sample, it shows a wide area of damage to the front electrode, with some parts completely removed in the form of flakes, this is known as delamination. The image (b) is the front view of the 3D image, which shows the mentioned material in reddish colors. In (c) the cross sectional profile states that

the scribe has a depth of 900 nm which is coherent with the thicknesses of the layers to ablate, the width of this valley is relatively continuous, with a maximum $15\ \mu\text{m}$ distance. Furthermore, it shows the complete removal of material (right side of picture) and the presence of the flakes (left side of the scribe). This optical analysis cannot determine the affected layers, even though it is believed that only the ITO is affected.

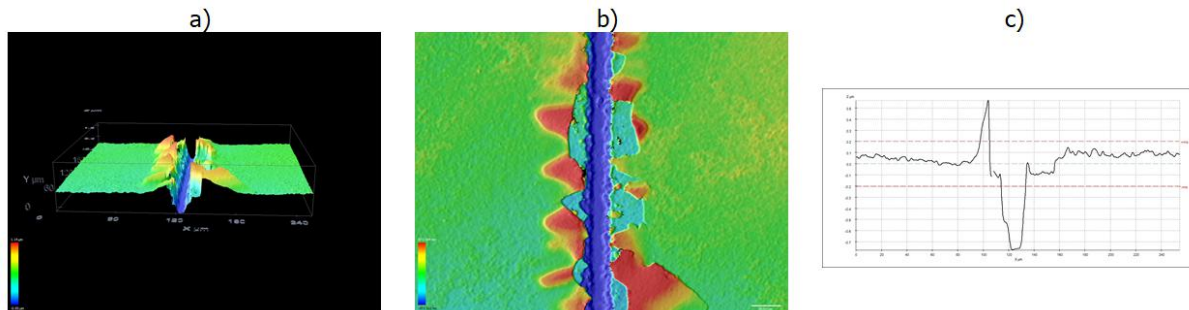


Figure 6.15: P3 scribed lines topography analysis for a sample ablated with apparent power of 1300 mW (17.9 mW real power) at scribing speed of $40\ \text{mm/s}$, (a) 3D surface image with confocal microscopy in confocal mode, (b) 50x magnification with confocal microscopy in contour mode, (c) cross sectional profile with confocal microscopy in topography mode.

The Figure 6.16 shows the elemental analysis performed to the sample to determine the films affected by delamination. (a) shows the frontal view of the sample under 2000X magnification. The left side of the image exposes a complete delamination of material, while the right side shows less detachment of the layer. (b) presents the profile of Pb, directly related to the perovskite layer. This material was only removed on the line region, which proves that the light absorbent layer was not affected by the laser beam. The In of the front ITO is absent of the delaminated areas (c). Nonetheless, the stronger signal of the right side appears to be a flake of material that is not attached to the stack. The figure (d) confirms this supposition since the C profile has a weaker signal in the same region. This element is related to the underneath layer of the electrode, spiro-OMeTAD. Besides, the layer is widely removed compared to the perovskite, proving the low resistance to thermal stress due to the film nano structure.

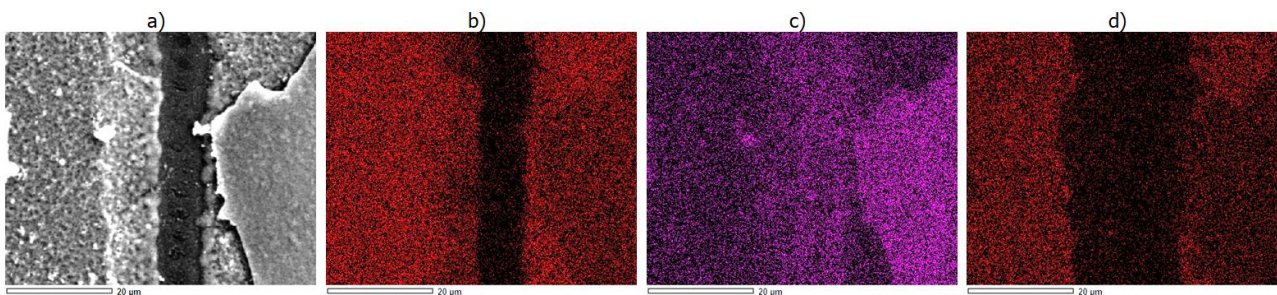


Figure 6.16: P3 scribed lines elemental analysis for a sample ablated with apparent power of 1300 mW (17.9 mW real power) at scribing speed of $40\ \text{mm/s}$, (a) 2000x magnification with SEM under scanner mode; 2000x magnification with SEM under EDS mode (b) Pb, (c) In, and (d) C mapping.

The final settings for this scribe are 17.9 mW power and $40\ \text{mm/s}$ scribing speed. At this rate, the electrode layer shows less damage compared to slower and faster speeds. Besides, the combination of power and speed removes the materials correctly and does not damage the rear ITO (Appendix E).

6.5. OVERVIEW OF THE LASER SYSTEM PARAMETERS

The Table 6.5 resumes the selected settings for each scribe. The speed is 40 *mm/s* for most of the cases, this represents an 80 % overlap. The power also has near values (except the commercial ITO). The incident real power to the samples are 34.96 and 24.7 mW for the P1 scribe (commercial and home sputtered, respectively), and 17.86 mW for P2 and P3 scribe. These numbers were calculated using the data of the Appendix A.

Table 6.5: Selected settings for each scribe line

Scribe line	Frequency [kHz]	Pulse length [ps]	Power [mW]	Scribing speed [mm/s]
P1 (commercial ITO)	10	1	1800	40
P1 (home made ITO)	10	1	1500	30
P2	10	1	1300	60
P3	10	1	1300	40

6.6. MODULE PROCESSING

The experiment used both commercial and home sputtered ITO samples as the bottom electrode layer. However, due to scribing issues, the batch with commercial samples was destroyed. The presented experiments are from the home sputtered ITO layer.

The P1 scribe was performed following the settings of Table 6.5 and the design depicted in Figure 5.7. After the laser processing, the isolation of the cells was checked with a multimeter to warranty the correct removal of conducting material.

The Figure 6.17 shows the results of the confocal microscopy analysis. The line appeared to be continuous and without damaging to the edges (a). The width of the scribe is 20 μm and depth of 200 nm with a good squared profile (b) and (c). No delamination and good edge quality without spikes were detected in the samples.

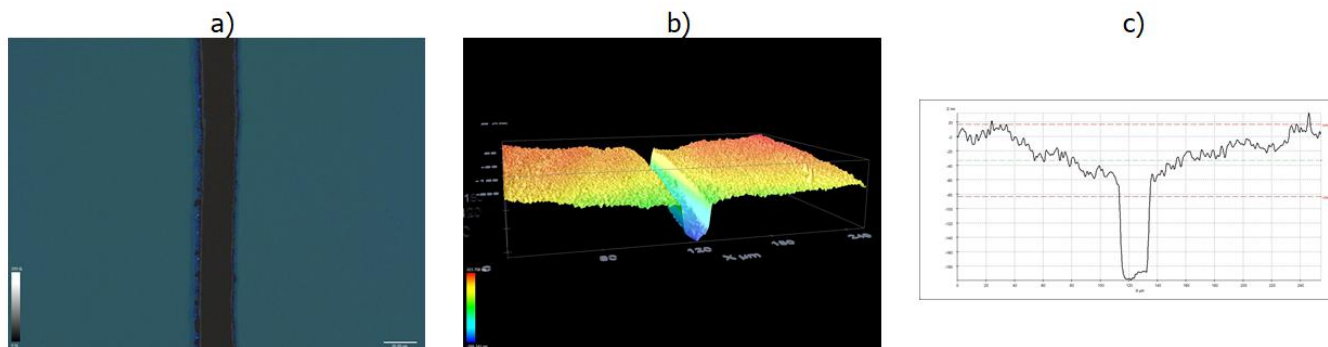


Figure 6.17: P1 scribing line analysis with microscopy. (a) 50x magnification with confocal microscopy in white light mode, (b) 3D surface image with confocal microscopy in topography mode, (c) cross sectional profile with confocal microscopy in topography mode.

The Figure 6.18 shows the necessity of cleaning post-treatment after P0 and P1 scribe (where P0 defines the area of the cell). After the first laser processing, a remarkable amount of particles is present on the substrate (a). This suspending material can compromise the quality of the consequent deposited layers. After the sonication, the sample has no pollutants on its surface (b).

The depositions were performed based on the method described in Chapter 5. The morphology of some layers is plotted in Figure 6.19. It can be seen that the SnO_2 forms large particles on its film, this can be related to the crystallization effect from the post-annealing treatment (a). For the triple

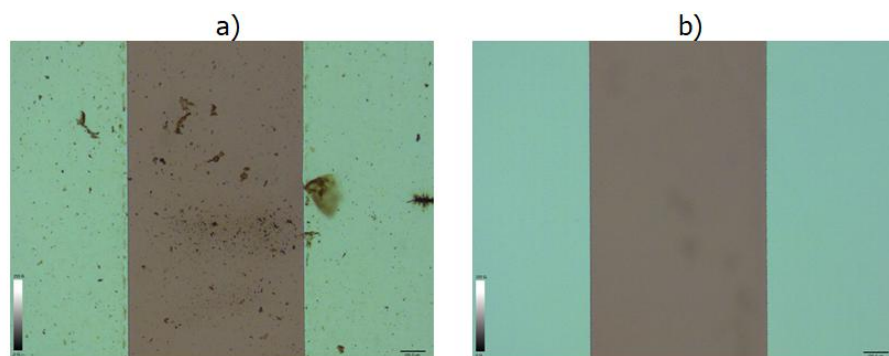


Figure 6.18: Effect of substrate clean after P0 and P1 scribing (a) substrate right after laser processing (b) substrate after sonication cleaning.

cation perovskite layer (b) the layer has good uniformity with a minimal presence of holes, which infers a high quality of the film. The spiro-OMeTAD shows a granulated structure with big grain size (c) with no presence of voids on its surface.

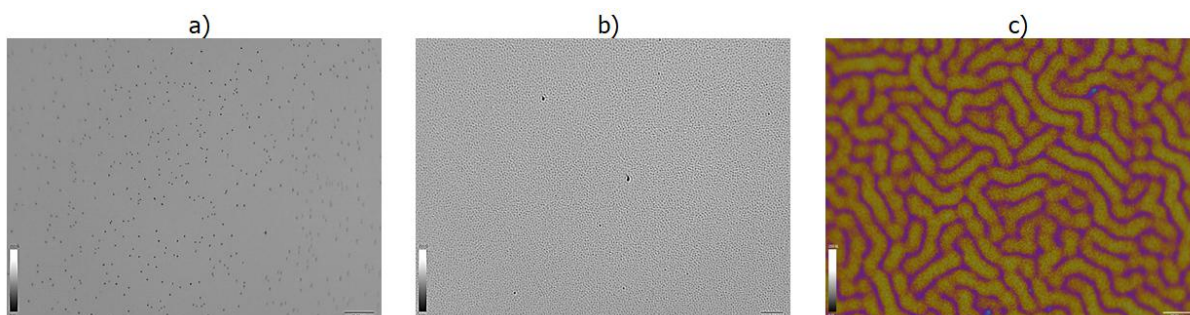


Figure 6.19: Morphology of different deposited layers. (a) SnO_2 , 50x magnification with confocal microscopy in blue light mode. (b) perovskite layer, 20x magnification with confocal microscopy in blue light mode. (c) spiro-OMeTAD, 50x magnification with confocal microscopy in white light mode.

The P2 line was scribed under the conditions stated in Table 6.5. The width of the scribe is around $40 \mu\text{m}$ near the surface in a continuous line with no significant damage to the edges. The bottom part of the scribe presented $10 \mu\text{m}$ broadness. The valley has a slight triangle shape with $750 \mu\text{m}$ average depth. However, this batch had a problem in the complete removal of SnO_2 , which will affect the performance of the cell.

This ablation issue is associated with the limitation of the field size of the *telecentric f-theta* lens used in this setup. Since the UV lens has a relatively small working area where the focus position is corrected as function of position in the field size ($35 \text{ mm} \times 35 \text{ mm}$). Close to the borders of this area the focus position is not defined anymore and a larger spot size is obtained on target.

A quick ablation check before the P2 lining step would be enough to avoid undesired effects. However, given the safety measures of the perovskite laser processing, the samples cannot be processed one by one, and thus are not available to check with the microscope right after the laser scribing.

Furthermore, the laser processing faced issues respect to the alignment of the P2 and P3 lines concerning the precedent scribed line. In some cases, the markers were difficult to find which derived in tilted lines that crossed the others. Another reason was the deviation of the *ADEM System*, which scribed the lines with different distance respect to the layout, this situation leads to overlap of lines or bad positioning. This misalignment is directly responsible for the considerable loss of samples.

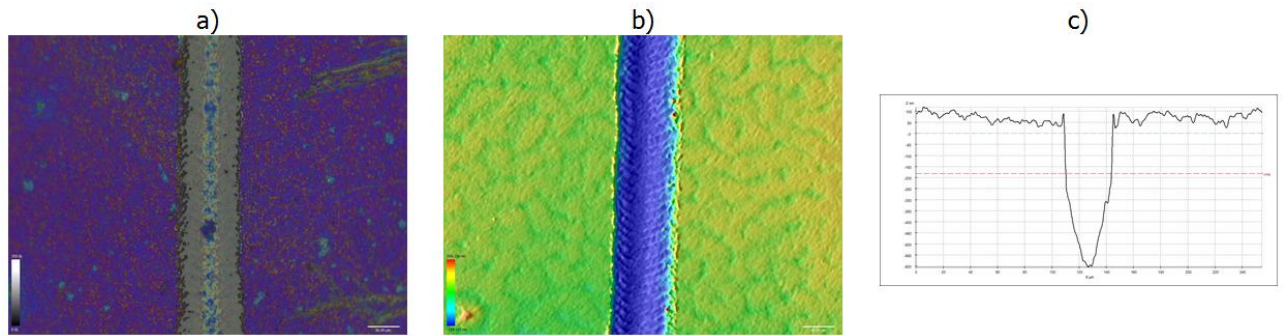


Figure 6.20: P1 scribing line analysis with microscopy. (a) 50x magnification with confocal microscopy in white light mode, (b) 3D surface in front view with confocal microscopy in topography mode, (c) cross sectional profile with confocal microscopy in topography mode.

The last scribe, P3 line, was performed with the operating conditions listed in Table 6.5. The microscopy analysis is presented in Figure 6.21. The front view of the cell (a) shows the delamination effect in the P3 scribe. This damage has an average width of $66 \mu\text{m}$ (including the scribe). This material damaging has no significant impact on the geometrical losses since one of its sides is inside the dead area. Thus the estimated width loss for each scribe is $20 \mu\text{m}$. The contour image of the scribed line (b) shows suspended material near the scribe and less delamination compared to previous tests. The average depth of this scribe is $900 \mu\text{m}$ with a squared profile of $20 \mu\text{m}$ wide (c), which is the desired shape for the line. The last two images also present the presence of the P2 scribe which was previously analyzed.

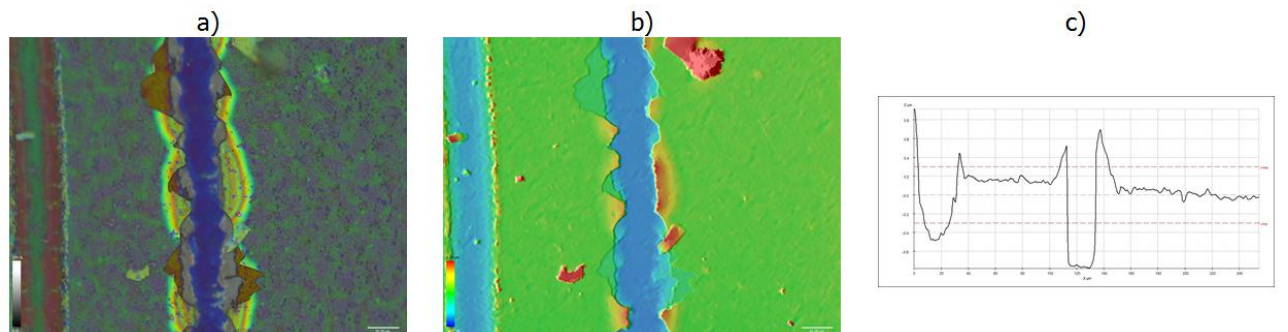


Figure 6.21: P1 scribing line analysis with microscopy. (a) 50x magnification with confocal microscopy in white light mode, (b) 3D surface in front view with confocal microscopy in topography mode, (c) cross sectional profile with confocal microscopy in topography mode.

Additional devices of the batch were prepared to perform TLM analysis and make it comparable with the modules of the same group of samples, which in turn, can be compared to the previous test. The average contact resistivity ρ_c was $2.29 \times 10^{-2} \Omega\text{cm}^2$. This value is almost ten times higher compared to the previous test. This high resistance was added by the SnO_2 material that was not correctly removed. The complete set of results can be found on Appendix ??

The Figure 6.22 shows the outline of the laser processing. The measured width of the scribed and damaged area is $240 \mu\text{m}$ (0.24 mm). Besides, this module layout the length of the ablated lines is 20 mm . Then, the dead area is around 4.8 mm^2 per interconnection, thus 24 mm^2 for the whole device. The total size of the module is $20 \times 19.41 \text{ mm}^2$, thus 388.2 mm^2 area. With all the previous data, the GFF is calculated as:

$$GFF = \frac{388.2 - 24 \text{ mm}^2}{388.2 \text{ mm}^2} = 93.81 \%$$

The selected module layout and laser setup have geometrical losses up to 6.19% , a low value

that can be reduced with the reduction of the distance between P2 and P3 (Figure 6.22

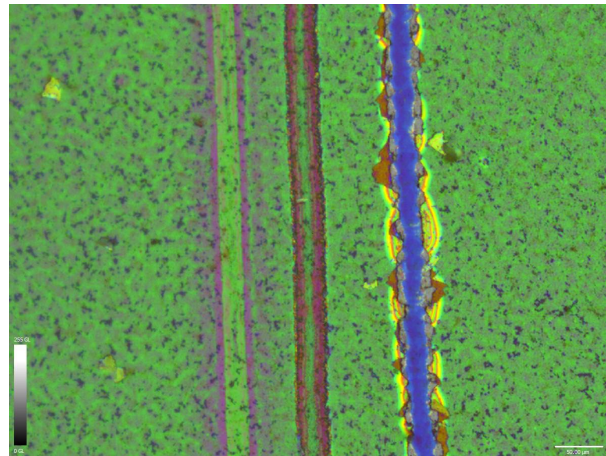


Figure 6.22: Outline of the scribe processing: P1 on the left, P2 at the center, P3 in the right, 20x magnification with confocal microscopy under white light mode.

The modules are ready for characterization. The working modules are referred as E4, E5, and E6. These modules have home sputtered ITO as both front and rear electrodes. Nonetheless, because of the relatively low conductivity of the ITO compared to metallic materials, metal stripes are added to the contact area. For this experiment, a Silver paste is employed.

6.6.1. REFERENCE CELL CHARACTERIZATION

Working single cells were prepared simultaneously with the module batch to make a comparison of the properties. The Figure 6.23 shows the IV curves of the reference cell (built simultaneously with the modules). The forward scan is made from the J_{SC} to forward bias; while the backward scan is performed from forward bias to the J_{SC} . The scan rate was set in the speed mode under 20 mV s^{-1} .

These values were calculated with a graphic method. The series resistance is calculated with a regression of the IV curve near the V_{OC} is plotted, the inverse of the slope its absolute value is the series resistance in $\Omega \text{ cm}^2$. The shunt resistance, on the other side, is obtained with the dispersion of the IV curve near the J_{SC} and the same posterior calculation.

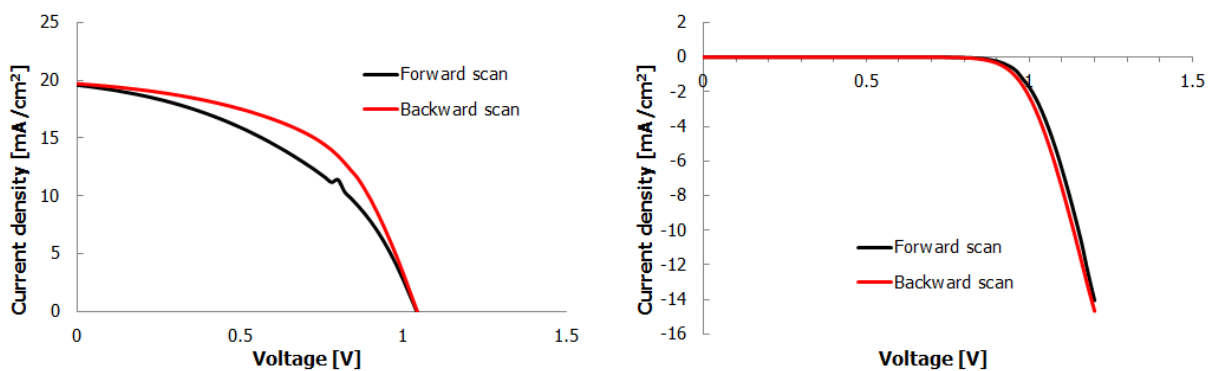


Figure 6.23: Current–voltage under illumination (left). (b) Current–voltage in the dark. Results of the best performed cell.

The Table 6.6 shows the results of the characterization of the IV-curve. The overall efficiency of the device is nearly 11 %. This value is delimited by the FF which surpasses 53 %. Shunt resistance and additional resistance are the two main reasons of the decreased FF. The decrease of the efficiency can be because of the quality of the solutions and consequent solution-based deposition of the layers.

Table 6.6: Reference cell characteristics under illumination in backward and forward scan

	Backward	Forward
V_{OC} [mV]	1042.78	1041.00
I_{SC}/cm^2 [mA/cm ²]	19.71	19.58
FF [%]	53.28	44.73
MP/cm ² [mW/cm ²]	10.95	9.12
Efficiency [%]	10.95	9.12

6.6.2. MODULE CHARACTERIZATION

The Figure 6.24 shows the measured current-voltage lines for the working devices. The Table 6.7 lists the complete characteristics of the working modules of the experiment

In most of the cases, the J_{SC} is around 3 mA/cm². This current is dramatically reduced compared to the reference cell, which is near 20 mA/cm² (Figure 6.23). Diverse factors can be behind this. Firstly, it is important to remember that since the module is constituted by series connected cells, in such an arrangement the overall current density is limited by the lowest of one of the cells. If one of the cells have processing defects, this cell will be more likely to reduce the current of the complete device. Secondly, the interconnection is critical regarding current flow. If the materials are not correctly removed, they can produce additional resistance to the current flow, an example of this is the SnO₂. This had origin on the defocus of the laser and the caused non-uniform fluence of the beam. Lastly, the quality of the material needs to be optimum at the time of the deposition, solutions as the spiro-OMeTAD and triple cation perovskite need to be prepared within two weeks before the deposition, old solutions lead to less quality of the deposited material and thus, less performance.

About the voltage of the cell, it is reported as 1.04 V (1047.78 mV) for the reference cell in Table 6.6. In a module with series connected cells, the total voltage is the sum of the voltage produced from each cell. The Figure 6.24 shows that the V_{OC} for E4 and E5 is near 5 V, while for E6 is nearly 4 V. In this case, the voltage can be decreased because of the malfunction of one or more of the cells. Another cause can be a slightly lower voltage force in each of the cells. Additional analysis needs to be performed to find the origin of this behavior.

The series resistance is calculated with a regression of the IV curve near the V_{OC} is plotted, the inverse of the slope its absolute value is the series resistance in Ωcm^2 . The shunt resistance, on the other side, is obtained with the dispersion of the IV curve near the J_{SC} and the same posterior calculation.

The s-shape of the E4 and E5 IV-curve can have origin on the barrier resistance exerted by the residual SnO₂ of the P2 scribe. Moreover, the series resistance can also influence on the curvature of the line. Given this, the series resistance calculated by the graphic method cannot be accurate for this analysis. These resistances are related with the reduction of the FF for all the devices.

The calculated values for the shunt resistance are listed in Table 6.7. The J_{SC} is nearly the same for all the devices, the same trend happens for the FF.

This analysis confirms that the sample E4 has high shunt resistance in the backward mode, which is related to the better curve fit near de J_{SC} . The V_{OC} is coherent with the amount of cells and the voltage that each one can produce.

Regarding the device E5, it had the greatest shunt resistance, with an estimated value of 20 $k\Omega cm^2$ this value is comparable with the PBCM/Ag based devices [61]. This is also noticeable in the curve shape near the J_{SC} in the forward scan. In terms of voltage, there is a slight decrease of this value compared to E4

The module E6 had low shunt resistance. Moreover, this device had the worst performance of the three cells, which can be related to the high shunting on the module. The low voltage of this

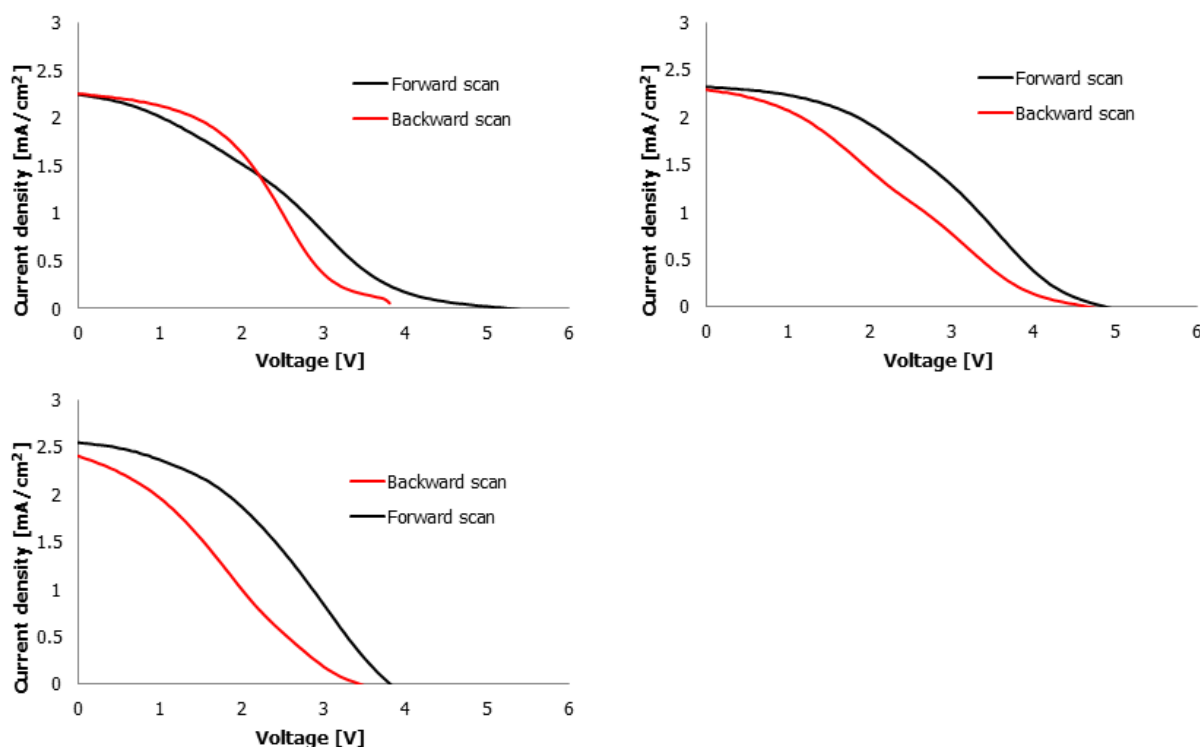


Figure 6.24: IV curves for the modules E4 (top left), E5 (top right), and E6 (bottom left)

devices would infer that some of the cells are not working, and thus not contributing with the V_{OC} of the device.

Table 6.7: Complete characterization of the semi transparent perovskite modules.

	E4		E5		E6	
	Forward	Backward	Forward	Backward	Forward	Backward
V_{OC} [mV]	5.26	3.8	4.87	4.65	3.81	3.43
I_{SC}/cm^2 [mA/cm ²]	2.24	2.25	2.32	2.28	2.40	2.40
FF [%]	26.13	26	35.98	26.93	27.70	27.70
MP/cm ² [mW/cm ²]	3.08	2.22	4.06	2.87	2.29	2.29
Efficiency [%]	3.08	2.22	4.06	2.87	2.29	2.29
R_{shunt} [k Ω cm ²]	10	12.5	20	11.1	16.66	5

The semi transparent nature of the module makes it suitable for illumination on both sides. It is believed that the n-i-p also gives enhanced results. The samples were additionally illuminated from the back side to check the performance.

The IV-curves can be seen in Figure 6.25. For the module E4, less shunt resistance is appreciated and the current density improved to 3 mA cm^2 , the voltage keeps the same value. Regard to E5 and E6 devices a resistance is present. The calculation of shunt and series resistance is made to determine which phenomena dominate in each case. Nonetheless, given the irregular shape of some curves, the series resistance cannot be stated as correct.

The Table 6.8 shows the characterization of the modules in rear illumination. The module E4 shows no change in shunt resistance. However, its more regular curve fit the CPE is improved up to of 5.22 %. This increase of the efficiency is directly related to the architecture of the cells when the light enters from the back side, it passes through the ITO and SnO₂ with an average width of 230 nm

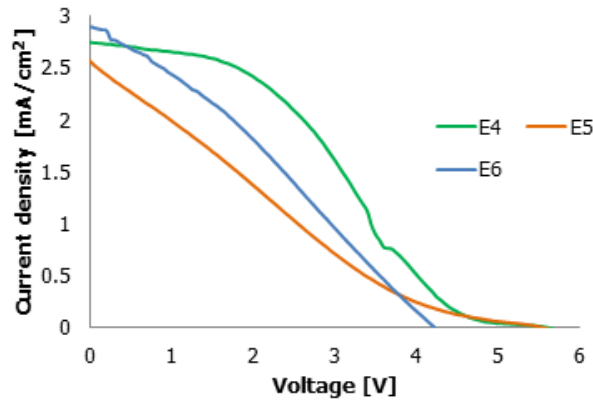


Figure 6.25: IV curves for the modules illuminated from the rear side in forward scan

for both layers, this it is easily absorbed in the perovskite layer. Then the light enters from the top side, and it needs to travel through 420 nm before reaching the light absorbing layer, this doubled distance is not only the hindering factor.

Moreover, the MoO_3 and spiro-OMeTAD are slightly opaque. Thus the light is not completely transmitted and leads to losses. The E4 device presented an increase of the performance with an efficiency of 5.22 %, the highest value for all the tests. The curve shows a decreased shunt resistance. The FF increased from 26 % to 34.29 %. IN this case, the curve had a slight irregularity near the V_{OC} , this can be because of a measurement error of the Wacom system. Regarding the sample E6, the efficiency kept constant, and the performance had no significant difference with the front illuminated test.

Table 6.8: Complete characterization of the semi transparent perovskite modules with rear illumination. Forward scan

	E4	E5	E6
V_{OC} [mV]	5.55	5.51	4.21
I_{SC}/cm^2 [mA/cm^2]	2.74	2.61	2.88
FF [%]	34.29	19.36	29.84
MP/cm^2 [mW/cm^2]	5.22	2.80	3.62
Efficiency [%]	5.22	2.80	3.62
R_{shunt} [$\text{k}\Omega \text{ cm}^2$]	12.5	1.42	1.66

Further methods were applied to determine the causes for the performance behavior of each device. The selected tests were photoluminescence, illuminated lock-in thermography, and dark lock-in thermography

The samples were analyzed with photoluminescence (Figure 6.26) to check the reaction to photo stimulation and find the possible origin of the poor performance in some samples. The module E4 shows a uniform profile regarding response to the light. Besides, it has relatively broad interconnection areas, and this situation leads to a decrease of the GFF. The module E5 (b) has a differentiated appearance, only the second and fifth cell seem to work correctly, while the third and fourth are affected by a spot defect from the spin coating, this has a remarkable effect on the third cell which shows the weakest excitation to the light. Lastly, the device E6 present a localized defect from the spin coating. However, it does not affect the photo stimulation of the cell.

Additionally, the second and sixth cell had less stimulation because of material defect that can be seen in the image. A peculiarity of the primary defect in cells E5 and E6 is the difference of oper-

ation influenced by the localization of the irregularity. E5 defect is located on the interconnection, which leads to the low performance of the adjacent cells because of shunting. E6 had the hole on one of the cells, which did not affect the cell response to light and did not affect the neighbor cells. Both spots were also analyzed with electron microscopy. This test shows that the spot on E5 has a lack of C, which is related to spiro-OMeTAD. In the case of the irregularity in E6, it has a lack of Pb, and this infers a void of perovskite material.

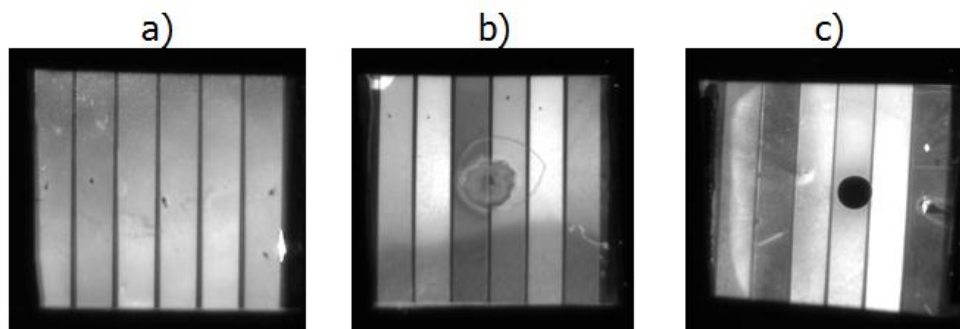


Figure 6.26: Photoluminescence test for perovskite modules. (a) Best performing module labeled as E4, (b) Low performing module, labeled as E5, (c) middle performing module, labeled as E6. The dark stripes between the cells are the interconnection, which has no photoactivity.

Another test to locate anomalies is the Lock-in thermography, which can determine shunting effect due to the heat of the material in such areas. The Figure 6.27 shows in (a) the almost absence of overheat area in module E4, only a small warm area is marked on the right side of the device. Respect to E5 (b) the shunt is present in the same area as the void spot, with a stronger presence in the third cell. A positive effect of the interconnection shows a reduction of the shunting in the fourth cell. Lastly, the module E6 (c) has a small shunting between the first and second cell that is identified as an anomaly that hinders the performance of the second cell. The void of the fourth cell is also detected as a recombination center.

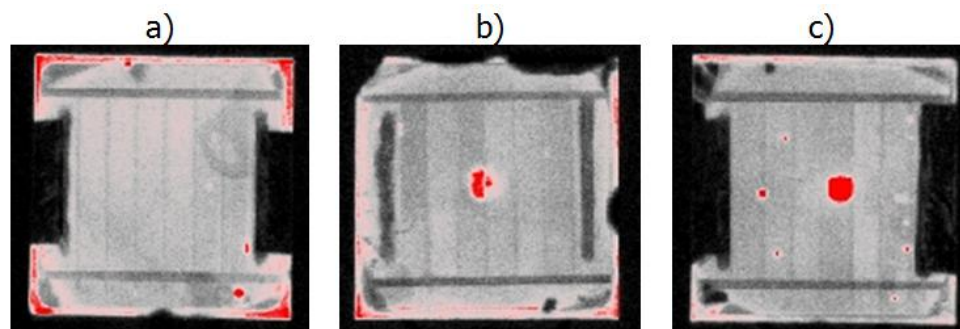


Figure 6.27: Lock-in thermography test for perovskite modules. (a) Best performing module labeled as E4, (b) Low performing module, labeled as E5, (c) middle performing module, labeled as E6.

The dark lock-in thermography helps to simulate the operation of the module and identify its response. The method is based on the application of forward bias in the dark conditions [62].

The Figure 6.28 shows the results of these tests. For the module E4 (a) the sample does not show any thermal response. This suggests that E4 is a good performing device, it can also be related to the low shunt resistance presented in Table 6.7. Respect to E5 (b) some of the cells show shunting. The void area seen in photoluminescence and lock-in thermography is responsible for shunting according to the images. Furthermore, most of the cells present shunts, this can prove the highest value for this characteristic listed in Table 6.7. Finally, E6 (c) shows localized shunting, which also

coincides with non-uniformity of the layer, this could mean that the current leakage occurs because of a defect in the material.

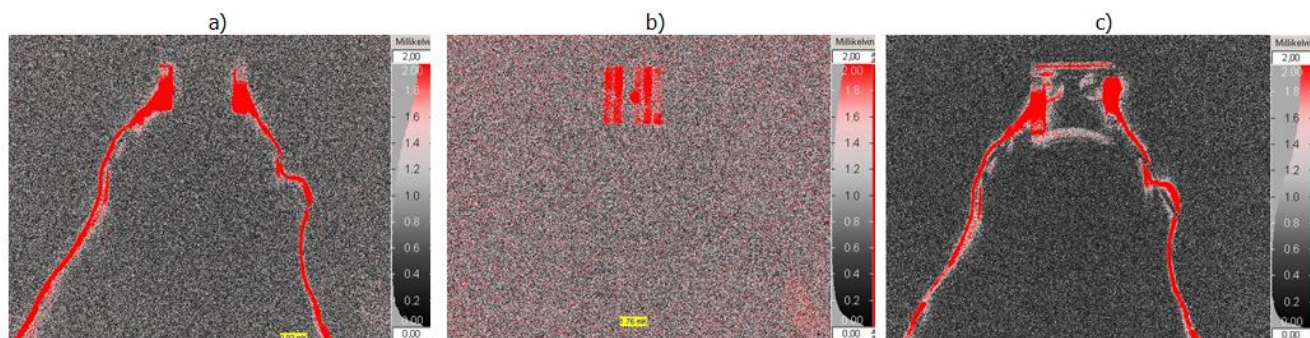


Figure 6.28: Dark lock-in thermography test for perovskite modules. (a) Best performing module labeled as E4, (b) Low performing module, labeled as E5, (c) middle performing module, labeled as E6.

6.7. ADDITIONAL P2 SCRIBE

Due to the issue of the P2 scribe in this batch, an additional test is performed with a spare sample of the bundle. The increase of the apparent power in 100 mW (3.4 mW real power) showed not significant effect on the material ablation. Nonetheless, the reduction of the scribing speed showed a positive impact on the SnO_2 removal compared to Figure 6.20. The best scribing speed for this batch is 40 mm/s, which shows a complete electrode exposition.

The Figure 6.29 shows the front image of the scribe performed at 40 mm/s with 50x magnification (a), the electrode stripe had an average 7 μm width. The cross-sectional image shows a wider profile compared to the Figure 6.20, which is better for the interconnection and avoid current crowding. The valley had a broader ablation between 100 and -300 nm in (b), this gives a rough approximation of the spiro-OMeTAD thickness

Therefore, the P2 scribed line settings are set with a power of 17.9 mW at a range of scribing speed between 40 and 60 mm/s, a value that is determined by the thicknesses of the layers for each batch.

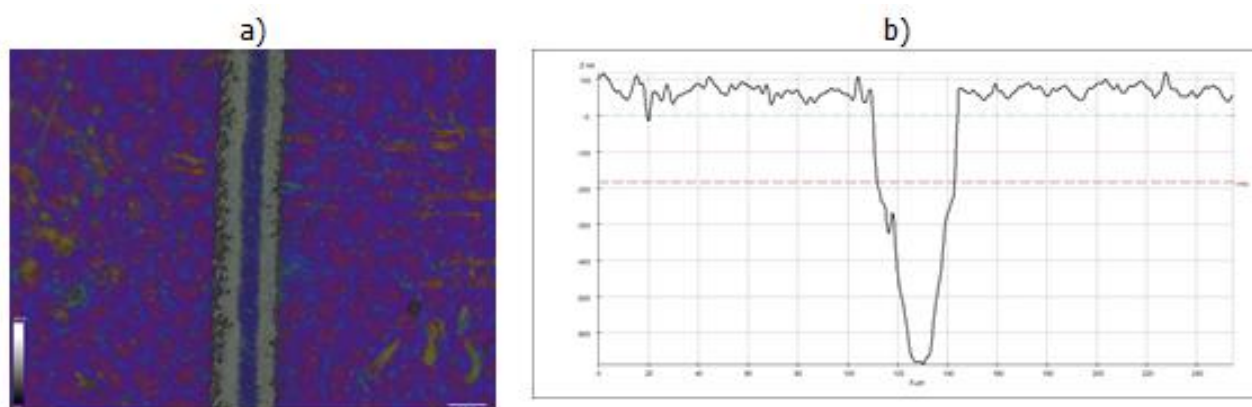


Figure 6.29: Additional P2 scribe test. (a) 50x magnification with confocal microscopy in white light mode, (b) cross sectional profile with confocal microscopy in topography mode.

The presented test showed the need to make a quick ablation test before the full scribing process; this can be carried out with an improve safety system for the perovskite ablation that allows the change of sample right after laser processing

7

CONCLUSIONS AND RECOMMENDATIONS

7.1. CONCLUSIONS

The aim of this project was the development and optimization of the laser processing to produce an efficient semi transparent perovskite cell. Manufacturing working devices with acceptable characteristics were possible. However, some features decreased the performance of the modules.

Several aspects are involved with the manufacturing and the final performance of the device: the selected materials and its deposition techniques, laser characteristics, and layout of the module. Each of the parameters was analyzed to find their impact on the module processing.

For the laser set up, a UV laser was preferred because of the optical absorption by all layers of the module. The pulse length of 1 ps at a frequency of 10 kHz generates a satisfactory beam, regarding the pulse energy; this case required less apparent power.

The P1 scribe faced issues of crystallization and cracking effect, especially for the amorphous ITO layer. These problems were overcome with a configuration of 1800 mW at 40 *mm/s* and 1500 mW at 30 *mm/s* for the commercial and home-sputtered ITO, respectively.

The P2 scribing line dealt with several aspects such as width and depth of scribe, adjacent damaged material, bottom ITO layer integrity, and SnO₂ removal. The selected settings for this step are 1300 mW at 60 *mm/s* scribing speed. The TLM showed a comparable ρ_c for the stack contact with the non-transparent device with front gold electrode, with a contact resistivity of $1.20 \times 10^{-3} \Omega \text{cm}^2$ and $2.81 \times 10^{-4} \Omega \text{cm}^2$, respectively.

The final P3 line set up had unavoidable delamination effect on the front film, basically caused by the weak capacity against the thermal stress of the amorphous ITO. Moreover, the damage to spiro-OMeTAD is also present. The chosen settings for this scribe are 1300 mW apparent power and 40 *mm/s* scribing speed.

For this device, the stack was deposited in the n-i-p configuration, starting with ITO, then SnO₂, triple cation perovskite, spiro-OMeTAD, MoO₃, and front ITO electrode. This architecture achieved a 10.95 CPE for a single cell. The configuration of the laser system was fixed to 335 nm wavelength (UV laser), 10 kHz frequency, 1 ps pulse length for the general operation of the system. For these conditions, the most suitable scribing speed was around 40 *mm/s*. Respect to the apparent power, 1500, and 1300 mW were used for P1, P2, and P3, respectively.

The microscopy analysis showed a correct laser processing with no significant damage to the stack. However, the SnO₂ ablation was not sufficient in the P2 scribe, this was reflected in the series resistance barrier of the IV-curves. This issue is caused by two main factors: the variation of thickness on this stack and the narrow optical field of the laser.

About the shunt resistance, the illuminated and dark-lock in thermography showed the presence of this phenomena in the defect areas, mainly caused by deposition mistakes.

The highest CPE for the produced modules were 4.06 % and 5.22 % for the front and rear illumination of the devices. These efficiencies are affected by different factors that were identified and can be corrected for upcoming projects

7.2. RECOMMENDATIONS

The laser scribing is a complex process that requires specialized handling to ensure accurate results. Regarding the laser misalignment due to the low visibility of the positioning markers, the issue can be solved making the crosses more visible by double or triple pass of the beam. Furthermore, the coordinates for each substrate trace need to be recorded to use them as a back-up in case that the markers are not easy to detect.

About the focusing and system deviation, the samples should be processed one at a time placing them in the center of the process box. This is because the narrow optical field of the UV laser has different results in areas far from the midpoint. In this work, the samples were scribed in batches of six samples placed around the center of the box. This arrangement followed the safety measures of the perovskite ablation, which is time-consuming and not practical. The laser box has a valve integrated to connect a flow system that removes the polluted atmosphere. A flow purifier system is required for the post-treatment of the air. The upgrade would help to process the modules one by one.

Given the higher efficiency of the rear illuminated module, a p-i-n architecture can be analyzed for the development of a semi transparent module. Nonetheless, this arrangement would need a change of the HTL and ETL given the post treatment of the triple cation perovskite and SnO_2 .

BIBLIOGRAPHY

- [1] A. Smets, K. Jäger, O. Isabella, R. van Swaaij, and M. Zeman, *Solar Energy The physics and engineering of photovoltaic conversion, technologies and systems* (UIT Cambridge, 2016).
- [2] I. I. E. Agency, *Key world energy statistics*. (2016).
- [3] M. Perez and R. Perez, *Update 2015—a fundamental look at supply side energy reserves for the planet*, *Natural Gas* **2**, 215 (2015).
- [4] S. Europe, *Global market outlook for solar power / 2017 - 2021*, (2017).
- [5] P. J. Cousins, D. D. Smith, H.-C. Luan, J. Manning, T. D. Dennis, A. Waldhauer, K. E. Wilson, G. Harley, and W. P. Mulligan, *Generation 3: Improved performance at lower cost*, in *Photovoltaic Specialists Conference (PVSC), 2010 35th IEEE* (IEEE, 2010) pp. 000275–000278.
- [6] N. N. R. E. Laboratory, *Best research-cell efficiencies*. (2016).
- [7] T. P. White, N. N. Lal, and K. R. Catchpole, *Tandem solar cells based on high-efficiency c-si bottom cells: top cell requirements for > 30% efficiency*, *IEEE Journal of Photovoltaics* **4**, 208 (2014).
- [8] E. H. Anaraki, A. Kermanpur, L. Steier, K. Domanski, T. Matsui, W. Tress, M. Saliba, A. Abate, M. Grätzel, A. Hagfeldt, *et al.*, *Highly efficient and stable planar perovskite solar cells by solution-processed tin oxide*, *Energy & Environmental Science* **9**, 3128 (2016).
- [9] D. P. McMeekin, G. Sadoughi, W. Rehman, G. E. Eperon, M. Saliba, M. T. Hörantner, A. Haghighirad, N. Sakai, L. Korte, B. Rech, *et al.*, *A mixed-cation lead mixed-halide perovskite absorber for tandem solar cells*, *Science* **351**, 151 (2016).
- [10] S. S. Shin, E. J. Yeom, W. S. Yang, S. Hur, M. G. Kim, J. Im, J. Seo, J. H. Noh, and S. I. Seok, *Colloidally prepared la-doped basno₃ electrodes for efficient, photostable perovskite solar cells*, *Science* **356**, 167 (2017).
- [11] D. Bryant, N. Aristidou, S. Pont, I. Sanchez-Molina, T. Chotchunangatchaval, S. Wheeler, J. R. Durrant, and S. A. Haque, *Light and oxygen induced degradation limits the operational stability of methylammonium lead triiodide perovskite solar cells*, *Energy Environ. Sci.* **9**, 1655 (2016).
- [12] G. E. Eperon, T. Leijtens, K. A. Bush, R. Prasanna, T. Green, J. T.-W. Wang, D. P. McMeekin, G. Volonakis, R. L. Milot, R. May, *et al.*, *Perovskite-perovskite tandem photovoltaics with optimized band gaps*, *Science* **354**, 861 (2016).
- [13] M. A. Green, A. Ho-Baillie, and H. J. Snaith, *The emergence of perovskite solar cells*, *Nature Photonics* **8**, 506 (2014).
- [14] M. Saliba, T. Matsui, J.-Y. Seo, K. Domanski, J.-P. Correa-Baena, M. K. Nazeeruddin, S. M. Zaakeeruddin, W. Tress, A. Abate, A. Hagfeldt, *et al.*, *Cesium-containing triple cation perovskite solar cells: improved stability, reproducibility and high efficiency*, *Energy & environmental science* **9**, 1989 (2016).

- [15] C. C. Stoumpos, C. D. Malliakas, and M. G. Kanatzidis, *Semiconducting tin and lead iodide perovskites with organic cations: phase transitions, high mobilities, and near-infrared photoluminescent properties*, *Inorganic chemistry* **52**, 9019 (2013).
- [16] H. Choi, J. Jeong, H.-B. Kim, S. Kim, B. Walker, G.-H. Kim, and J. Y. Kim, *Cesium-doped methylammonium lead iodide perovskite light absorber for hybrid solar cells*, *Nano Energy* **7**, 80 (2014).
- [17] J.-W. Lee, D.-H. Kim, H.-S. Kim, S.-W. Seo, S. M. Cho, and N.-G. Park, *Formamidinium and cesium hybridization for photo- and moisture-stable perovskite solar cell*, *Advanced Energy Materials* **5** (2015).
- [18] C. Yi, J. Luo, S. Meloni, A. Boziki, N. Ashari-Astani, C. Grätzel, S. M. Zakeeruddin, U. Röhli-berger, and M. Grätzel, *Entropic stabilization of mixed a-cation abx₃ metal halide perovskites for high performance perovskite solar cells*, *Energy & Environmental Science* **9**, 656 (2016).
- [19] Z. Li, M. Yang, J.-S. Park, S.-H. Wei, J. J. Berry, and K. Zhu, *Stabilizing perovskite structures by tuning tolerance factor: formation of formamidinium and cesium lead iodide solid-state alloys*, *Chemistry of Materials* **28**, 284 (2015).
- [20] W. Ke, G. Fang, Q. Liu, L. Xiong, P. Qin, H. Tao, J. Wang, H. Lei, B. Li, J. Wan, *et al.*, *Low-temperature solution-processed tin oxide as an alternative electron transporting layer for efficient perovskite solar cells*, *Journal of the American Chemical Society* **137**, 6730 (2015).
- [21] K. A. Bush, C. D. Bailie, Y. Chen, A. R. Bowring, W. Wang, W. Ma, T. Leijtens, F. Moghadam, and M. D. McGehee, *Thermal and environmental stability of semi-transparent perovskite solar cells for tandems enabled by a solution-processed nanoparticle buffer layer and sputtered iTO electrode*, *Advanced Materials* (2016).
- [22] H. Kim, C. Gilmore, A. Pique, J. Horwitz, H. Mattoussi, H. Murata, Z. Kafafi, and D. Chrisey, *Electrical, optical, and structural properties of indium-tin-oxide thin films for organic light-emitting devices*, *Journal of Applied Physics* **86**, 6451 (1999).
- [23] F. Fu, T. Feurer, T. Jäger, E. Avancini, B. Bissig, S. Yoon, S. Buecheler, and A. N. Tiwari, *Low-temperature-processed efficient semi-transparent planar perovskite solar cells for bifacial and tandem applications*, *Nature communications* **6** (2015).
- [24] T. Leijtens, G. E. Eperon, S. Pathak, A. Abate, M. M. Lee, and H. J. Snaith, *Overcoming ultraviolet light instability of sensitized tio₂ with meso-superstructured organometal tri-halide perovskite solar cells*, *Nature communications* **4** (2013).
- [25] P. Tiwana, P. Docampo, M. B. Johnston, H. J. Snaith, and L. M. Herz, *Electron mobility and injection dynamics in mesoporous zno, sno₂, and tio₂ films used in dye-sensitized solar cells*, *ACS nano* **5**, 5158 (2011).
- [26] C. Roldán-Carmona, O. Malinkiewicz, R. Betancur, G. Longo, C. Momblona, F. Jaramillo, L. Camacho, and H. J. Bolink, *High efficiency single-junction semitransparent perovskite solar cells*, *Energy & Environmental Science* **7**, 2968 (2014).
- [27] W. H. Nguyen, C. D. Bailie, E. L. Unger, and M. D. McGehee, *Enhancing the hole-conductivity of spiro-ometad without oxygen or lithium salts by using spiro (tfsi) 2 in perovskite and dye-sensitized solar cells*, *Journal of the American Chemical Society* **136**, 10996 (2014).

- [28] C. D. Bailie, M. G. Christoforo, J. P. Mailoa, A. R. Bowring, E. L. Unger, W. H. Nguyen, J. Burschka, N. Pellet, J. Z. Lee, M. Grätzel, *et al.*, *Semi-transparent perovskite solar cells for tandems with silicon and cigs*, *Energy & Environmental Science* **8**, 956 (2015).
- [29] F. Liu, S. Shao, X. Guo, Y. Zhao, and Z. Xie, *Efficient polymer photovoltaic cells using solution-processed moo3 as anode buffer layer*, *Solar Energy Materials and Solar Cells* **94**, 842 (2010).
- [30] K. Kanai, K. Koizumi, S. Ouchi, Y. Tsukamoto, K. Sakanoue, Y. Ouchi, and K. Seki, *Electronic structure of anode interface with molybdenum oxide buffer layer*, *Organic Electronics* **11**, 188 (2010).
- [31] G. E. Eperon, S. D. Stranks, C. Menelaou, M. B. Johnston, L. M. Herz, and H. J. Snaith, *Formamidinium lead trihalide: a broadly tunable perovskite for efficient planar heterojunction solar cells*, *Energy & Environmental Science* **7**, 982 (2014).
- [32] T. C. Sum and N. Mathews, *Advancements in perovskite solar cells: photophysics behind the photovoltaics*, *Energy & Environmental Science* **7**, 2518 (2014).
- [33] H.-S. Kim, C.-R. Lee, J.-H. Im, K.-B. Lee, T. Moehl, A. Marchioro, S.-J. Moon, R. Humphry-Baker, J.-H. Yum, J. E. Moser, *et al.*, *Lead iodide perovskite sensitized all-solid-state submicron thin film mesoscopic solar cell with efficiency exceeding 9%*, *Scientific reports* **2**, 591 (2012).
- [34] L.-j. Meng and M. Dos Santos, *Properties of indium tin oxide films prepared by rf reactive magnetron sputtering at different substrate temperature*, *Thin Solid Films* **322**, 56 (1998).
- [35] G. Yang, C. Wang, H. Lei, X. Zheng, P. Qin, L. Xiong, X. Zhao, Y. Yan, and G. Fang, *Interface engineering in planar perovskite solar cells: energy level alignment, perovskite morphology control and high performance achievement*, *Journal of Materials Chemistry A* **5**, 1658 (2017).
- [36] N. Yamazoe, K. Shimano, and C. Sawada, *Contribution of electron tunneling transport in semiconductor gas sensor*, *Thin Solid Films* **515**, 8302 (2007).
- [37] T.-b. Song, Q. Chen, H. H.-P. Zhou, C. Jiang, H.-H. Wang, Y. (Michael) Yang, Y. Liu, J. You, Y. Yang, Y. Liu, J. You, Y. (Michael) Yang, Y. Liu, J. You, and Y. Yang, *Perovskite solar cells: film formation and properties*, *Journal of Materials Chemistry A* **3**, 9032 (2015).
- [38] J. Liu, S. Shao, G. Fang, B. Meng, Z. Xie, and L. Wang, *High-efficiency inverted polymer solar cells with transparent and work-function tunable moo3-al composite film as cathode buffer layer*, *Advanced Materials* **24**, 2774 (2012).
- [39] S. Murase and Y. Yang, *Solution processed moo3 interfacial layer for organic photovoltaics prepared by a facile synthesis method*, *Advanced materials* **24**, 2459 (2012).
- [40] M. Liu, M. B. Johnston, and H. J. Snaith, *Efficient planar heterojunction perovskite solar cells by vapour deposition*, *Nature* **501**, 395 (2013).
- [41] P. Kelly and R. Arnell, *Magnetron sputtering: a review of recent developments and applications*, *Vacuum* **56**, 159 (2000).
- [42] M. M. Inc, *Magnetron sputtering technology*, (2017).
- [43] A. I. inc, *Sputter 4 (aja atc 2200-v)*, (2016).
- [44] N. Sahu, B. Parija, and S. Panigrahi, *Fundamental understanding and modeling of spin coating process: A review*, *Indian Journal of Physics* **83**, 493 (2009).

- [45] F. C. Krebs, *Fabrication and processing of polymer solar cells: a review of printing and coating techniques*, Solar energy materials and solar cells **93**, 394 (2009).
- [46] A. K. Dubey and V. Yadava, *Laser beam machining—a review*, International Journal of Machine Tools and Manufacture **48**, 609 (2008).
- [47] S. E., *The basic principles of laser technology*, Tutorial (2012), uses and safety measures in anaesthesia.
- [48] D. W. Bäuerle, *Laser processing and chemistry* (Springer Science & Business Media, 2013).
- [49] K.-H. Leitz, B. Redlingshöfer, Y. Reg, A. Otto, and M. Schmidt, *Metal ablation with short and ultrashort laser pulses*, Physics Procedia **12**, 230 (2011).
- [50] M. Ghosh and A. Raychaudhuri, *Field induced reversible control of visible luminescence in zno nanostructures*, arXiv preprint arXiv:0903.3735 (2009).
- [51] J. Xu, Y. Li, H. Huang, Y. Zhu, Z. Wang, Z. Xie, X. Wang, D. Chen, and G. Shen, *Synthesis, characterizations and improved gas-sensing performance of sno 2 nanospike arrays*, Journal of Materials Chemistry **21**, 19086 (2011).
- [52] J. Liu, Y. Wu, C. Qin, X. Yang, T. Yasuda, A. Islam, K. Zhang, W. Peng, W. Chen, and L. Han, *A dopant-free hole-transporting material for efficient and stable perovskite solar cells*, Energy & Environmental Science **7**, 2963 (2014).
- [53] B. Muhsin, J. Renz, K.-H. Drüe, G. Gobsch, and H. Hoppe, *Efficient polymer solar cell modules*, Synthetic Metals **159**, 2358 (2009).
- [54] P. Kubis, N. Li, T. Stubhan, F. Machui, G. J. Matt, M. M. Voigt, and C. J. Brabec, *Patterning of organic photovoltaic modules by ultrafast laser*, Progress in Photovoltaics: Research and Applications **23**, 238 (2015).
- [55] R. S. Patel, J. Bovatsek, and A. Tamhankar, *Why pulse duration matters in photovoltaics*, Laser Technik Journal **7**, 21 (2010).
- [56] X. Luo, P. Chen, and Y. Wang, *Power content m^2 -values smaller than one*, Applied Physics B **98**, 181 (2010).
- [57] A. del Campo and E. Arzt, *Generating micro-and nanopatterns on polymeric materials* (John Wiley & Sons, 2011).
- [58] L. Rakocevic, R. Gehlhaar, T. Merckx, W. Qiu, U. W. Paetzold, H. Fledderus, and J. Poortmans, *Interconnection optimization for highly efficient perovskite modules*, IEEE Journal of Photovoltaics **7**, 404 (2017).
- [59] H. Hoppe, M. Seeland, and B. Muhsin, *Optimal geometric design of monolithic thin-film solar modules: Architecture of polymer solar cells*, Solar Energy Materials and Solar Cells **97**, 119 (2012).
- [60] D. K. Schroder, *Semiconductor material and device characterization* (John Wiley & Sons, 2006).
- [61] J. Min, Z.-G. Zhang, Y. Hou, C. O. Ramirez Quiroz, T. Przybilla, C. Bronnbauer, F. Guo, K. Forberich, H. Azimi, T. Ameri, *et al.*, *Interface engineering of perovskite hybrid solar cells with solution-processed perylene-diimide heterojunctions toward high performance*, Chemistry of Materials **27**, 227 (2014).

- [62] O. Breitenstein, J. P. Rakotoniaina, M. Kaes, S. Seren, T. Pernau, G. Hahn, W. Warta, and J. Isenberg, *Lock-in thermography-a universal tool for local analysis of solar cells*, in *Proceedings of the 20th European Photovoltaic Solar Energy Conference and Exhibition, Barcelona (2005)* pp. 6–10.

A

ABLATION THRESHOLD

The Figure A.1 shows the regression to estimate the real power from any apparent power, this line was determined by a series of measurements of the real power delivered by the laser beam.

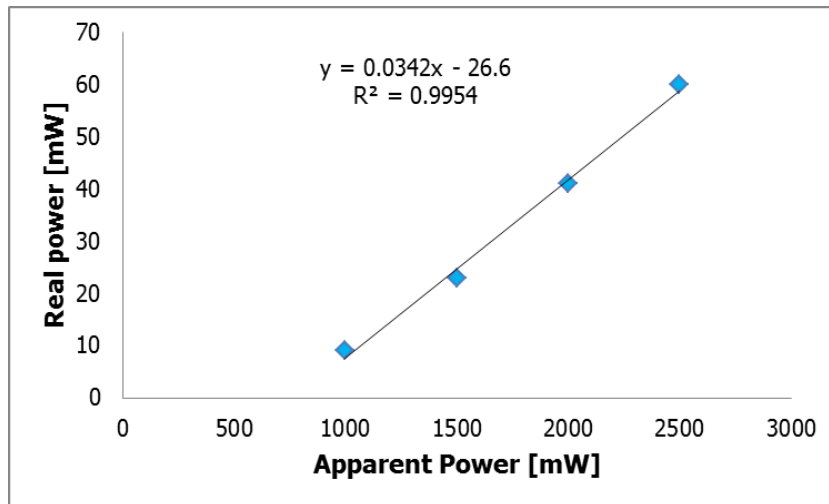


Figure A.1: Apparent power vs measured power of laser beam, in mW.

The pulse energy is calculated with the Formula A.1. Where P_{real} is the measured power in W and f the frequency of beam in Hz . The results are listed in Tables A.1 A.2 and A.3.

$$E_{pulse} = \frac{P_{real}}{f} \quad (A.1)$$

The Table A.1 lists the measured power and calculated energy for the 250 fs laser at diverse frequencies. It is important to remark that the system has limits of operation in terms of power.

At 10 kHz kHz frequency the system cannot go further than 2000 mW, at 20 kHz 5000 mW is the limit power level, and for 50 kHz the maximum power is 9000 mW. From the measurements only the 50 kHz delivered pulse energies from 4.46 to 16.32 $\mu/pulse$

At 10 kHz frequency only the 1 ps pulse length delivered pulse energy from 1 to 6.3 $\mu/pulse$ (Table A.2). The higher pulse length emitted low pulse energy. For this frequency, the 5 and 10 ps pulse length had less intensity.

At 50 kHz, the experiment followed the same trend as for 10 kHz the maximal pulse energy was 4.98 $\mu/pulse$ for 1 ps pulse length with 2500 mW apparent power.

The best selected results for the laser processing are mentioned in Chapter 6

Table A.1: Real power and pulse energy for each frequency at 250 fs pulse length.

250 fs						
Apparent power [mW]	Real power [W]			Pulse energy [μ J/pulse]		
	10 kHz	20 kHz	50 kHz	10 kHz	20 kHz	50 kHz
1000	0.057	0.029	0	5.7	1.45	0
2000	0.154	0.13	0	15.4	6.5	0
3000	error	0.249	0	error	12.45	0
4000	-	0.335	0.223	-	16.75	4.46
5000	-	0.403	0.34	-	20.15	6.8
6000	-	error	0.495	-	error	9.9
7000	-	-	0.589	-	-	11.78
8000	-	-	0.705	-	-	14.1
9000	-	-	0.816	-	-	16.32

Table A.2: Real power and pulse energy for each frequency pulse length at 10 kHz frequency

10 kHz						
Apparent power [mW]	Real power [W]			Pulse Energy [μ J/pulse]		
	1 ps	5 ps	10 ps	1 ps	5 ps	10 ps
1000	0.009	0.002	0.001	0.9	0.2	0.1
2000	0.043	0.007	0.003	4.3	0.7	0.3
2500	0.063	0.013	0.005	6.3	1.3	0.5

Table A.3: Real power and pulse energy for each frequency pulse length at 50 kHz frequency

50 kHz						
Apparent power [mW]	Real power [W]			Pulse Energy [μ J/pulse]		
	1 ps	5 ps	10 ps	1 ps	5 ps	10 ps
4000	0.035	0.002	0.001	0.7	0.04	0.02
6000	0.097	0.008	0.003	1.94	0.16	0.06
9000	0.249	0.027	0.009	4.98	0.54	0.18

The tested samples were commercial ITO on glass and sputtered ITO with the *AJA sputtertool*, the Table A.4 shows the lowest and highest power tested for both samples. As seen in the images from the left side the diameter of the ablated holes starts from 13 and ends to 36 μ m for the commercial samples. Plus the shape of most of the ablated tests were circular and regular. For the case of the sputtered substrate the ablation was slightly different, giving diameters from 8 to 28 μ m for the lowest and highest power tested, respectively. It is also important to remark that the shape of the ablation is irregular compared to the commercial sample.

A regression of the diameter and energy is plotted to find the diameter of beam in the focal plane $2 \omega_0$ With the logarithmic trend line (Figure A.2). The plot to calculate the ablation threshold is on the right side of the figure.

Table A.4: Ablation of ITO samples for commercial and sputtered samples at 250 fs and 50 kHz

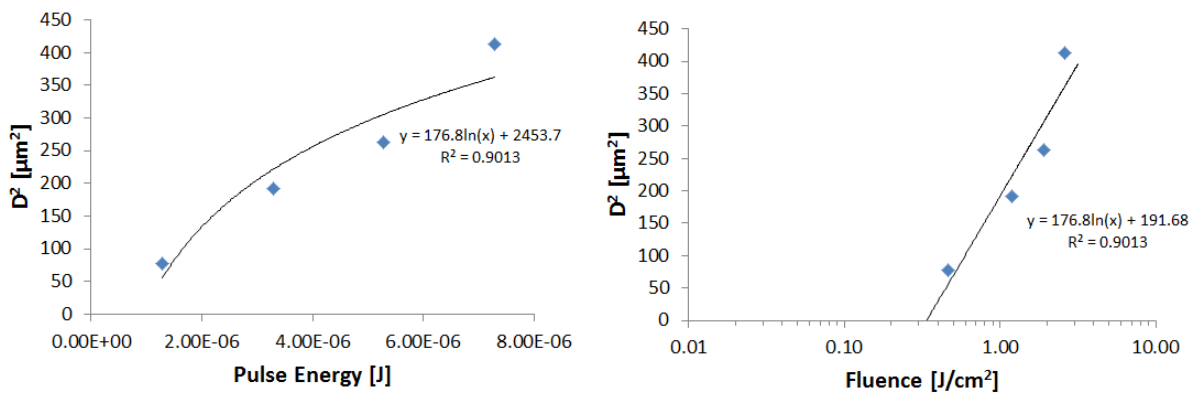
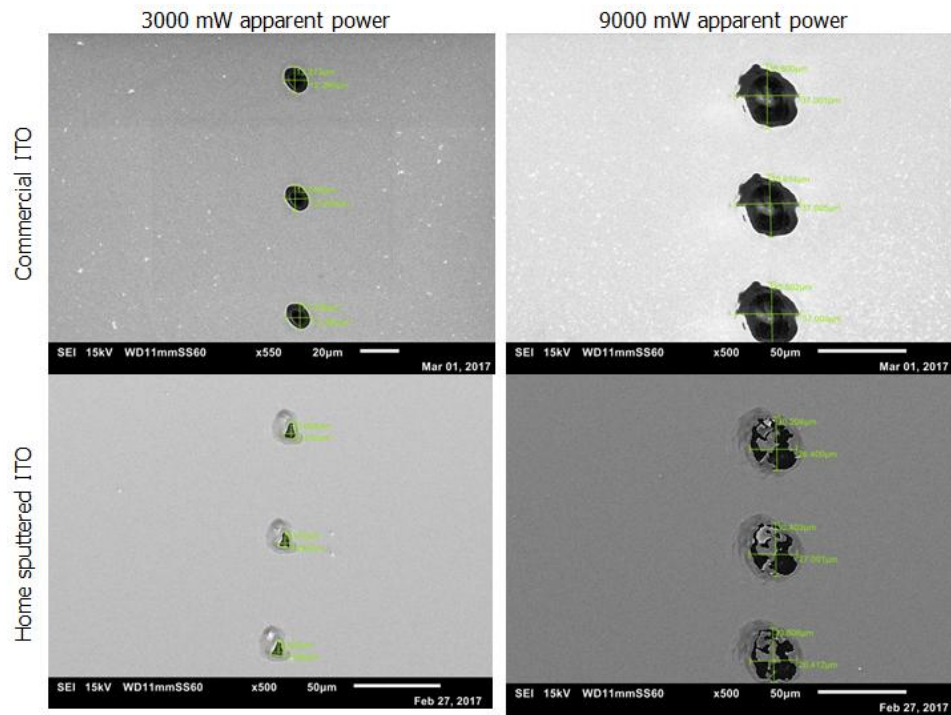


Figure A.2: (left) D^2 of ablated spot (in μm^2) vs pulse energy (in J) for the determination of the diameter of beam in focal plane $2\omega_0$; (right) D^2 of ablated spot (in μm^2) vs pulse energy (in J/cm^2) for the calculation of the ablation threshold F . home sputtered made ITO.

B

POWER SCAN FOR THE P1 SCRIBE

Table B.1: First power scan for the commercial ITO with apparent power between 1000 and 2500 mW at scribing speed from 160 to 10 mm/s, 50x magnification with confocal microscopy in white light mode.

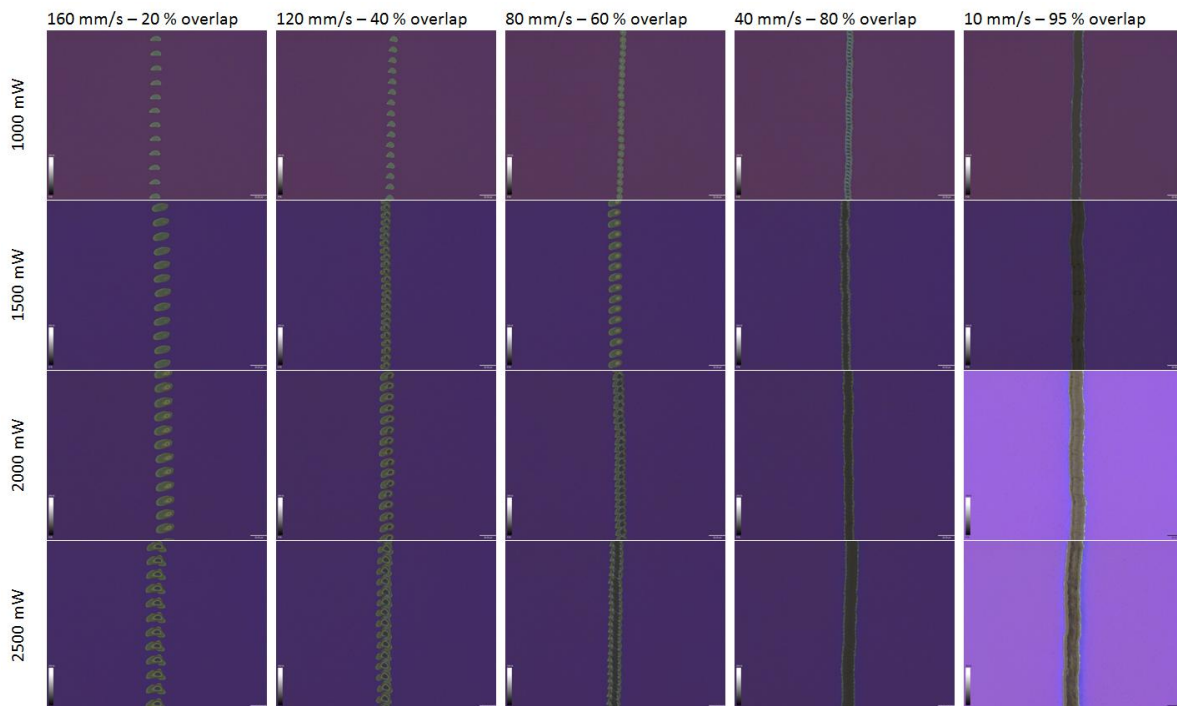


Table B.2: First power scan for the home-sputtered ITO with apparent power between 1000 and 2500 mW at scribing speed from 160 to 10 mm/s, 50x magnification with confocal microscopy in white light mode.

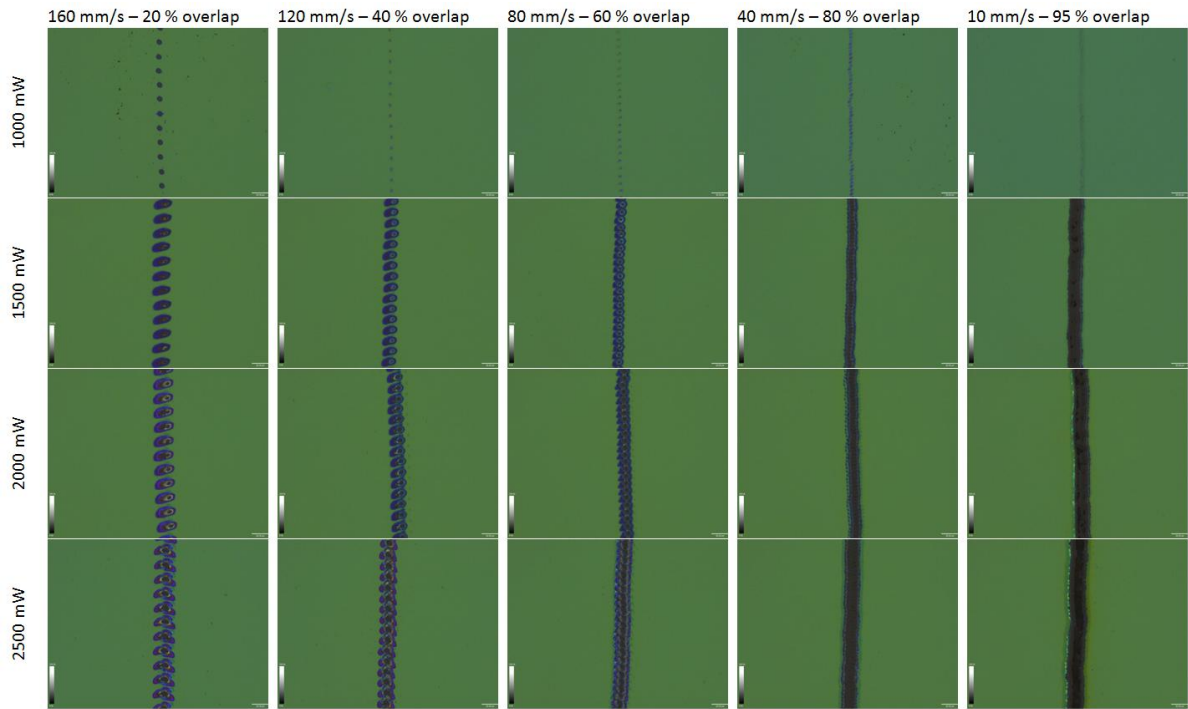


Table B.3: Second power scan for the commercial ITO with apparent power between 1800 and 2100 mW at scribing speed from 80 to 20 mm/s, 50x magnification with confocal microscopy in white light mode.

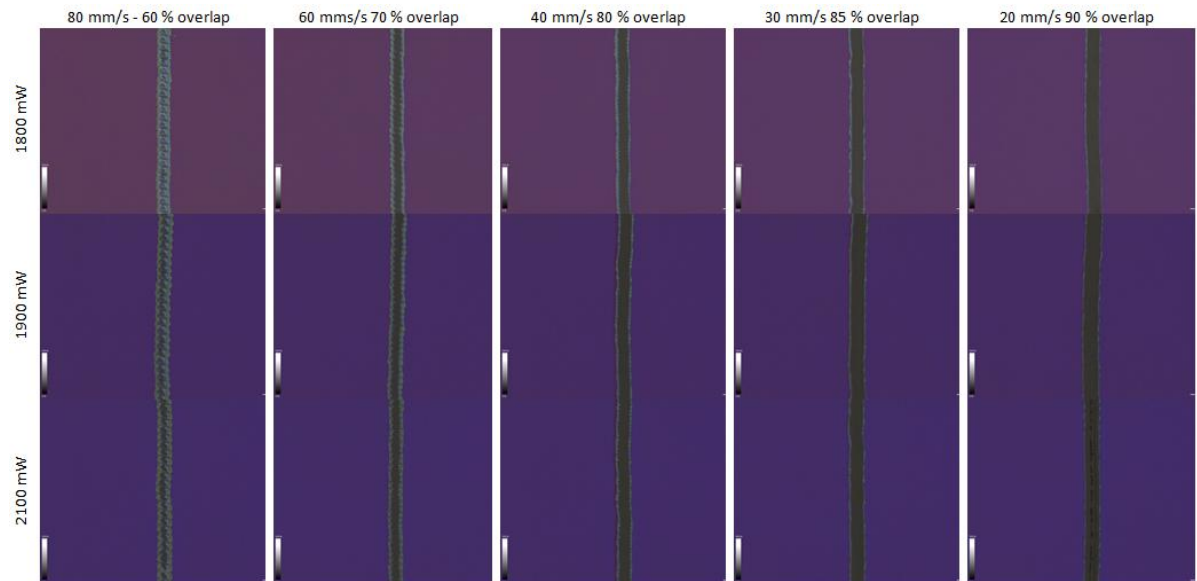


Table B.4: Second power scan for the home-sputtered ITO with apparent power between 1300 and 1600 mW at scribing speed from 80 to 20 mm/s, 50x magnification with confocal microscopy in white light mode.

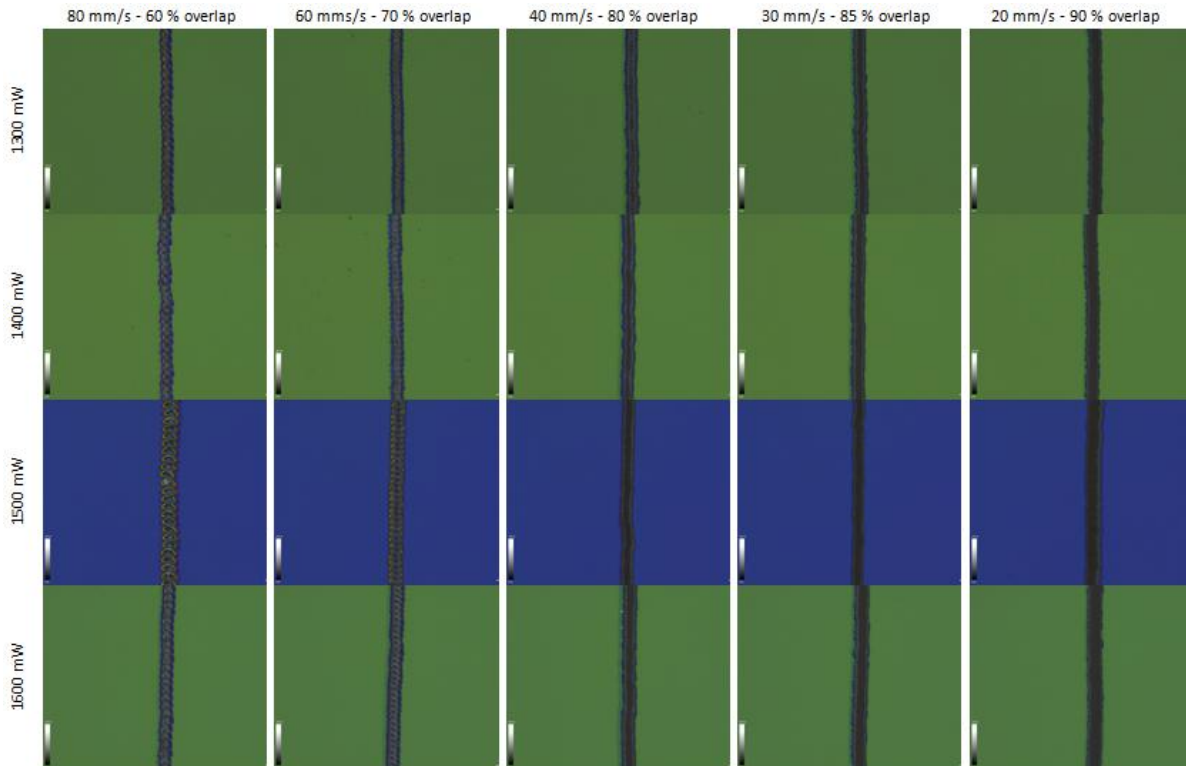


Table B.5: SEM images for isolating lines in commercial ITO samples, 3000x magnification with SEM in scanner mode.

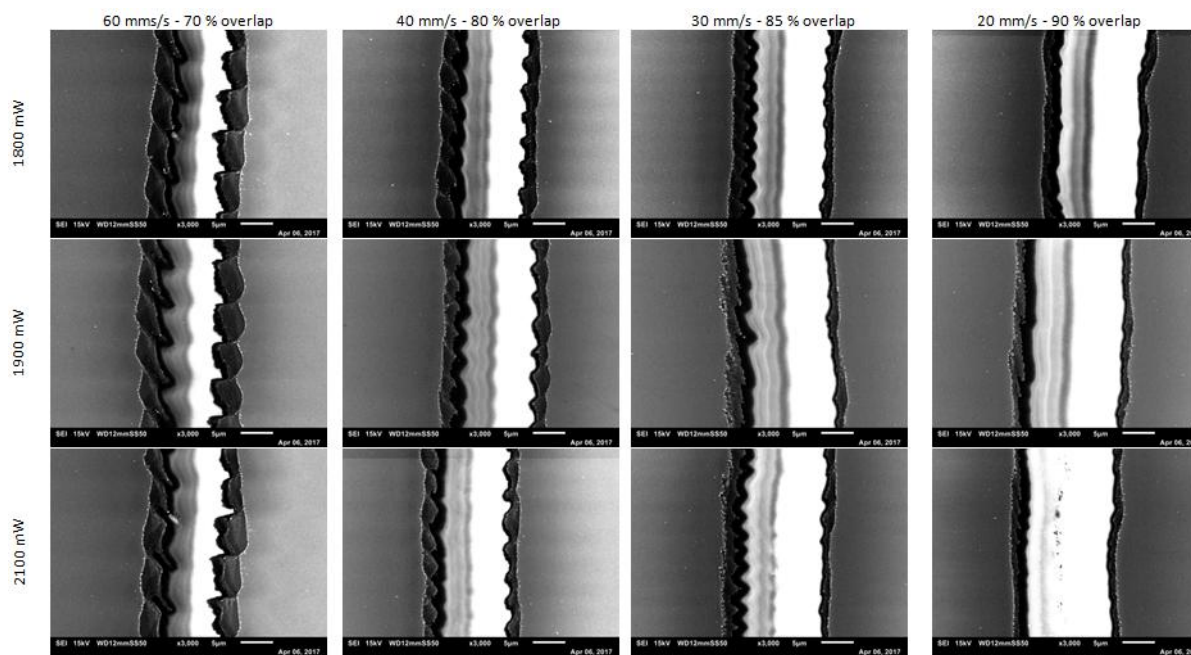
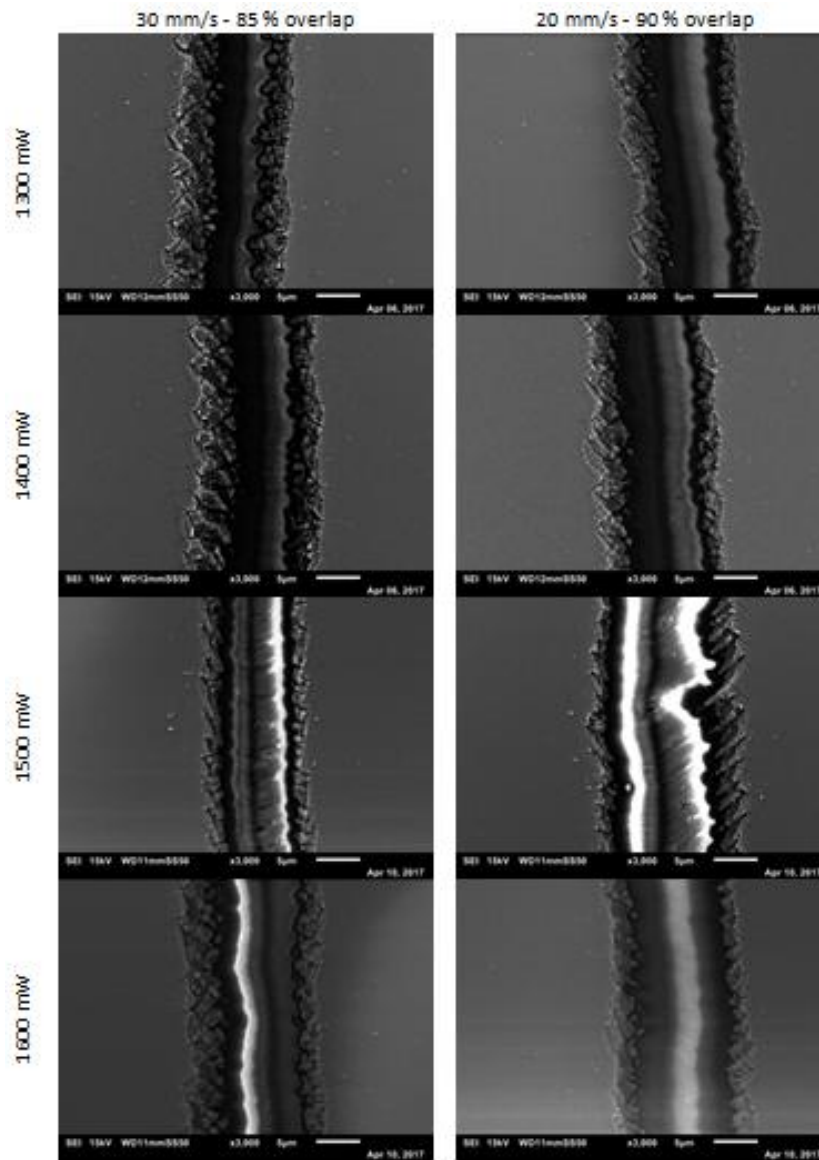


Table B.6: SEM images for the isolating lines in home-sputtered ITO samples, 3000x magnification with SEM in scanner mode.



C

POWER SCAN FOR THE P2 SCRIBE

Table C.1: Confocal microscope images for the first power scan for the P2 scribed line, with apparent power between 1000 and 1800 mW at scribing speed from 80 to 20 mm/s, 50x magnification with confocal microscope in white light mode.

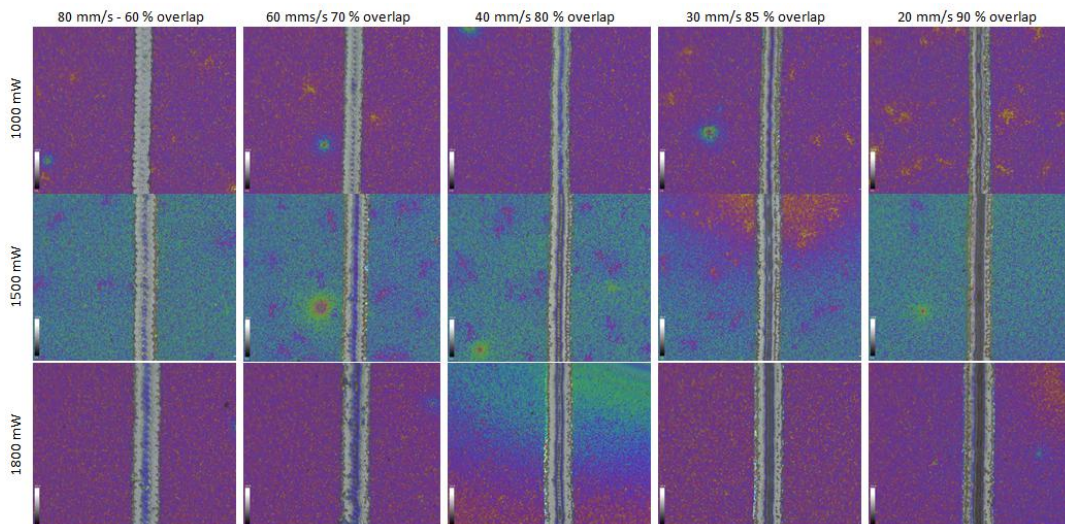


Table C.2: Cross-sectional images with correspondent depth of scribe for the first power scan for the P2 scribed line, with apparent power between 1000 and 1800 mW at scribing speed from 80 to 20 mm/s, cross sectional profile using confocal microscope under topography mode.

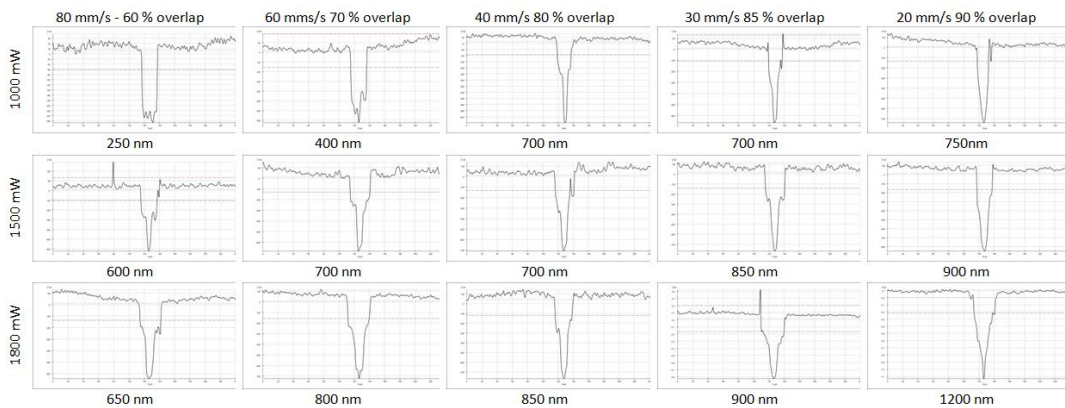


Table C.3: Confocal microscope images for the second power scan for the P2 scribed line, with apparent power between 1100 and 1300 mW at scribing speed from 70 to 30 mm/s , 50x magnification with confocal microscopy in white light mode.

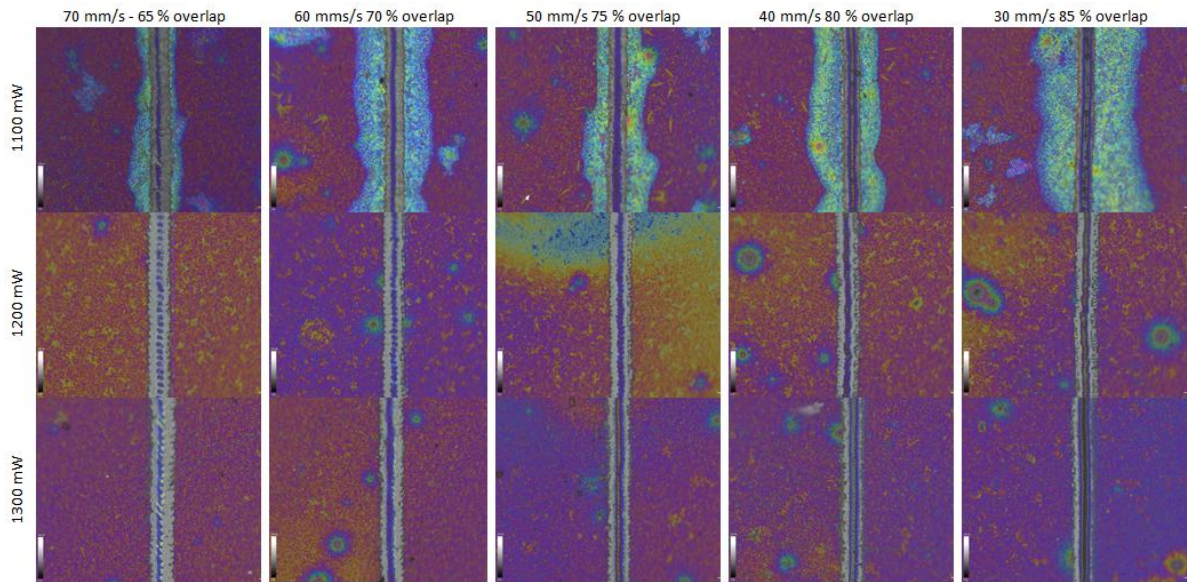


Table C.4: Cross-sectional images with correspondent depth of scribe for the second power scan for the P2 scribed line, with apparent power between 1100 and 1300 mW at scribing speed from 70 to 30 mm/s , cross sectional profile using confocal microscope under topography mode.

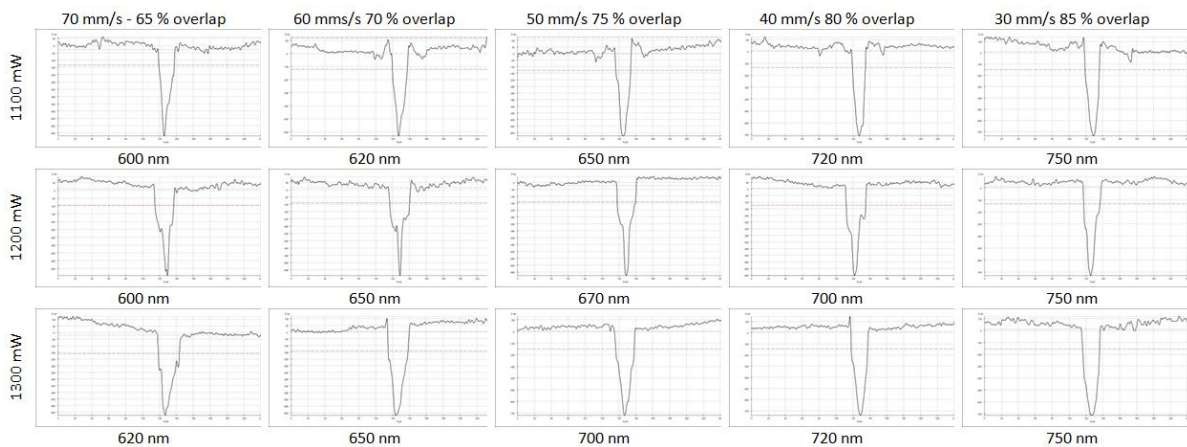
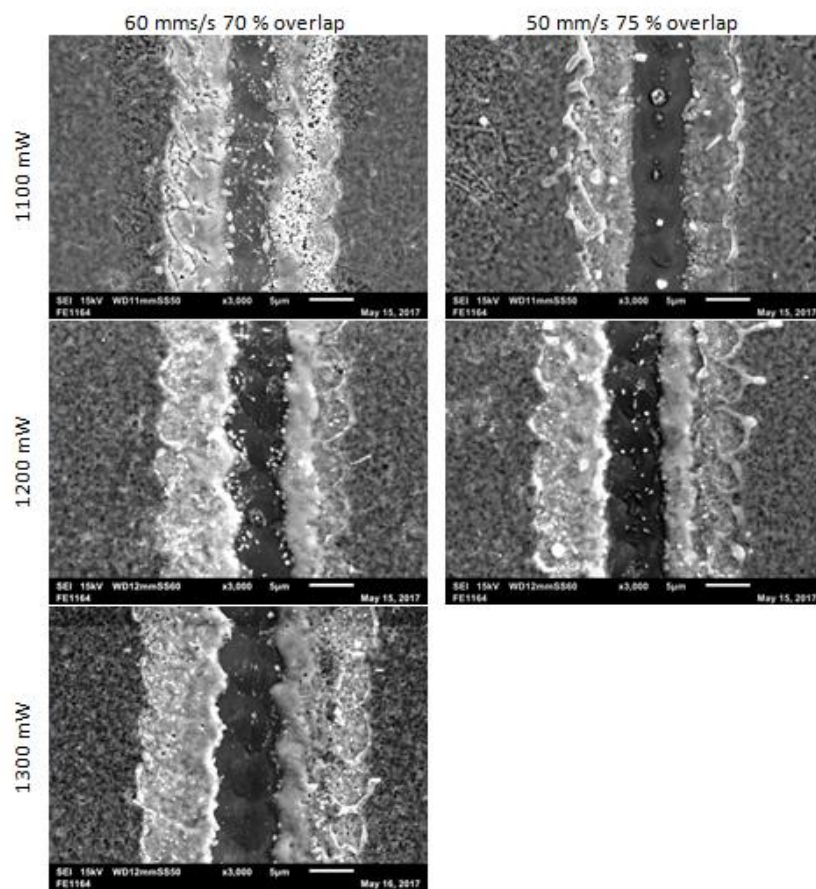


Table C.5: SEM images for selected cases of scribe for the second power scan for the P2 scribed line, 3000x magnification using SEM in scanner mode.



D

TRANSMISSION LINE MEASUREMENT

The Tables [D.1](#) [D.2](#) [D.3](#) show the results of the previous tests (Section [5.2.4](#)). In terms of the contact resistance, the Au-ITO has the half compared to ITO-ITO resistance. Which proves that gold is a better conductive material. The sheet resistance has a value close to 20Ω for all cases, this also shows the good reproducibility of the tests

Table D.1: Resistivity and resistance of Au-ITO and ITO-ITO contacts scribed with 1200 mW

Contact	Au - ITO	Au - ITO	ITO - ITO	ITO - ITO
Power	1200 mW	1200 mW	1200 mW	1200 mW
Scribe speed	50 mm/s	60 mm/s	50 mm/s	60 mm/s
Contact resistance R_C	1.52 Ω	1.43 Ω	3.04 Ω	3.19 Ω
Sheet resistance R_{SH}	21.25 Ω	20.58 Ω	20.85 Ω	20.32 Ω
Contact resistivity ρ_c	4.95 E-4 Ωcm^2	4.64 E-4 Ωcm^2	1.05 E-3 Ωcm^2	1.18 E-3 Ωcm^2

Table D.2: Resistivity and resistance of Au-ITO and ITO-ITO contacts scribed with 1250 mW

Contact	Au - ITO	Au - ITO	ITO - ITO	ITO - ITO
Apparent power	1250 mW	1250 mW	1250 mW	1250 mW
Scribe speed	50 mm/s	60 mm/s	50 mm/s	60 mm/s
Contact resistance R_C	0.75 Ω	0.61 Ω	3.25 Ω	3.42 Ω
Sheet resistance R_{SH}	23.4 Ω	22.80 Ω	24.26 Ω	18.62 Ω
Contact resistivity ρ_c	4.15 E-4 Ωcm^2	4.79 E-4 Ωcm^2	2.58 E-3 Ωcm^2	1.39 E-3 Ωcm^2

Table D.3: Resistivity and resistance of Au-ITO and ITO-ITO contacts scribed with 1300 mW

Contact	Au - ITO	Au - ITO	ITO - ITO	ITO - ITO
Power	1300 mW	1300 mW	1300 mW	1300 mW
Scribe speed	50 mm/s	60 mm/s	50 mm/s	60 mm/s
Contact resistance R_C	1.64 Ω	1.63 Ω	3.76 Ω	3.61 Ω
Sheet resistance R_{SH}	19.1 Ω	20.29 Ω	20.76 Ω	20.11 Ω
Contact resistivity ρ_c	4.65 E-4 Ωcm^2	5.38 E-4 Ωcm^2	1.84 E-3 Ωcm^2	1.76 E-3 Ωcm^2

The Figure [D.1](#) shows an insight of the contact resistivity for all the tests. the clear trend is the less resistivity of the gold-ITO contact with values around the half compared to ITO-ITO contacts. About the power, it has no clear relationship with the resistivity which would infer that it was worked in a good range.

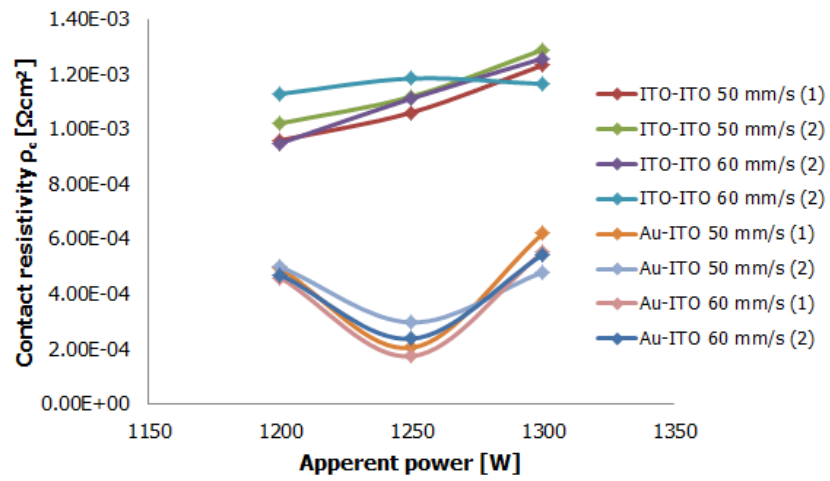
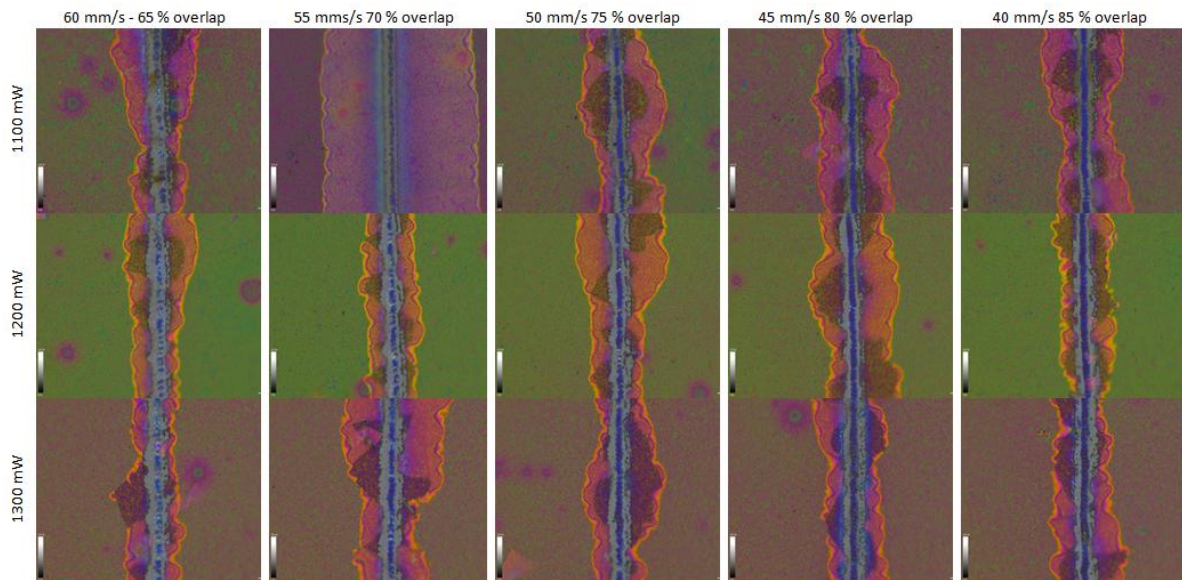


Figure D.1: Contact resistivity ρ_c (in Ωcm^2 vs apperent power (in mW) for selected P2 scribe settings

E

P3 POWER SCAN

Table E.1: Confocal microscope images for the first power scan for the P3 scribed line, with apparent power between 1100 and 1300 mW at scribing speed from 60 to 40 mm/s , 50x magnification with confocal microscopy in white light mode.



F

TRANSMISSION LINE MEASUREMENT FOR THE PROCESSED MODULES

A dispersion of the total resistance R_{TC} and the distance of measurement is made to find the slope and intersection of the curve. As discussed in section 5.2.4. The slope gives the R_{sh}/W , while the intersection is the $2 R_{TC}$. The Figure E1 shows the trend of three tests scribed with the P2 settings.

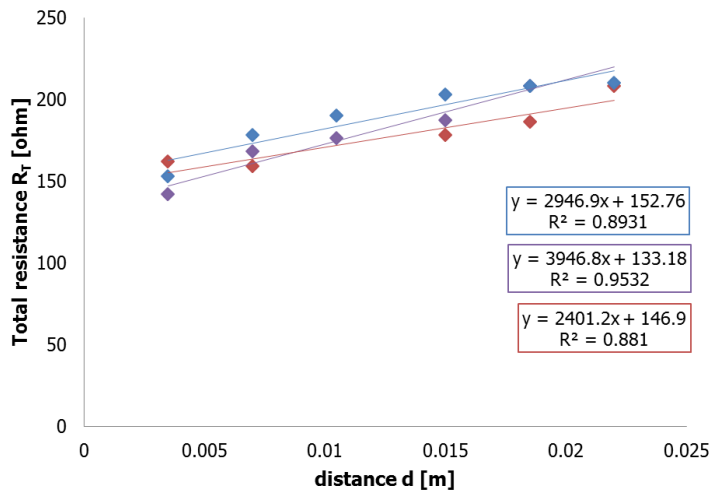


Figure E1: Total resistance R_T (in Ω) versus distance d (in m) for an interconnection scribed with an apparent power of 1300 mW at 60 mm/s scribe speed.

The Table E1 shows the results of the produced minimodules. It can be seen that the resistances are high, the Chapter 6 discusses the origin of this issue.

Table E1: Resistivity and resistance of ITO-ITO contacts scribed with 1300 mW at 60 mm/s

Contact	Test 1	Test 2	Test 3
Power	1300 mW	1300 mW	1300 mW
Scribe speed	60 mm/s	60 mm/s	60 mm/s
Contact resistance R_C	66.59 Ω	68.63 Ω	76.38 Ω
Sheet resistance R_{SH}	19.73 Ω	13.56 Ω	14.73 Ω
Contact resistivity ρ_c	2.16 E-2 Ωcm^2	2.23 E-2 Ωcm^2	2.48 E-2 Ωcm^2